ELECTROPLATING NICKEL ONTO GALLIUM ARSENIDE AND GALLIUM PHOSPHIDE
FOR BETAVOLTAIC APPLICATIONS

ELECTROPLATING NICKEL ONTO GALLIUM ARSENIDE AND GALLIUM PHOSPHIDE NANOWIRES FOR BETAVOLTAIC APPLICATIONS

By LINH LAM, B.A.Sc.

A Thesis Submitted to the School of Graduate Studies in Partial Fulfillment of the Requirements

for the Degree of Master of Applied Science

McMaster University © Copyright by Linh Lam, October 2025

McMaster University

Master of Applied Science (2025)

Hamilton, Ontario (Department of Engineering Physics)

TITLE: Electroplating Nickel onto Gallium Arsenide and Gallium Phosphide Nanowires for

Betavoltaic Applications

AUTHOR: Linh Lam, B.A.Sc. (Carleton University)

SUPERVISOR: Dr. Ray LaPierre

NUMBER OF PAGES: xiii, 87

Lay Abstract

Batteries are everywhere in our daily lives, but most of them need regular charging or replacement. For devices that are very small, placed deep underground, in space, or even inside the human body, replacing or recharging batteries is often impossible. Betavoltaic batteries are a special type of nuclear battery that can solve this problem. Instead of relying on sunlight (like solar cells) or chemical reactions (like normal batteries), they use tiny particles released by radioactive materials to generate electricity. Because certain radioactive materials, like nickel-63, release energy very slowly over many decades, betavoltaic batteries can provide continuous, maintenance-free power for over 100 years.

This thesis focused on improving the design of betavoltaic batteries using nanowires (NWs) - very thin, hair-like structures hundreds of times smaller than a human hair. These NWs capture energy more efficiently than flat surfaces because of their shape and spacing. To make the batteries work, a thin and even layer of nickel needs to be deposited around the NWs. This project developed new methods to "electroplate" nickel onto NWs made from two materials: gallium arsenide and gallium phosphide. Different plating techniques and experimental setups were tested to achieve the most uniform coating.

The research showed that using pulsed electroplating (turning the current on and off in cycles) gave better results than using steady current, because it allowed nickel to spread more evenly along the NWs. These findings provide practical guidelines for how to coat NWs effectively, which is an important step toward making reliable, long-lasting nuclear batteries at the nanoscale.

Abstract

Betavoltaic (BV) devices represent a promising alternative energy technology, offering longlasting, maintenance-free power for applications in remote, harsh, or inaccessible environments. Their performance is often limited by self-absorption of beta particles and inefficient carrier collection in conventional planar geometries. To address these challenges, this work investigates the conformal electroplating of nickel (Ni), and ultimately radioisotope nickel-63 in the future, onto gallium arsenide (GaAs) and gallium phosphide (GaP) NWs for use in BV devices. A systematic evolution of electroplating cell designs - from a simple beaker configuration to a custom Teflon cell - was carried out to optimize uniformity, reproducibility, and current efficiency. Direct current (DC) and pulsed electroplating methods were evaluated across NW arrays of varying pitch (360 nm, 600 nm, and 1000 nm). Results demonstrate that pulsed electroplating significantly mitigates mass diffusion limitations compared to DC plating, improving conformality along NW sidewalls. Optimal plating conditions were found to depend strongly on the interplay between ontime, off-time, and lateral diffusion times within NW arrays. These findings provide a framework for achieving controlled Ni coatings on III–V NWs, representing a key step toward high-efficiency, nanoscale BV devices.

Acknowledgements

I would like to express my deepest gratitude to my supervisor, Ray LaPierre, for his invaluable guidance and support throughout my master's program, ensuring that I remained on track to complete my thesis successfully. I am also grateful to Mohammadreza Shahzadeh and Catherine Luck for providing electronic supplies and assisting me in the construction of my circuit, which was vital for my research. I sincerely thank Jim Cleaver for his assistance in building the customized Teflon cell, which was essential for my experiments, and Jacqueline Huo for her contribution to the COMSOL simulations.

I extend my sincere thanks to Jhoynner S. Martinez and Elisea Vella for teaching me the operation of the Scanning Electron Microscope and the use of Energy Dispersive X-ray analysis, skills that were crucial for my experimental work. I am equally thankful to my fellow graduate students, Amanda Thomas and Ethan Diak, for their generosity in sharing knowledge and guidance in the lab.

I am profoundly appreciative of my parents for their unwavering trust, encouragement, and support throughout my academic journey. Finally, I thank my friends Sophie, Gloria, and Liping for their constant support and companionship during both challenging and rewarding moments.

Table of Contents

LAY ABSTRACT	III
ABSTRACT	IV
ACKNOWLEDGEMENTS	V
LIST OF FIGURES	VII
LISTS OF TABLES	
LISTS OF ABBREVIATIONS	
CHAPTER 1 INTRODUCTION	
1.1 BACKGROUND	
1.2.1 Nanowires (NWs)	
1.2.2 Betavoltaic (BV) Devices	
1.2.3 Nickel Coating on Nanowires	
1.3 OBJECTIVES OF THESIS	
CHAPTER 2 ELECTRODEPOSITION	16
2.1 FUNDAMENTALS OF ELECTROCHEMISTRY	16
2.2 CHEMICAL REACTION IN THE CELL	
2.3 FACTORS IN ELECTRODEPOSITION	20
2.3.1 Bath Composition	
2.3.2 Bath pH	
2.3.3 Temperature	
2.3.4 Current Density	
2.4 ELECTROPLATING ON SI SUBSTRATE AND NWS	
2.4.1 Etching	
2.4.2 Electroplating on Si Substrate and NWs	
CHAPTER 3 DESIGN EVOLUTION	
3.1 ITERATION 1: GLASS BEAKER	32
3.2 ITERATION 2: SEALED ELECTROLYTIC CELL	
3.3 ITERATION 3: CUSTOMIZED TEFLON CELL	37
CHAPTER 4 DC ELECTRODEPOSITION ON SI SUBSTRATES	41
4.1 Iteration 1	41
4.2 ITERATION 2	42
4.3 ITERATION 3	46
CHAPTER 5 DC ELECTRODEPOSITION ON NANOWIRES	51
5.1 GAAs NWs	51
5.2 GAP NWs	
CHAPTER 6 PULSE ELECTRODEPOSITION ON NANOWIRE	S 62
6.1 THE MECHANISM OF PULSE ELECTRODEPOSITION	62
6.2 GAAS NWS	65
6.3 GAP NWs	69
CHAPTER 7 CONCLUSIONS	
DEFEDENCES	94

List of Figures

Figure 1.1. The principle of Si whisker growth via Au-Si catalytic droplets (reproduced from 2)	n Ref.
Figure 1.2. 30° tilted SEM images of Be-doped GaP NWs with 360 nm pitch (a), 600 nm pit	tch
(b), and 1000 nm pitch (c) (reproduced from Ref ³).	
Figure 1.3. The betavoltaic battery design. Obtained from Ref ¹²	
Figure 1.4. A solid betavoltaic p-n junction battery design. Obtained from Ref ¹²	
Figure 1.5. Correlation between conductive channel length and Ni coating (recreated from R	
20)	
Figure 1.6. The illustration of the conformal coating of Ni on GaP NWs	
Figure 2.1. The mechanism of hydrogen passivation 41	
Figure 2.2. The schematic representation of set up for Ni plating using DC source	28
Figure 2.3. The pulse circuit shown in Multisim.	30
Figure 2.4. The experimental setup implementing pulse current signal.	
Figure 3.1. The electrical contact of Si with Cu wire through a thin Cu sheet	
Figure 3.2. The design of wrapping Si substrate with Cu wire in a beaker. Alligator clips we	re
used to provide stability and establish electrical connection with the power supply	34
Figure 3.3. Stony Lab copper sheet electrode holder.	
Figure 3.4. Schematic cross-section of Si attached to Cu sheet electrode holder	35
Figure 3.5. The design of sealed electrolytic cell.	
Figure 3.6. The experimental setup using sealed electrolytic cell as deposition method	
Figure 4.1. Non-uniform Ni deposition on Si in beaker setup, with edge accumulation due to	
poor current distribution with (a) SEM images of Ni coating on n-type Si substrate at 0.43 A	
50 °C for 136 s at different positions at the center, (b) near the center, and (c) at the edge (c)	
Figure 4.2. Cross-sectional view of the n-type Si substrate at 0.43 A, 3V, 50 °C, for 136 s. (a	
SEM image of Ni coating on n-type Si. (b-c) EDX elemental maps showing distributions Ni	
(blue) and Si (green) respectively.	
Figure 4.3. Effect of current on Ni thickness: higher current increases deposition but causes	-
adhesion and flaking at 3V for 144 s at 58 °C. (a-b) SEM images of the coated n-type Si (10	
substrate at 0.025 A and 0.1A respectively. (c-d) EDX elemental maps showing distributions	
Si (teal) and Ni (blue) at current 0.025 A. (e-f) EDX elemental maps showing distributions	
(teal) and Ni (green) at current 0.1 A.	44
Figure 4.4. IPA rinse enhances Ni adhesion and coating uniformity, but excessive deposition	
leads to peeling. Cross-section (tilted 15°) EDX of n-type Si substrate coated with Ni in whi	
(a) and (b) are the results without rinsing with IPA and (c) is the result rinsing with IPA. Bot	
samples were plated at 0.1A and 3V for 144 s at 58 °C.	
Figure 4.5. Image was taken by phone camera, showing peeling of the Ni film observed by a	
eye	
Figure 4.6. Ni growth on Si follows Volmer–Weber mode: particles coalesce into clusters with the coalesce into clusters with t	
higher current. SEM images of n-type Si (100) substrate after rinsing with IPA and coated w	
Ni at (a) 0.005 A, (b) 0.01 A, and (c) photograph of n-type Si sample at 0.05 A.	
Figure 4.7. Ni growth on Si follows Volmer–Weber mode: particles coalesce into clusters will longer deposition times. SEM images of Ni electroplating on n-type Si (100) substrates back	
coated with 400 nm of Al after (a) 60 s, (b) 120 s, and (c) 300 s	
200100 11 11 1 TOV 1111 OL / 11 01 101 (01 OU), (UI 140), (III (UI JUU), (III UI JUU), (III	T /

Figure 4.8. The cross-section SEM images of Ni electroplating on n-type Si (100) substrates
back-coated with 400 nm of Al after (a) 60 s, (b) 120 s, and (c) 300 s
Figure 4.9. The plots of (a) number of Ni particles per unit area in cm ² , (b) percentage of Ni
particle covered the surface of n-type Si substrate (100), and (c) The average size of Ni particles
in μm
Figure 4.10. Faster Ni growth on p-type Si than n-type; at 120 s coatings peel due to excessive
thickness. SEM images of Ni deposition on p-type Si (111) that was back-coated with 400 nm Al then 200 nm of Au at (a) 30 s, (b) 60 s, and (c) 120 s
Figure 4.11. Cross-section SEM images of Ni deposition on p-type Si (111) that was back-coated
with 400 nm Al then 200 nm of Au at (a) 30 s, (b) 60 s, and (c) 120 s
Figure 4.12. The cross-section SEM of sample Ni deposited on p-type Si (111) which was back-
coated with 400 nm Al and 200 nm of Au, which demonstrated Ni peeled off Si's surface 50
Figure 4.13. (a) Number of Ni particles per unit area in cm ² , (b) percentage of Ni particle
covered the surface of p-type Si substrate (111), and (c) average size of Ni particles in µm 50
Figure 5.1. 30° tilted SEM and EDX analysis of Ni-coated GaAs NWs synthesized by DC
electrodeposition. (a) SEM image of GaAs NWs on GaAs substrate before Ni deposition and (b)
after Ni deposition, obtained using DC electrodeposition (0.9 mA, plating time = 1 minute). (c-e)
EDX elemental maps showing distributions of Ga (purple), As (yellow), and Ni (blue),
respectively
Figure 5.2. Plan view SEM and EDX analysis of Ni-coated GaAs NWs synthesized by DC
electrodeposition. (a) SEM image of GaAs NWs on GaAs substrate before Ni deposition and (b)
after Ni deposition, obtained using DC electrodeposition (0.9 mA, plating time = 1 minute). (c-e)
EDX elemental maps showing distributions of Ga (yellow), As (brown), and Ni (purple),
respectively
Figure 5.3. SEM and EDX analysis of Ni-coated GaP NWs (1000 nm pitch) by DC
electrodeposition. (a) SEM image of GaP NWs before Ni deposition. (b) SEM image of GaP
NWs after Ni deposition obtained using DC (0.9 mA, plating time = 45 minutes). (c-f) EDX
elemental maps showing distributions of Si (blue), P (green), Ga (orange), and Ni (purple),
respectively
Figure 5.4. SEM image of GaAs NWs after Ni deposition using DC of 3.6 mA for 15 minutes.
Reproduced from Ref ²⁰
Figure 5.5. (a) SEM image of 360 nm pitch GaP NWs before Ni deposition. (b) SEM image of
GaP NWs after Ni deposition at 3.6 mA for 15 minutes. (c-e) EDX elemental maps showing the
distributions of Si (orange), Ga (jade green), and P (green), respectively. Ni was not detected 56
Figure 5.6. (a) 30° tilted SEM image of 600 nm pitch GaP NWs before Ni deposition. (b) 57°
tilted SEM image of 600 nm pitch GaP NWs after Ni deposition at 3.6 mA for 15 minutes. (c-d)
EDX elemental maps showing distributions of Ni (purple) and Si (blue), respectively
GaP NWs after Ni deposition at 3.6 mA for 15 minutes. (c–d) EDX elemental maps showing
distributions of Ni (green) and Si (red), respectively
Figure 5.8. SEM image of 1000 nm pitch GaP NWs
Figure 6.2. Drift time (t_{drift}) of Ni ²⁺ ions versus applied voltage for GaP NWs
Figure 6.2. Billit time (t_{drift}) of Ni – ions versus applied voltage for Gai N ws
= 10 ms, t_{off} = 1 s, plating time = 15 min) with the arrows indicating the location of Ni
deposition. (b-d) EDX elemental maps showing distributions of Ga (blue), As (purple), and Ni
(green), respectively

Figure 6.4. (a) SEM image of Ni-coated GaAs NWs obtained using pulse signal parameters (t_{on}
= 10 ms, t_{off} = 1 s, plating time = 30 min). (b–d) EDX elemental maps showing distributions of
Ga (yellow), As (brown), and Ni (purple), respectively
Figure 6.5. GaAs NWs from Figure 6.4. (a) SEM image of GaAs NWs with a height marker of
2 μm. (b) SEM image of a single NW, with a yellow line indicating the region analyzed by EDX.
(c) Elemental intensity profiles along the line in (b), showing the distributions of Ni (red), Ga
(green), and As (blue)
Figure 6.6. (a) SEM image of Ni-coated GaAs NWs obtained using pulse signal parameters (t_{on}
= 10 ms, t_{off} = 1 s, plating time = 90 min). (b–d) EDX elemental maps showing distributions of
Ga (orange), As (green), and Ni (yellow), respectively.
Figure 6.7. Correlative structural and elemental analysis of the surface structure of GaAs NWs
from Figure 6.6. (a) SEM image of GaAs NWs with a height marker of 2 µm. (b) SEM image of
a single NW, with a yellow line indicating the region analyzed by EDX. (c) Elemental intensity
profiles along the line in (b), showing the distributions of Ni (purple), Ga (yellow), and As
(orange)
Figure 6.8. (a) SEM image of 360 nm pitch GaP NWs after Ni deposition using $t_{on} = 10$ ms, t_{off}
= 1s, V = 3 V, and plating for 15 min. (b-d) EDX elemental maps showing distributions of Si
(blue), Ga (yellow), and P (purple), respectively. Ni was not detected
Figure 6.9. (a) SEM image of GaP NWs with a 360 nm pitch after Ni deposition. (b–c) EDX
spectra obtained from the selected regions in (a). The orange rectangle and the green star indicate
the specific areas analyzed by EDX71
Figure 6.10. (a) SEM image of 600 nm pitch GaP NWs after Ni deposition using $t_{on} = 10$ ms,
$t_{off} = 1 \text{ s}, V = 3 \text{ V}, \text{ and plating for 15 min. (b-d) EDX elemental maps showing distributions of }$
Si (blue), Ga (yellow), and P (purple), respectively
Figure 6.11. (a) SEM image of GaP NWs with a 600 nm pitch after Ni deposition. (b-c) EDX
spectra obtained from the selected regions in (a). The orange rectangle and the green star indicate
the specific areas analyzed by EDX
Figure 6.12. The electric field components along the y- and z-axes (E _y and E _z) around NW
structure. The legend is presented on a logarithmic scale by a factor of 10^{-12} to set the base
reference level for the smallest arrow lengths. A range quotient of 10 ³ indicates that the longest
arrows are about 1000 times longer than the shortest one. The greyscale represents the norm of
the Y- and Z- components
Figure 6.13. Conformal Ni coating achieved on GaP NWs at 1000 nm pitch. (a) SEM image of
1000 nm pitch GaP NWs after Ni deposition using $t_{on} = 10$ ms, $t_{off} = 1$ s, $V = 3$ V, and plating
for 15 min. (b-e) EDX elemental maps showing distributions of Si (green), Ga (orange), P
(blue), and Ni (red), respectively
Figure 6.14. EDX map spectrum of 1000 nm pitch GaP NWs on p-type Si substrate74
Figure 6.15. The morphological difference of GaP before and after deposition. (a) SEM of GaP
NW array before deposition. (b-d) SEM images of GaP NWs (1000 nm pitch), showing
conformal coating along sidewalls for 15 min, 30 min, and 45 min of Ni deposition, respectively.
Figure 6.16. (a-c) TEM images of a Ni-coated GaP NW at increasing magnifications, from low
(a) to high (c)
Figure 6.17. (a) TEM image of a Ni-coated GaP NW, showing the polycrystalline nature of the
Ni layer. (b) Selected area electron diffraction (SAED) pattern obtained from region Diff 05 77

Figure 6.18. (a–b) TEM images of the top region of a GaP NW. (c) EDX elemental map of the	
same region, where red corresponds to Ni, blue to P, and green to Ga. (d) EDX line-scan	
thickness analysis, showing Ni (orange), Ga (green), and P (blue), with the Ni layer thickness	
measured to be approximately 150 nm.	78
Figure 6.19. (a–b) TEM images of the middle region of a GaP NW. (c) EDX elemental map of	
the same region, where red corresponds to Ni, blue to P, and green to Ga. (d) EDX line-scan	
thickness analysis, showing Ni (orange), Ga (green), and P (blue), with the Ni layer thickness	
measured to be approximately 166 nm.	78
Figure 6.20. (a–b) TEM images of the bottom region of a GaP NW. (c) EDX elemental map of	
the same region, where red corresponds to Ni, blue to P, and green to Ga. (d) EDX line-scan	
thickness analysis, showing Ni (orange), Ga (green), and P (blue), with the Ni layer thickness	
measured to be approximately 179 nm.	79
Figure 6.21. SEM measurements showing the increase in a GaP NW diameter with Ni coating a	ιS
a function of time	80
Figure 6.22. Evolution of the Ni coating thickness on GaP NWs with a 1000 nm pitch over time) .
	81

Lists of Tables

Table 4.1. The experimental conditions for n-type Si (100) samples as deposition time incre	
Table 4.2. The experimental conditions for p-type Si (111) samples as deposition time increase.	
	48

Lists of Abbreviations

SEM Scanning Electron Microscope

TEM Transmission Electron Microscope

EDX Energy-Dispersive X-ray Spectroscopy

SAED Selected Area Electron Diffraction

CCEM Canadian Centre for Electron Microscopy

DC Direct Current

PED Pulse Electrodeposition

MBE Molecular Beam Epitaxy

GS-MBE Gas Source Molecular Beam Epitaxy

NW Nanowire

BV Betavoltaic

FIB Focused ion beam

BOE Buffered oxide etch

CVD Chemical Vapor Deposition

UHV Ultra-High Vacuum

SAE Selective-Area Epitaxy

EBL Electron Beam Lithography

RIE Reactive-Ion Etching

GHG Greenhouse Gas

RCA Radio Corporation of America

EHPs Electron-Hole Pairs

MEMS Microelectromechanical Systems

BOE Buffered Oxide Etch

IPCC Intergovernmental Panel on Climate Change

Chapter 1 Introduction

1.1 Background

As society advances, the demand for green energy and the miniaturization of devices to the micro- and nanoscale have risen significantly. NWs are promising and attractive candidates for reducing device sizes and harvesting energy. Like photovoltaic devices, betavoltaic (BV) cells utilize the high aspect ratio and charge carrier dynamics of NWs to generate electrical energy from a radioactive beta source ¹. Semiconductor NWs can absorb beta particles (high energy electrons) produced by a beta emitter deposited between the NWs. Electron-hole pairs are produced in the semiconductor NWs upon beta absorption. These electron-hole pairs are separated and collected at electrical contacts on either end of NWs, resulting in electrical output power.

One of the most common beta sources for BV devices is nickel-63 (63Ni), which has a half-life of 100.2 years. ² This long half-life makes it suitable for special applications that require a long-lasting power source, minimal maintenance, and resilience in harsh environments such as space, underground, or within the human body. ⁶³Ni is commonly used for BV devices because its radiation spectrum is below the lattice damage threshold for Si, SiC, and other semiconductors ². ⁶³Ni has an energy range that neither damages the lattice structure nor shortens device lifetimes ³. Moreover, ⁶³Ni exists in metallic form, making it easier to handle and deposit compared to some other beta sources (such as ³H) ².

Commercial BV devices use a planar semiconductor substrate with a thin layer of radioisotope deposited on top. However, the power output is relatively low due to the

isotropic nature of radioactive emission, shielding by device contacts, and self-shielding by the radioisotope itself³.

Various methods exist for depositing nickel (Ni) onto semiconductor substrates, including electroplating, spin coating, electroless plating, and chemical vapor deposition. Electroplating, especially with ⁶³Ni, has become the most widely used technique ². This project aims to deposit Ni (and eventually ⁶³Ni) conformally onto NWs using electroplating to maximize energy capture and improve overall energy output.

1.2 Literature Review

1.2.1 Nanowires (NWs)

NWs are classified as one-dimensional (1D) nanomaterials, meaning they have cylindrical nanostructures with diameters in the nanometer range and lengths that can extend to micrometers. Recently, NWs have been the focus of intensive research due to their unique applications in mesoscopic physics and devices ⁴. NWs exhibit a wide range of properties - electrical, optical, biological, magnetic, and sensory.

Metallic NWs offer excellent electrical conductivity, advancing electronics by enabling smaller transistors, faster computers, and reduced CPU heat ⁴. Magnetic NWs such as Fe, Ni, Co-Cu, and Co can store large amounts of data in compact formats. Due to their small size and light weight, NWs are highly sensitive and are used in sensors such as gas detectors ⁴. Their high aspect ratio and geometry enhance the physical properties of semiconductors via quantum confinement. Moreover, their high surface-area-to-volume ratio improves performance and increases chemical reactivity ⁵.

NWs can be synthesized using various methods, including chemical vapor deposition (CVD), molecular beam epitaxy (MBE), laser ablation, and microwave-assisted physical vapor deposition. MBE was originally developed in 1968 by J.R. Arthur and A.Y. Cho for GaAs/Al_xGa_{1-x}As growth, ⁶ enabling precise control of composition, thickness, and doping for high-quality single-crystal thin films ⁷⁻⁸. MBE is the growth process based on the adsorption of atomic or molecular beams with a heated crystalline substrate in ultrahigh vacuum (UHV)¹. MBE processes rely on thermal and kinetic factors like evaporation, adsorption, surface diffusion, and incorporation ⁶⁻⁸. The term "epitaxy" means that the deposited layers have either identical or similar crystal structure as the substrate (less than 10% difference in lattice constant) ¹.

The vapor-liquid-solid (VLS) mechanism introduced by Wagner and Ellis in 1964 is commonly used in MBE for growing NWs ⁹. Initially developed for growing crystalline silicon (Si) whiskers using gold as a catalyst (Figure 1.1), the method was later advanced by Lieber, Yang, and Samuelson to produce high-quality NWs ¹⁰. The process involves forming an Au-Si alloy above the eutectic point (363 °C), then precipitating Si from the supersaturated droplet to form a liquid-solid interface. Continuous growth occurs through nucleation and diffusion at this interface ^{9–10}.

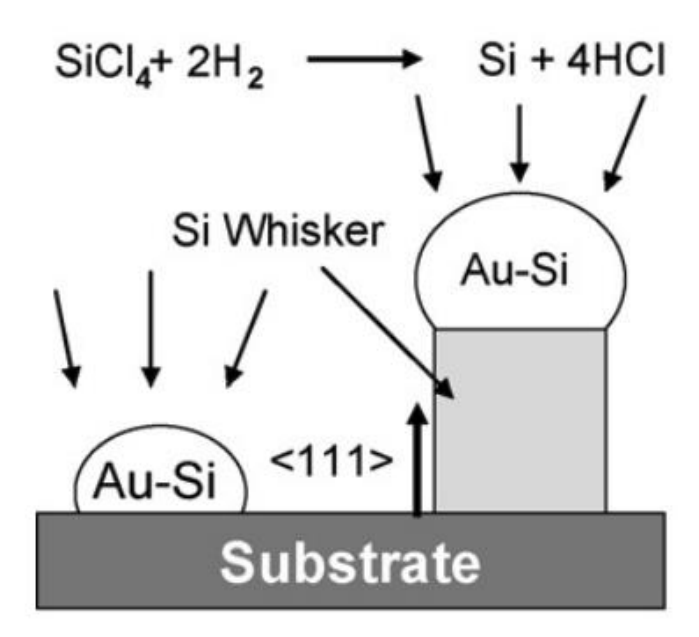


Figure 1.1. The principle of Si whisker growth via Au-Si catalytic droplets (reproduced from Ref. ²).

The VLS mechanism is also used for III-V materials via selective-area epitaxy (SAE), where electron beam lithography (EBL) creates patterned holes in an oxide mask on the substrate to control NW size and location. The oxide layer encourages selective nucleation of NWs within the mask openings on the exposed substrate, while simultaneously preventing nucleation on the oxide itself. Additionally, the oxide layer helps suppress unwanted thin film or crystallite formation between the NWs ¹¹.

In previous work, GaP NWs were grown by Thomas using gas source MBE (GS-MBE), as shown by scanning electron microscopy (SEM) images in Figure 1.2 ³. These NWs were grown by MBE using the self-assisted growth process where Ga droplets were used to nucleate the NWs instead of Au. The NW growth process was conducted in two distinct stages: (i) pre-deposition of Ga droplets and (ii) growth of Be-doped GaP NWs. In the first stage, a solid gallium (Ga) source (group III) was thermally evaporated and directed

toward the oxide mask openings at a deposition rate of $0.125 \,\mu\text{m/h}$ for $250 \,\text{s}$ at a substrate temperature of $650 \,^{\circ}\text{C}$, resulting in the formation of Ga catalyst droplets 3 . In the subsequent growth stage, phosphorus (P₂) vapor, generated by thermal cracking of phosphine (PH₃), was introduced at a flux three times greater than that of Ga (V/III flux ratio = 3). The growth proceeded for 90 min, yielding 100% NWs with a beryllium (Be) doping concentration of approximately $1 \times 10^{19} \,\text{cm}^{-3}$ 3. Throughout both stages, the Ga impingement rate and substrate temperature were held constant. Growth was terminated by simultaneously closing the Ga, PH₃, and Be shutters 3 . The resulting p-type GaP NWs exhibited pitches (separation between NWs) of 360 nm, 600 nm, and 1000 nm; lengths ranging from 3.6 to 3.8 μ m; and diameters between 101 and 135 nm 3 .

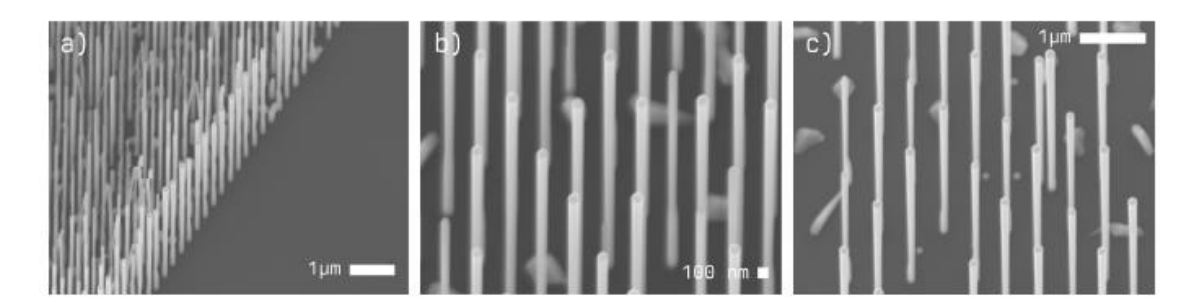


Figure 1.2. 30° tilted SEM images of Be-doped GaP NWs with 360 nm pitch (a), 600 nm pitch (b), and 1000 nm pitch (c) (reproduced from Ref ³).

1.2.2 Betavoltaic (BV) Devices

According to the Intergovernmental Panel on Climate Change (IPCC) (2022), global total greenhouse gas (GHG) emission has significantly increased since 1850 ⁴. Fossil fuels such as coal, oil, and gas are the largest factor contributing to GHG emission ⁴. Burning fossil fuels leads to carbon dioxide emission which is considered the main cause of global warming and climate change, known as the greenhouse effect ⁵. Moreover, fossil fuels are scarce, yet they provide most energy all over the world. Energy usage continues

increasing while fossil fuels are not sustainable economically and environmentally. Researchers are developing alternative energy sources that are clean and sustainable. Betavoltaic batteries are one of the alternative energy sources that generate electrical energy from the decay of radioactive sources. Betavoltaics utilize a beta-emitting radioisotope, making it a suitable source in dark environments unlike solar energy. Compared to other clean sustainable energy sources such as wind and solar energy, betavoltaic energy is not influenced by the environment and able to operate longer due to the long half-life of radioisotopes ⁶. Therefore, betavoltaic batteries can operate under harsh conditions, provide long-lasting power, and operate with little maintenance suitable for space, the human body, ocean, and polar regions ⁶.

In 1953, a betavoltaic device was first reported by Paul Rappaport at Radio Corporation of America (RCA) ⁷. Rappaport and his coworkers investigated a Si semiconductor with 50 mCi of ⁹⁰Sr-⁹⁰Y radioactive source ⁷. The radiation damage ⁸ and electron voltaic effect ⁹ reduced the efficiency to 0.4%. Electronic voltaic effect is similar to the photovoltaic effect in the p-n junction of a semiconductor ¹⁰. In a p-n junction, electrons from the high concentration (n-type) region diffuse to the lower concentration (p-type) region, while holes from the high concentration (p-type) region diffuse to the lower concentration (n-type) region. As a result, a region called the depletion region or depletion zone is created. The p-region now becomes negatively charged while the n-region becomes positively charged. This charge difference creates an electric field from the n to p region. When the p-n junction is illuminated with photon energy that is higher than the bandgap energy of the semiconductor, electron-hole pairs (EHPs) are generated. Due to the built-in electric field of the depletion region, photo-generated electrons and holes are driven across the p-

n junction. Hence, a voltage appears, and power can be delivered if the p-n junction is connected to an external circuit. This phenomenon is called the photovoltaic effect ¹¹. The electronic voltaic effect is similar to the photovoltaic effect but using electrons for excitation instead of light ¹⁰.

During 1968-1974, the licensed Betacel pacemakers were implemented on over 100 patients as cardiac pacemakers from Larry Olsen's group at Donald W. Douglas Laboratories. The Betacel was made of p-n junctions of Si cells paired with ¹⁴⁷Pm in the form of Pm₂O₃ ¹². The Betacel battery achieved 4% efficiency with over 10 years lifetime. ⁹ However, lithium batteries replaced betavoltaic batteries in the pacemaker market as lithium is cheaper and safer than ¹⁴⁷Pm ⁹. Subsequently, the research on betavoltaic batteries slowed down until 2006. After 2006, many manufacturers including BetaBatt ¹², Ovnergy, City Labs, and Widetronix developed several novel betavoltaic batteries 9. In 2008, Oynergy's Ouvncell KRT-2000 betavoltaic power cell was awarded a specific license by the US Nuclear Regulatory Commission ¹². This specific license marked a remarkable milestone in the betavoltaic industry - the device could now be sold to properly trained workers. Nevertheless, it still limited the device to only users who were trained to work with radionuclides. Two years later, City Lab's Nano-Tritium battery passed all nuclear regulatory requirements and was awarded as the first betavoltaic device providing a general license to any user ^{9,12}.

Along with the advancements of nanotechnology, betavoltaic batteries have renewed interest among many researchers nowadays. With their compact size, reliability, and long-lasting energy capabilities, betavoltaic batteries represent highly attractive power sources

for future electronic applications. Betavoltaic batteries are categorized under nuclear batteries, which converts electrical energy from radioisotope energy ¹³ by employing semiconductor p-n junctions to collect charge (Figure 1.3) ¹³. Beta particles emitted from an isotope decay strike the semiconductor junction, ionizing atoms and creating thousands of EHPs. These pairs are then separated by the semiconductor p-n junction and collected to generate electrical power. While one beta particle can create many EHPs, much of its energy is lost due to isotropic radiation emission with half of all betas emitted away from the semiconductor ¹³.

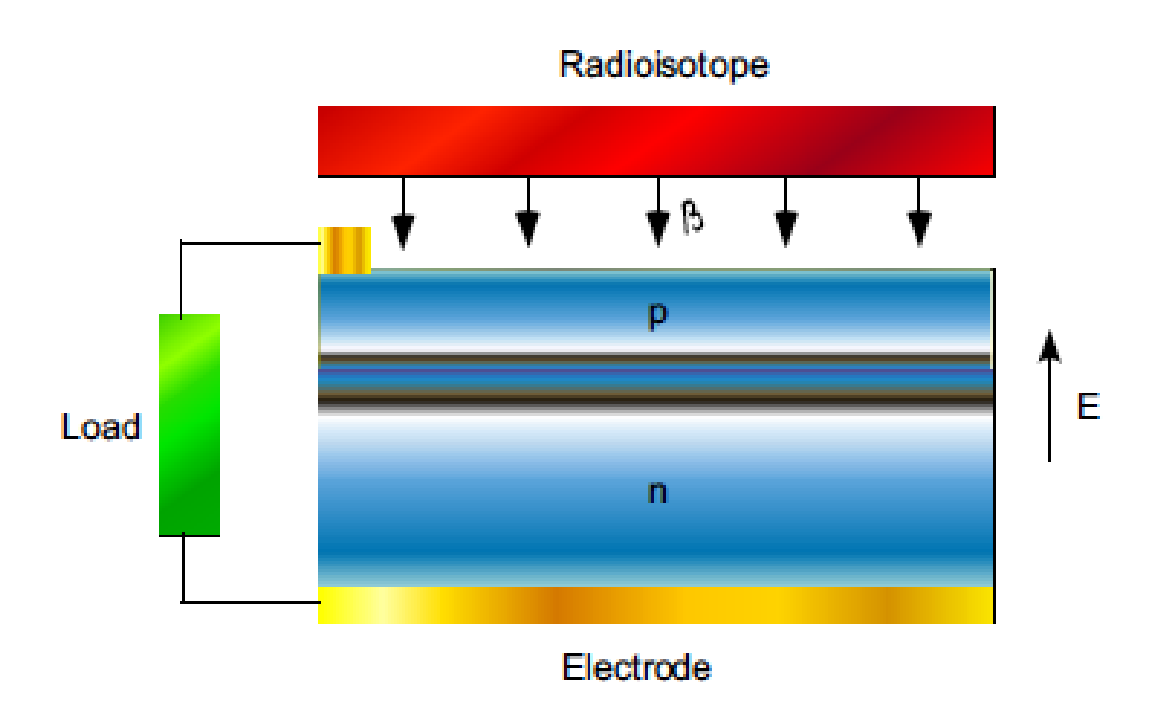


Figure 1.3. The betavoltaic battery design. Obtained from Ref¹³.

Typically, a betavoltaic battery's design includes an upper electrode, a p-type region (doped surface region), a depletion region, an n-type region (doped substrate), and a bottom electrode as shown in Figure 1.4 ¹³. Energetic beta particles emitted from the radioisotope enter and create EHPs in the semiconductor through collision, excitations,

and ionization. Each beta particle can generate several thousand EHPs, although the EHPs can recombine and cause energy loss in betavoltaic batteries. Lattice vibrations also contribute to the reduction in efficiency ¹³. EHPs created in the depletion region can be separated by the built-in electric field. Beta-generated electrons and holes are separated towards the n- and p-type region, respectively, and subsequently collected by the contacts. A thin p-type layer is usually used in the design to minimize the recombination events and maximize EHPs collected from the depletion region ¹³.

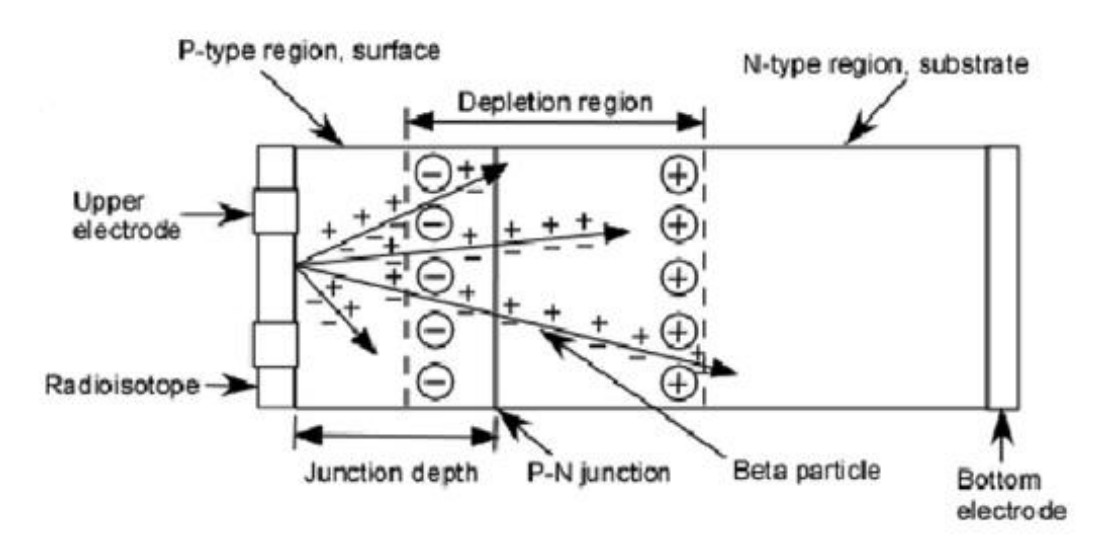


Figure 1.4. A solid betavoltaic p-n junction battery design. Obtained from Ref ¹³.

Zhang et al. introduced the idea of modulating the doping density to increase the EHPs in 4H-SiC ⁹. The resulting energy conversion efficiency of the betavoltaic device was 1.99% with a 0.16 mCi ⁶³Ni source. Half of emitted beta particles are lost due to isotropic emission and do not generate any EHPs in the planar geometry design ¹⁴. Another loss is the self-absorption effect of beta particles in the radioisotope source. The source layer needs to be thick enough to achieve high activity, while the thickness can cause beta particles to be absorbed before reaching the p-type region ¹⁴. This shielding effect can be

minimized if the radioisotope has sufficiently high beta-decay energies ¹⁵. However, energy above 100 keV will likely cause damage to the lattice structure inside the semiconductor and eventually result in the reduction of device lifetime. ¹⁵ Therefore, Ni-63 and tritium are two main radioisotopes because their maximum beta energies are 65.9 keV and 18.6 keV, respectively ¹⁵. At these energy levels, the shielding of the contact and source are considerable. Establishing a micro- and nanoscale structure to BVs is intended to reduce self-shielding and improve energy capture, as explained below ¹⁵.

In 2019, Wagner et al. developed a new design of a NW-based betavoltaic device through simulation and optimization that can overcome the self-shielding effect occurring in planar BVs. ¹⁵ This design consists of a hexagonal array of axial NW p-i-n junction diodes grown on a Si substrate and radioisotope source filling the space between NWs. This new design utilizes the isotropic emission of beta particles by surrounding the beta source with NW arrays. Additionally, the small space between NWs shortens the travel path length of beta particles that reduces significantly the self-shielding effect. Previous work has shown that porous Si with a tritium source significantly improved the device performance up to ten fold compared to a planar design. 15 Nevertheless, further improvement can be accomplished by employing higher band gap material such as gallium phosphide (GaP) that improves the open-circuit voltage ¹⁵. Additionally, it was demonstrated that growing III-V material on Si does not generate misfit dislocations as NWs accommodate greater elastic strain than a planar geometry ¹⁶. The indirect bandgap of GaP offers the advantage of achieving adequate minority carrier lifetimes for efficient charge carrier collection. ⁶³Ni was chosen as the beta emitter source as it meets certain criteria. ⁶³Ni has a long halflife (approximately 100 years) with the average and maximum energy lower than the

damage energy threshold of GaP ¹⁷. Moreover, ⁶³Ni is considered relatively safe due to its low chemical toxicity and the fact that it can be effectively shielded with a thin layer of plastic ¹⁷.

Inserting ⁶³Ni in the space between NWs is another consideration, but the process can be accomplished through electroplating or spin-coating. McNamee et al. demonstrated the spin-coating method on a GaP NW betavoltaic device and reported the overall device efficiency of 0.45% ⁸. There are some possible improvements to the beta capture efficiency, namely reducing NWs pitch, increasing the volume of ⁶³Ni between NWs, and increasing NWs length. The low fill factor (25%) observed in the electrical characteristics of the NW diodes may result from low beta particle capture ⁸. Hence, Ni electrodeposition is proposed to replace the sol-gel method with the possibility of reducing the consequence of self-absorption and enhance beta interaction in NWs ⁸.

Betavoltaic battery size can be reduced to human hair scale while chemical batteries cannot be due to the restriction of low energy density. Miniaturization of fossil fuels and fuel cells has also been attempted, yet there are many challenges during the scaling down process. At small scale, it is difficult to replenish and package the liquid fuel supply while removing by-products ¹³. This process also reduces energy density in fossil fuels and fuel cells ¹³. Meanwhile, betavoltaic batteries do not require refueling as it lasts from several years up to several hundreds of years because of the long half-life of the radioactive source. Its energy density is 10² to 10⁴ times higher than chemical and fossil fuels ¹³. Betavoltaics have many applications in microelectromechanical systems (MEMS), remote sensors, and implantable medical devices. With high energy, prolonged lifetime,

and anti-jamming property, they are suitable to explore harsh environments like space, undersea, underground, polar and torrid regions. Betavoltaic batteries can also be used in military and sensor applications ¹³. Although the conversion of a nuclear source to electrical energy is low, betavoltaic batteries are still a very promising energy source in the future of the nuclear battery industry.

1.2.3 Nickel Coating on Nanowires

The conformal coating of Ni on NWs depends on various factors: the length of the NWs, the aspect ratio, deposition current, bath concentration, and plating duration. NWs require axial or core-shell (coaxial) heterostructures or p-n junctions to separate electron-hole pairs ¹⁸. There are three classifications in coaxial NWs, namely active core/conductive shell coaxial NWs, conductive core/active shell coaxial NWs, and other coaxial NWs ¹⁹. A conducting core refers to a material that is electrically conductive, allowing electrons to move easily through it. In 2025, Kuzmin et al. demonstrated that Ni particle formation varies with GaAs NW geometry ²⁰.GaAs NWs were grown on n-type (111) Si substrate with a height of 5 µm and diameter of approximately 60 nm using MBE and Au nanoparticles as a catalyst ²⁰. The study concluded that doping GaAs NWs with Si due to unintentional absorption of Si atoms by the Au NPs can result in core-shell structures. Referring to Figure 1.5, the orange region represents the GaAs:Si n-type channel (core) within the GaAs NWs (blue). When the core length (L_c) matches the NW length (L_w), rounded Ni clusters form at the NW tips. If the core is shorter, Ni forms as isolated islands

or nanoparticles on the NW sidewalls. With sufficient current and time, clusters may coalesce into a continuous coating (Figure 1.6) ²⁰.

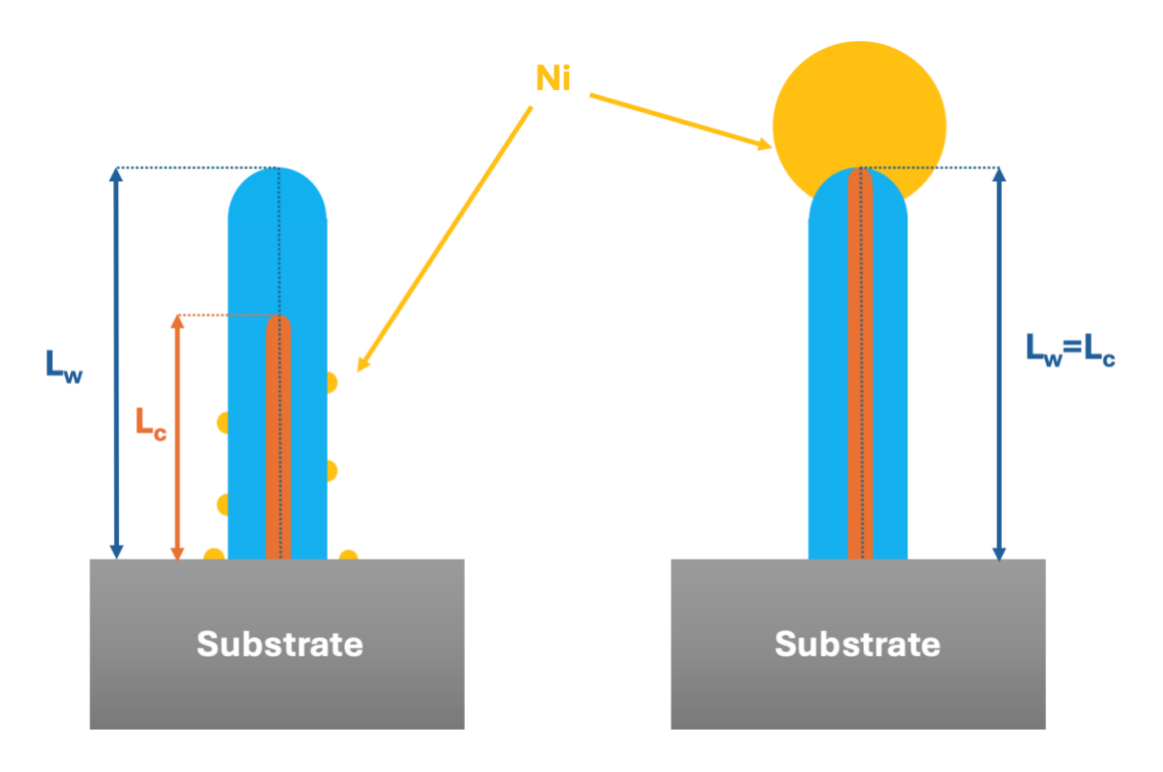


Figure 1.5. Correlation between conductive channel length and Ni coating (recreated from Ref ²⁰).

Ni particles form via the Volmer-Weber growth mode, which favors deposition at the lower portions of NWs, where conductivity was reportedly higher ¹³. As previously noted, doping levels declined as NW growth progressed ²⁰. Volmer-Weber is one of three epitaxial growth modes (along with Frank–van der Merwe and Stranski–Krastanow) ²¹. The Frank–van der Merwe mode occurs with minimal lattice mismatch and yields layer-by-layer growth. Stranski–Krastanow begins with two-dimensional growth, transitioning to three-dimensional island formation. Volmer-Weber occurs in systems with high lattice mismatch, where materials form 3D islands directly on the substrate without forming a wetting layer ²¹.

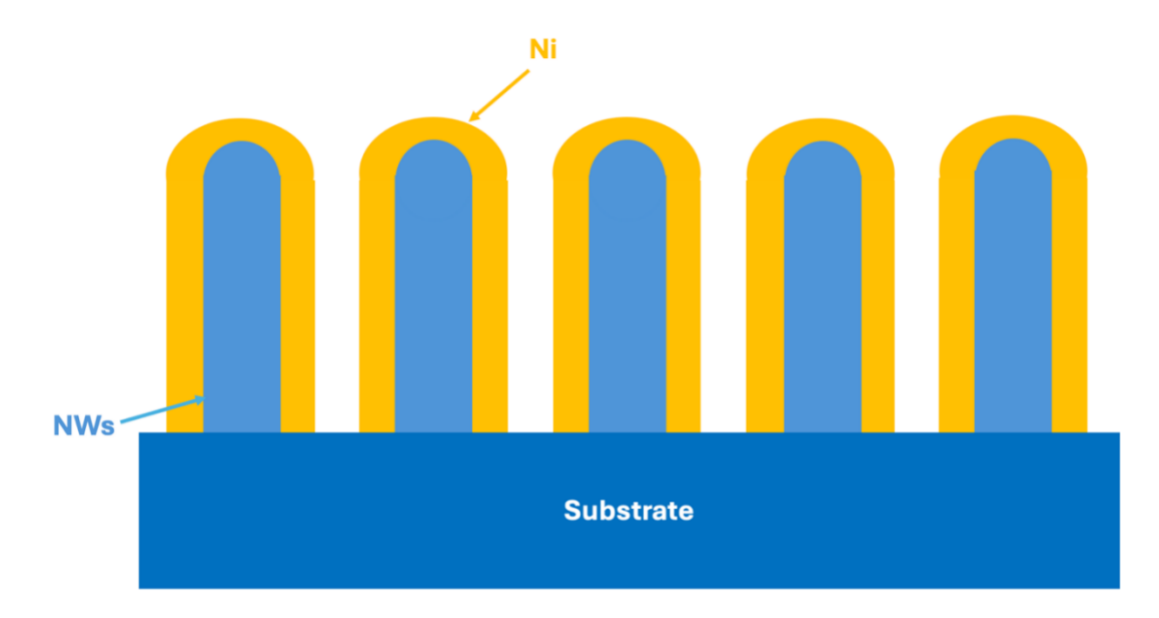


Figure 1.6. The illustration of the conformal coating of Ni on GaP NWs.

1.3 Objectives of Thesis

Previous research using the sol-gel method for radioisotope deposition showed limitations, such as carrier depletion in NWs, self-absorption, and low electrical output.

16 Therefore, this project aims to use electroplating to deposit a uniform Ni layer between NWs, such as Figure 1.6, improving betavoltaic device efficiency by reducing beta self-absorption.

This project focuses on depositing a thin (~100 nm) layer of Ni on pre-synthesized GaAs NWs using Au catalyst with arbitrary pitch²², and GaP NWs with pitches of 360 nm, 600 nm, and 1000 nm¹¹ using both DC and pulsed electroplating. The goal is to compare results and determine the most effective method for fabricating high-performance BV devices.

Chapter 2 Electrodeposition

2.1 Fundamentals of Electrochemistry

The fundamental concept of electrochemistry is to study electron transport within a chemical reaction ²³. Most reactions occur at an electrode surface and include processes such as adsorption, desorption, and crystallization ²⁴. These processes significantly impact the electrochemical behavior of the electrode through the electrolyte-electrode interface. Electrochemistry was first developed by Alessandro Volta in 1800 with the invention of the first battery, also known as the voltaic pile ²⁵. Volta's experiment consisted of stacks of copper (Cu) and zinc (Zn) and separated by paper or cloth soaked in brine ^{24,25}. Following Volta's invention, scientific development in this field became intensive and grew rapidly. Numerous experiments were conducted after the voltaic pile, but it wasn't until 1835 that Michael Faraday established a foundation for electrochemical concepts, introducing key terms such as anode, cathode, electrode, electrolyte, and ion ^{24,25}. Among these terms, "cell" is commonly used due to the wide variety of functions, shapes, and sizes. There are two primary types of electrochemical cells: galvanic (voltaic) cells and electrolytic cells. In galvanic cells, electrochemical reactions occur spontaneously through redox reactions, while electrolytic cells require an external energy source (such as DC or AC power) to initiate reactions. In both cells, oxidation occurs at the anode and reduction occurs at the cathode ²³. However, the polarity of the electrode differs: in galvanic cells, the anode is negative, and cathode is positive, while in electrolytic cell, the anode is positive and cathode is negative.

In the experiments of this thesis, an external source of energy is being utilized, so the electrolytic cells are relevant. The anode is Platinum (Pt) mesh, and the cathode is Si/NWs

substrate. Pt mesh is advantageous for precisely controlling the electroplating process because Pt is inert and exhibits a high exchange current density, without participating in the redox reactions occurring in the electrochemical cell, making it an ideal choice for the anode ²⁶. Additionally, the mesh structure yields a greater uniformity in metal deposition compared to other shapes due to its higher surface area. The large surface area of Pt mesh facilitates a higher rate of fuel conversion with minimal electrode polarization, resulting in greater power output for fuel cells ²⁷.

2.2 Chemical Reaction in the Cell

As mentioned before, Pt mesh is the anode, and the NWs are the cathode. The bath solution in this experiment consisted of nickel chloride (NiCl₂.6H₂O) and boric acid (H₃BO₃). NiCl₂.6H₂O increases the conductivity of solution, and so reduces the voltage requirement ²⁸. H₃BO₃ is a buffer solution to control the solution pH. The chemical reactions of each half-cell are:

Cathode (-):
$$Ni_{(ag)}^{2+} + 2e^- \rightarrow Ni_{(s)}$$
 $E_{cathode}^0 = -0.26$ (2.1)

$$2H_{(aq)}^{+} + 2e^{-} \rightarrow H_{2(g)}$$
 $E_{cathode}^{0} = 0 \text{ V}$ (2.2)

Anode (+):
$$2Cl_{(ag)}^- \to Cl_{2(g)} + 2e^- \qquad E_{anode}^0 = 1.36 \text{ V}$$
 (2.3)

$$2H_2O_{(l)} \rightarrow O_{2(g)}^{\uparrow} + 4H_{(aq)}^{+} + 4e^{-} \qquad E_{anode}^{0} = 1.23 \text{ V}$$
 (2.4)

Buffer reaction:
$$H_3BO_3 + H_2O \rightleftharpoons [B(OH)_4]^- + H^+$$
 (2.5)

Although Cl- oxidation has lower standard potential than water oxidation, Pt anode does not catalyze the reaction (2.3) efficiently. Oxygen evolution on Pt is kinetically favourable despite of its slightly greater thermodynamic potential. Thus, the overall reaction is:

$$Ni_{(aq)}^{2+} + 2H_2O_{(l)} \rightarrow Ni_{(s)} + O_{2(g)}^{\uparrow} + 4H_{(aq)}^{+}$$
 (2.6)

Reaction (2.4) produce H⁺ which reduces the pH of the solution, so H₃BO₃ acts like a buffer and maintains a stable pH, as discussed below. Moreover, the protons provided by H₃BO₃ prevent excessive hydrogen evolution at the cathode which improves the quality of Ni plating. The reaction (2.2) is an undesired side reaction because it creates hydrogen bubbles and defects in the uniformity of the plated surface.

The standard cell potential of the overall reaction is determined as:

$$E_{cell}^0 = E_{cathode}^0 - E_{anode}^0 = -0.26 \text{ V} - 1.23 \text{ V} = -1.49 \text{ V} \text{ vs SHE}$$
 (2.7)

SHE or Standard Hydrogen Electrode is the universal reference for measuring other standard cell potentials $(E^0)^{29}$. SHE consists of a Pt electrode in contact with 1 M solution of hydrogen ions H^+ (activity = 1) and the pressure of hydrogen gas H_2 is 1 bar or 1 atm 29 . The half-cell reaction is as follow:

$$2H_{(aq)}^+ + 2e^- \rightleftharpoons H_{2(q)}$$
 (2.8)

Thus, by convention, the electrode potential of SHE is $E_{SHE}^0 = 0.000 V$ at $25^{\circ} C^{29}$.

In electrochemistry, electrochemical cells convert chemical energy to electrical energy and that process requires a certain amount of energy from the electrochemical cell, w_{max} :

$$W_{max} = nFE_{cell} \tag{2.9}$$

 w_{max} is the work being done by the system and has a negative value. n is the number of electrons transferred in balanced equations. E_{cell} is the cell potential that measures the potential difference between the two half-cells in an electrochemical cell at non-standard condition. F is Faraday's constant.

The change in free energy or ΔG is expressed as the maximum amount of work that is required during the chemical process, so $\Delta G = -w_{max}$:

$$\Delta G = -nFE_{cell} \tag{2.10}$$

M.A.Sc Thesis - L. Lam; McMaster University – Engineering Physics

A more negative ΔG means a more spontaneous redox reaction ³⁰.

When both reactants and products are in standard states (1 atm, 298.15K), Eq. (2.10) becomes:

$$\Delta G^0 = -nFE_{cell}^0 \tag{2.11}$$

Moreover, the standard free-energy change is related to the equilibrium constant according to the following equation:

$$\Delta G^0 = -RT lnK \tag{2.12}$$

where K is the equilibrium constant. In the case of nonstandard conditions, ΔG can also be rewritten in the form:

$$\Delta G = \Delta G^0 + RT lnO \tag{2.13}$$

where Q is the reaction quotient used in a non-equilibrium reaction. Recalling that $\Delta G = -nFE_{cell}$, we get:

$$-nFE_{cell} = -nFE_{cell}^{0} + RTlnQ (2.14)$$

Dividing both sides by -nF gives:

$$E_{cell} = E_{cell}^0 - \left(\frac{RT}{nF}\right) lnQ \tag{2.15}$$

Eq. (2.15) is the Nernst equation which can be used to determine the value of E_{cell} at any condition. The minimum cell voltage at experimental conditions is approximately 1.22 V. In practice, due to kinetic overpotentials and IR voltage drops, the working cell voltage needs to be greater than this minimum cell voltage. Consequently, the range of voltage 2.0 V - 3.0 V is appropriate depending on deposition rate and coating morphology, which will be discussed in more detail later.

2.3 Factors in Electrodeposition

The amount of depositing metal can be controlled by many factors such as bath composition, pH, temperature, current density, deposition duration, and coating thickness ³¹. Nevertheless, the basic operation of electrodeposition remains similar. The deposition process is based on the flow of electrons from an external power supply. In an electrolytic cell, the cathode is connected to the negative terminal of an external potential source and the anode is connected to the positive terminal of the potential source. ²³ Negatively charged anions are attracted towards the anode and positively charge cations move to the cathode. As a result, to neutralize charges, anions at the anode need to lose electrons through the oxidation process and cations at the cathode need to gain electrons through the reduction process ^{23,31}.

2.3.1 Bath Composition

A bath typically consists of solvents and solutes. It is obvious that solutes impact directly on the plating result as they determine what material is eventually being plated. The ability of a solvent to dissociate solutes to ions determines whether electrochemical deposition occurs or not, as it provides the medium and allows ions to move in electrochemical reactions, enabling the process to occur.

2.3.2 Bath pH

pH is used to measure the hydrogen ion concentration in a solution ²⁸. Lower pH means a more acidic solution. ²⁸ In the Ni plating process, pH is a crucial factor affecting the

performance of the bath solution. Changing pH in the bath could alter the equilibrium constant, which results in a shift in an equilibrium reaction.

Buffer H₃BO₃ is added to the solution to control the bath's pH by compensating the amount of hydrogen ions (H⁺) lost through hydrogen gas (refer to Eq. (2.2)). Therefore, it minimizes the rapid change in the acidity and controls pH via the reaction:

$$Ni^{2+} + 2 H_3 BO_3 \rightarrow (H_2 BO_3)_2 Ni + 2H^+$$
 (2.15)

Besides acting as a buffer, H_3BO_3 also has a catalytic effect due to its ability of lowering the over-potential and increasing current efficiency 32,33 . H_3BO_3 forms borate ions $(B(OH)_4^-)$ in the aqueous solution. When the solution becomes more acidic, $B(OH)_4^-$ combines with H+. According to Le Chatelier's principle, the equilibrium (Eq. (2.15)) shifts to the left to reduce H+, then reform H_3BO_3 again. The dissociation of boric acid in water at room temperature is $pK_\alpha = 9.2^{34}$.

$$B(OH)_3 + H_2O = B(OH)_4^- + H^+ \qquad pK_\alpha = 9.2$$
 (2.16)

H₃BO₃ can reduce the over-potential as it forms a complex compound with Ni ions that facilities metal deposition, ³³ reduces the required activation energy, and so decreases the overpotential of Ni deposition. ³⁵ The reaction that occurs is:

$$Ni^{2+} + 2\begin{bmatrix} HO & OH \\ B & HO \end{bmatrix}$$
 HO NI B HO OH HO OH HO OH HO OH HO OH (2.17)

H₃BO₃ not only decreases the over-potential but also increases current efficiency ^{32,33}. Current efficiency is determined by the ratio of the actual current to the calculated current from Faraday's law ³⁶. In other words, it measures the yield of electric current that contributes to the desired chemical reaction. In the Ni solution, H₃BO₃ prevents the

formation of insoluble Ni(OH)₂ on the surface ³², increasing the amount of Ni²⁺ ions in solution and the conductivity, so improving current efficiency. In this work, the Ni plating bath consists of 5.625 g of NiCl₂·6H₂O and 0.75 g of H₃BO₃ dissolved in 35 mL of water.

2.3.3 Temperature

Temperature can affect the performance of Ni plating, especially the brightness range, throwing power, ductility, hardness, internal stress, and burning characteristics ²⁸. The Nernst equation (Eq. (2.15)) illustrates that the temperature directly influences the value of cell potential and can shift the direction of the reaction as well. In this project, the temperature is maintained in the desired range (room temperature to 70°C) and checked by probe meter before and after the deposition.

2.3.4 Current Density

Current density controls the rate of deposition and the uniformity of coating. According to Faraday's law, the deposition current density is directly related to the thickness of deposited material. Current density (J) determines the result of total current I, applying on the electrode's surface area (A):

$$J = \frac{I}{A} \tag{2.18}$$

Moreover, Faraday's law can predict quantitatively the weight of deposited layer W from electrochemical equivalent Z (defined below), I, and deposition time t:

$$W = ZIt (2.19)$$

Faraday's law states that the amount of electricity transported by the flow of one ampere in one second has the value of 96,487 Coulombs per mole (C/mol) or 26.799 Amperehours and is denoted as F. Faraday's constant (F) can be determined by:

$$F = N_A e \tag{2.20}$$

where N_A is the Avogadro constant (6.0225 x 10^{23} molecules/ mol) and e is the charge of one electron (1.6021 x 10^{-19} Coulombs):

$$F = 6.0225 \times 10^{23} \times 1.6021 \times 10^{-19} = 96,487 \text{ C/mol}$$
 (2.21)

The electrochemical equivalent Z is the deposited or liberated mass at an electrode per one coulomb of electricity in electrochemical reactions ³⁷. Z is equivalent to the molar mass m_a , divided by n electrons involved in the chemical reaction times the Faraday constant F:

$$Z = \frac{m_a}{n_F} \tag{2.22}$$

Substituting the atomic weight of Ni (58.70 u) and the electron number 2 gives the following equation:

$$Z = \frac{58.70 \text{ g/mol}}{2 \times 26.799 \text{ C/mol}} = 1.095 \text{ g/C}$$
 (2.23)

Thus, the weight of Ni deposited in grams at the cathode at 100% current efficiency and one Ampere-hour can be quantitatively determined by:

$$W = 1.095 It (2.24)$$

In addition to current density, current flow also needs to be considered. Current flow between electrodes is affected by a solution resistance which depends on the ionic conductivity of the electrolyte and geometric arrangement of the electrodes such as the disk electrode and parallel planar electrode ^{23, 24}. In micro disk configuration, resistance increases when electrode is smaller, and resistance decreases when two electrodes get closer in parallel planar electrode configuration. The distance between electrodes could affect the uniformity of the final coating. So, the distance between electrodes should be fixed in order to achieve the uniform current density during the electroplating process ²⁶.

2.3.5 Duration of Deposition and Thickness

The deposited thickness is derived by considering the volume of deposit. The formula to find the volume V is V = hA in which h is the height or thickness and A is the surface area to be electroplated. The volume can also be determined by the relationship with weight of deposit W and the density d, $d = \frac{W}{V}$. Thus,

$$h = \frac{V}{A} = \frac{W}{Ad} \tag{2.25}$$

The density of Ni is 8.907 g/cm³ and the weight of Ni deposit was already defined in Eq. (2.25). This gives:

$$h = \frac{W}{Ad} = \frac{1.095 \, lt}{A \times 8.907} = 0.1229 \frac{lt}{A} = 0.1229 Jt \tag{2.26}$$

Eq. (2.26) can be rewritten in other units of time in hours, area in dm^2 and thickness in mm. As a result, the average thickness h in Eq. (2.27) in mm is:

$$h = 0.1229Jt \times 10^2 = 12.294Jt \ \mu m$$
 (2.27)

where J is the current density through the substrate in units of Amperes/dm², and t is the duration of deposition in units of hours. By keeping surface area fixed through design, Eq. (2.27) can determine the deposited thickness through time of plating and the current density being used with the assumption of 100% cathode current efficiency. The assumption of maintaining a constant surface area is made not only for mathematical simplicity but also to facilitate NW deposition.

2.4 Electroplating on Si Substrate and NWs

Electroplating is a cost-effective and facile method that enables precise metal deposition on NWs. Prior to fabrication, chemical etching of semiconductors is a critical step used to remove the native oxide layer and other contaminants from the surface. In this experiment, Ni is electroplated onto Si substrates. Si readily oxidizes even at room temperature upon exposure to air, forming an amorphous silica (SiO₂) layer ³⁸. This layer stabilizes the Si-based substrate and prevents further chemical reactions. Therefore, removing it before electroplating is necessary. Native oxides are also naturally formed on the NWs' facets. Etching the substrates and NWs will remove the native oxide ³⁹. This etching step is crucial to enable the subsequent electroplating reactions.

2.4.1 Etching

Our experiments included the deposition of Ni on Si or NWs grown on Si substrates. In this case, hydrofluoric acid (HF) or buffered oxide etch (BOE) was used to remove the unwanted oxide layer on the surface of Si. BOE is a mixture of hydrofluoric acid and ammonium fluoride. Ammonium fluoride (NH₄F) makes the Si surface smoother than HF with less oxygen and carbon on the Si surface comparing to HF or BHF. ⁴⁰ The process is illustrated through the following chemical reaction:

$$SiO_{2(s)} + 6HF_{(l)} \rightarrow H_2SiF_{6(aq)} + 2H_2O_{(l)}$$
 (2.28)

where H₂SiF₆ is soluble in water. When HF is introduced to the Si surface, it inserts into the bonding of Si due to polarization and leads to the fluorination of Si surface while the hydrogenation happens with another Si atom:

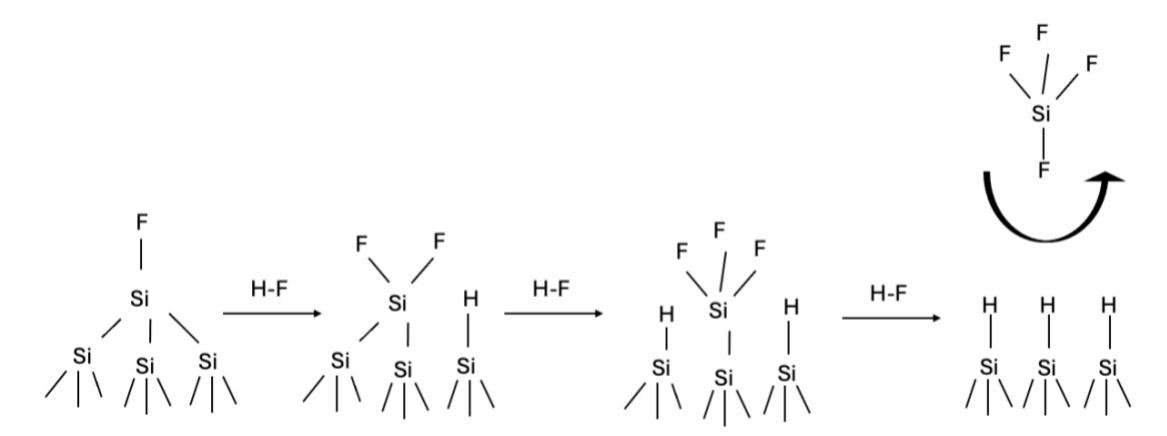


Figure 2.1. The mechanism of hydrogen passivation ⁴¹.

By introducing HF, the process of hydrogenation will take place over the surface of Si and results in the hydrogen passivation on Si surface ⁴¹. The etching process is divided into two steps: water molecules from solution initially oxidize the hydrogen-terminated Si surface, and HF molecules rapidly removes the newly formed oxide layer ⁴¹. This explains why buffer HF can etch the surface better and faster.

However, this surface after etching is highly hydrophobic which is a problem for electroplating occurring in an aqueous solution. Thus, after etching, the Si substrate can be rinsed with water. The hydroxyl group in water replaces hydrogen on the surface with the hydroxyl group. Nevertheless, water does not have much hydroxyl group, and it causes some contamination problems. Previous research has shown that the amount of F and C increases after rinsing the surface with water ⁴¹. Water rinsing also introduces oxygen on the surface affecting the electrical behaviour of bonds ⁴¹. A better method is to wash the Si substrate in alcohol such as ethanol or isopropanol after rinsing with water. The direct displacement makes the surface more bondable and less contaminated, and ready for the next step - electroplating.

Meanwhile, for GaAs NWs grown on GaAs substrate, the more suitable etching solution is hydrochloric acid (HCl). HCl is highly effective for removing the native oxide layer on GaAs NWs (Ga₂O₃ and As₂O₃) because it selectively dissolves these oxides into readily soluble chloride complexes - namely, GaCl₃ and AsCl₃ without significantly attacking the underlying GaAs substrate when used in proper dilution. The key reactions are:

$$Ga_2O_3 + 6HCl \rightarrow 2GaCl_3 + 3H_2$$
 (2.29)

$$As_2O_3 + 6HCl \rightarrow 2AsCl_3 + 3H_2O$$
 (2.30)

This results in an oxide-free surface that enhances subsequent metal adhesion and minimizes interface resistance. X-ray photoelectron spectroscopy (XPS) and ellipsometry studies confirm that HCl etching can reduce oxide thickness from several nanometers to less than one nanometer, achieving clean, Ga-rich surfaces ideal for further processing ⁴².

2.4.2 Electroplating on Si Substrate and NWs

The silver paste or the EPO-TEK® H20E was used to conduct charge carriers from the Si substrate or NW substrate. Silver paste is a 1:1 ratio mixture of EPO-TEK H20E part A (containing silver and epoxy phenol novolac resin) and EPO-TEK H20E part B (containing silver, reactive diluents, substituted imidazole). ⁴³ The epoxy mixture is electrically conductive and designed for bonding in microelectronic and optoelectronic applications.

2.4.2.1 Direct current (DC) Electrodeposition

The bath solution was thoroughly mixed using a magnetic stirrer. The temperature was maintained between 50 °C and 70 °C using a hot plate. Ni electroplating onto Si and NWs

using DC followed standard electroplating principles. The applied current was in the milliampere (mA) to the microampere (μ A) range, with the voltage set above 0.7 V-the threshold voltage for Si - and above 2.24 V for GaP, enabling current conduction in the forward direction ⁴⁴.

Initially, current was supplied using a KORAD KD3005D DC power supply, ⁴⁴ which offers a resolution of 1 mA ⁴⁵. However, to achieve finer current control in the μA range, a Keithley 2400 SourceMeter was employed ⁴⁶. The SourceMeter provides a more stable and lower-noise DC signal with up to 5-digit resolution, making it more suitable for sensitive electroplating processes.

The DC electroplating setup is illustrated in Figure 2.2. The black arrow indicates the direction of conventional current, while electrons flow in the opposite direction—from the negative to the positive terminal. In other words, electrons flow toward the Si substrate/NWs, rendering them negatively charged and attracting Ni²⁺ cations. Simultaneously, electrons flow away from the Pt electrode, making it positively charged and attracting Cl⁻ anions.

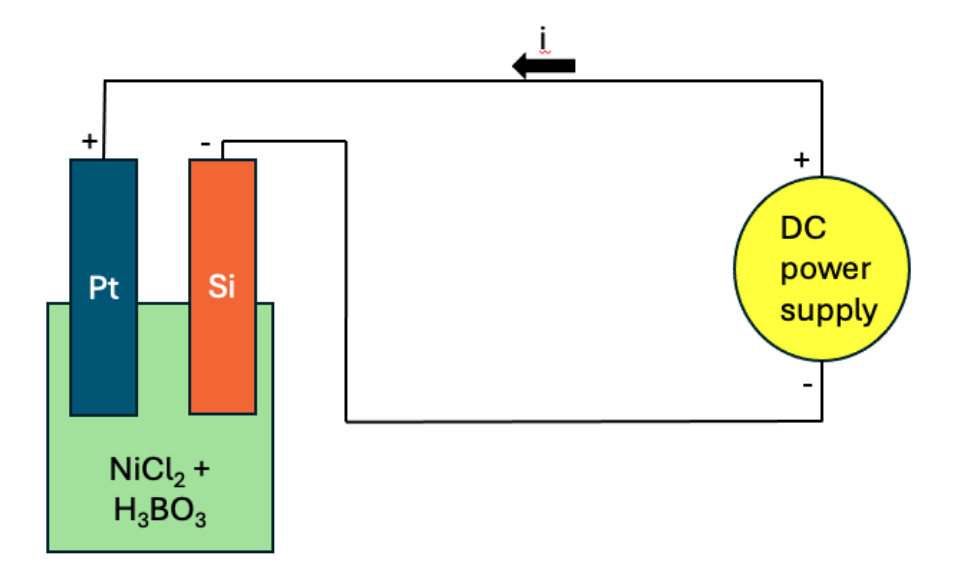


Figure 2.2. The schematic representation of set up for Ni plating using DC source.

2.4.2.2 Pulse Electrodeposition (PED)

The concept behind using a pulsed signal instead of DC in the electroplating process lies in the time-dependent nature of the pulse waveform. Unlike DC, a pulsed voltage alternates between two states: "on," where the voltage is applied for a duration defined as the time on (t_{on}) , and "off," where the voltage is removed for the time off (t_{off}) . The total period (T) is the sum of t_{off} and t_{on} and the reciprocal of the period gives the frequency (f) of the pulse signal.

Achieving a uniform coating onto NWs using standard DC electroplating is challenging. To address this issue, PED has been proposed as an effective alternative. For instance, Monaico et al. demonstrated that PED can achieve conformal Pt coating on InP NWs 40 . To generate the desired pulse signal, an external circuit was designed and assembled. The circuit consists of a 555 timer, an inverter, and a comparator. The 555 timer was configured in astable mode, which provides a continuous output waveform and is better suited for electrochemical applications than the single-pulse behavior of monostable mode. An astable 555 timer requires two resistors and one capacitor, with their values selected based on the desired t_{on} , t_{off} , and f.

Initially, the design aimed for a short t_{on} and long t_{off} , allowing metal ions sufficient time to reach the pore depth. However, this configuration proved difficult to implement due to the internal design constraint of the 555 timers. As a result, a more practical approach was adopted by using a long t_{on} and short t_{off} , then inverting the signal to achieve the desired behavior, necessitating the use of an inverter.

The comparator functions as a voltage amplifier. The comparator adjusts the signal to match the voltage requirements for the electrochemical process. The negative voltage favors nucleation and ameliorates the ionic mobility ⁴⁷.

The circuit and the experimental setup are shown in Figure 2.3 and Figure 2.4, respectively. An example of the frequency calculation follows using the parameter values in Figure 2.3:

$$t_{on} = \ln 2 \times (R_1 + R_2) \times C_1 = 0.639 \times (10^6 + 100) \times 1.47 \times 10^{-6} = 1.019 \text{ s}$$
 (2.31)

$$t_{off} = \ln 2 \times R_2 \times C_1 = 0.693 \times 100 \times 1.47 \times 10^{-6} = 101.9 \,\mu\text{s}$$
 (2.32)

$$f = \frac{1}{t_{on} + t_{off}} = \frac{1}{\ln 2 (R_1 + 2R_2) \times C_1} = \frac{1.44}{(10^6 + 2 \times 100) \times 1.47 \times 10^{-6}} = 0.9794 \, Hz$$
 (2.33)

The time on, time off, and frequency were adjusted depending on NWs array's size and experimental conditions.

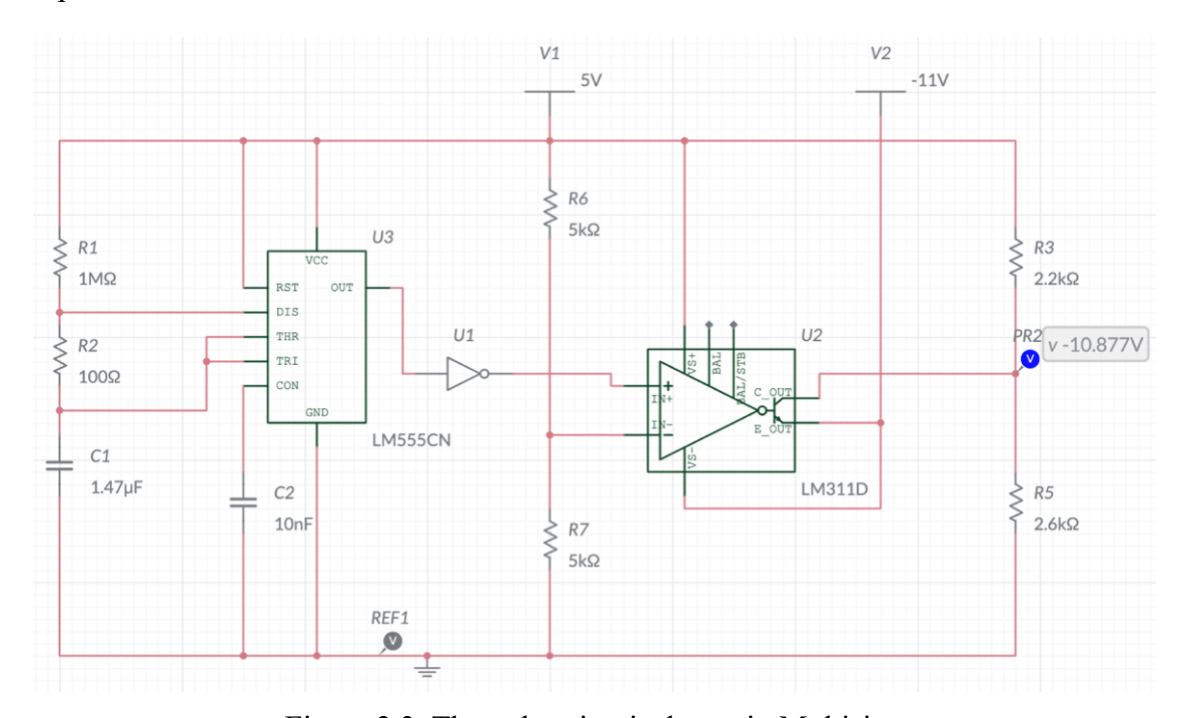


Figure 2.3. The pulse circuit shown in Multisim.

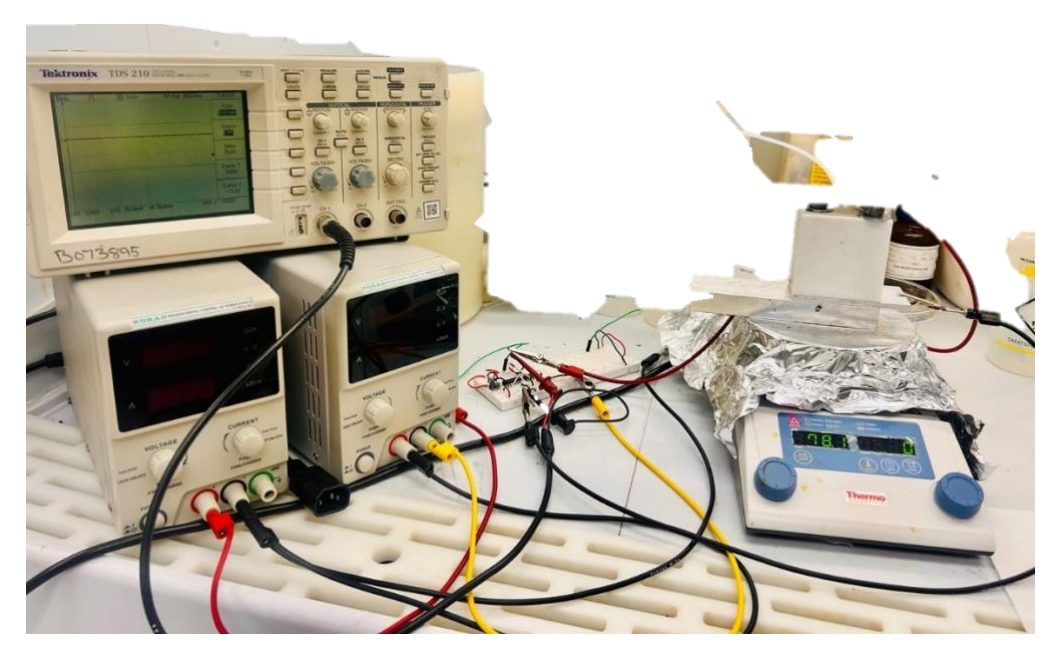


Figure 2.4. The experimental setup implementing pulse current signal.

Chapter 3 Design Evolution

Before Ni deposition was attempted on NWs, experiments were first performed on Si substrates. This chapter presents a series of experimental designs aimed at achieving uniform Ni coating on Si substrates. Three primary setups were evaluated: (iteration 1) a simple electrolytic cell using a glass beaker, (iteration 2) a commercial sealed electrolytic cell, and (iteration 3) a customized Teflon cell. Each configuration exhibited unique advantages and limitations—such as substrate contacting, electrode positioning, and the geometry of the Pt anode. These variables affected current efficiency, the likelihood of Ni flaking, experimental reproducibility, and coating uniformity. Among the approaches, iteration 1 yielded the poorest results, while iteration 3 (customized Teflon cell) produced the most uniform and reliable Ni coating. Each successive design was developed as an evolutionary improvement over the preceding setup, addressing identified limitations to enhance performance.

3.1 Iteration 1: Glass Beaker

In this first iteration of electrodeposition, Si substrates were bonded to a Cu sheet (refer to Figure 3.1) using Ag paste. Before each experiment, the n-type Si (100) substrate was cleaved into 1 cm × 1 cm squares, etched using buffered oxide etch (BOE) as described in section 2.4.1, and bonded to a Cu sheet using silver epoxy. The assembly was then cured at 120 °C for 15 minutes on a hot plate. To ensure good contact with the Si substrate, the Cu sheet was mechanically flattened using a hammer. In the initial design, the Si substrate, affixed to the thin Cu sheet, was wrapped with Cu wire as shown in Figure 3.1. Each Cu wire was coated with an insulating enamel. The enamel coating on both ends of the Cu wire was removed to establish electrical contact, while the remaining enamel acted

as an insulating layer to prevent unwanted electroplating in the Ni solution. However, since Cu is significantly more conductive than Si, Ni tended to deposit on the Cu sheet rather than on Si itself, making it more difficult to achieve Ni coating on Si.

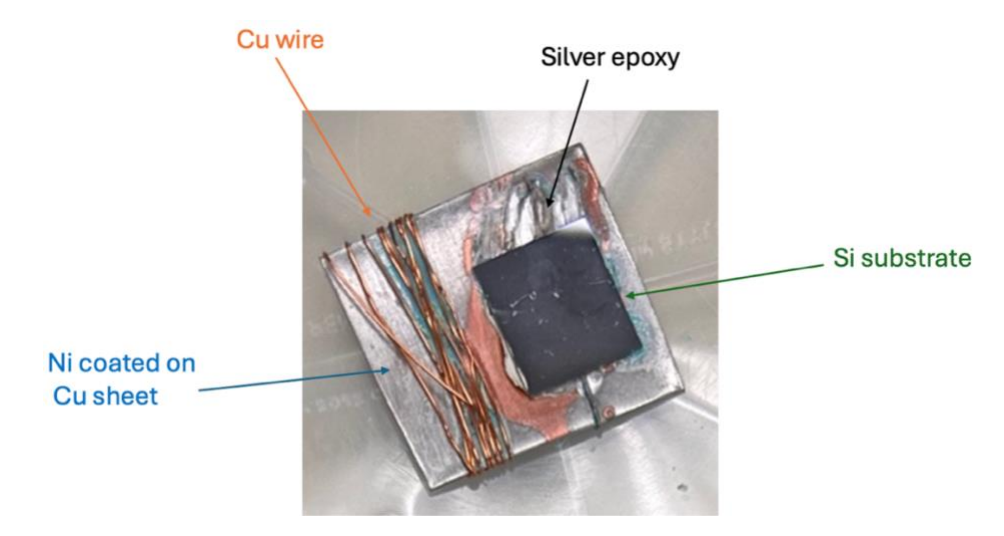


Figure 3.1. The electrical contact of Si with Cu wire through a thin Cu sheet.

The anode consisted of a thin cylindrical Pt wire (AWG 30) with a diameter of 0.25 mm and a length of 1 mm. Hydrogen bubble accumulation on the Pt wire increases ohmic resistance and overpotential, reduces the active electrode area, and hinders mass transport.

43 These effects ultimately decrease the efficiency of the plating process.

The electrolyte bath consisted of 225 g/L of NiCl₂·6H₂O and 30 g/L of H₃BO₃, dissolved in deionized water. The concentrations of Ni ions and H₃BO₃ were kept constant across all experiments to isolate the effects of other parameters such as plating duration and applied current.

Following substrate and solution preparation (Figure 3.2), the electroplating process was carried out on a hot plate at 50 °C. As shown in Figure 3.2, two alligator clips were attached to the edge of a beaker to secure the electrical connections to the voltage supply. The Cu sheet supporting the Si substrate was submerged in the electrolyte and positioned

above a magnetic stirrer. Voltage measurements were performed using a multimeter by connecting probes to each terminal.

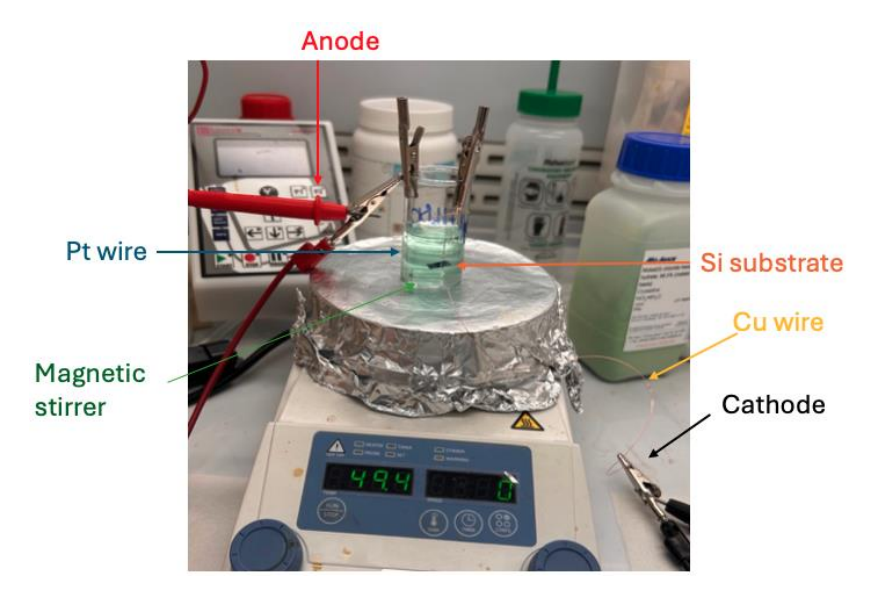


Figure 3.2. The design of wrapping Si substrate with Cu wire in a beaker. Alligator clips were used to provide stability and establish electrical connection with the power supply.

This initial design had several drawbacks. Various positions of the Si substrate affected both consistency and reproducibility of the experiment. It was also observed that the Cu sheet was sometimes displaced from the wire wrapping because of the magnetic stirrer underneath, which caused the loss of electrical connection with the cathode. As a result, Cu wire is not the best choice to establish interconnection between Si substrate and the cathode.

The Pt wire, due to its limited surface area, retained a significant number of hydrogen bubbles, further reducing coating uniformity. While vigorous stirring with a magnetic stirrer was employed to dislodge bubbles, this method was not entirely effective. Moreover, with this setup, both the front and back surfaces of the Cu sheet were exposed

to the plating solution, making it difficult to maintain a constant plating area - an assumption crucial to Eq. (2.25).

3.2 Iteration 2: Sealed Electrolytic Cell

The next iteration used a sealed electrolytic cell purchased from Stony Lab. The Si substrate was secured by a Stony Lab Cu sheet electrode (NY-PTFE-Electrode Holder Cu) as shown in Figure 3.3. The Si substrate was placed between the Cu sheet of the electrode and a polytetrafluoroethylene (PTFE) bolt (refer to Figure 3.3 and 3.4). This contact method offered more stable and consistent position of the substrate than the wrapping contact method in section 3.1. and limited the surface area of exposed Cu.

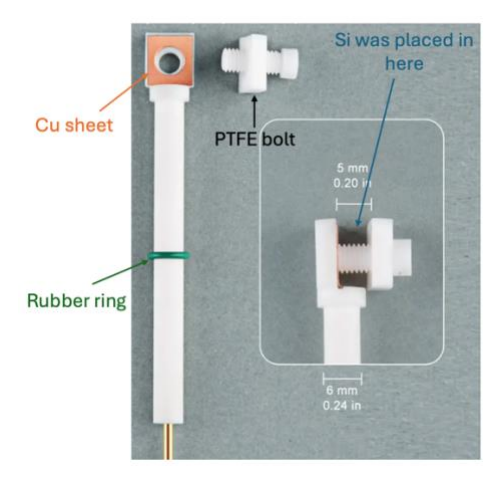


Figure 3.3. Stony Lab copper sheet electrode holder.

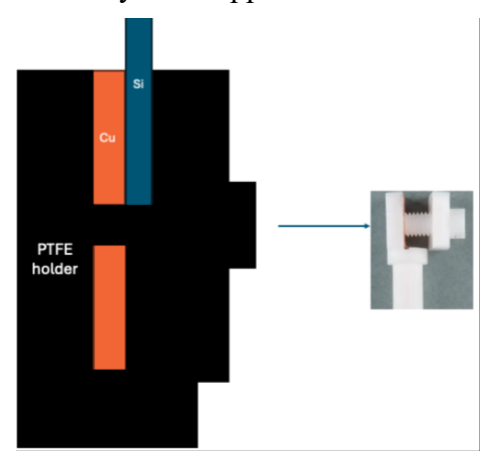


Figure 3.4. Schematic cross-section of Si attached to Cu sheet electrode holder.

As shown in Figure 3.5, the sealed electrolytic cell from Stony Lab (NY-D-ElectrolyticCell-50ml) offered the advantage of a fixed distance (approximately 2 cm) between the Pt electrode and the substrate, enhancing experimental consistency. This design used a Pt sheet instead of a Pt wire. The Pt sheet's surface area (204 mm²) was more rigid and had a well-defined geometry, offering a flatter and approximately 255 times larger surface area than the Pt wire's surface area (0.801 mm²) from the previous design. These characteristics made it more suitable for achieving uniform coating and enhancing reproducibility.



Figure 3.5. The design of sealed electrolytic cell.

Temperature and pH were monitored in real time using probes immersed in the solution during the process. A small plastic tube was incorporated into the setup to allow gas to escape, as illustrated in Figure 3.6. Moreover, this configuration proved superior to the earlier design that involved wrapping Cu wire around the substrate. Unlike the unstable suspension method shown in Figure 3.2, the new approach securely attached the substrate to the Cu sheet of the electrode holder (orange area in Figure 3.4) using mechanical force applied by a PTFE bolt. This improvement enhanced the overall stability of the setup and increased the reproducibility of the experiment.

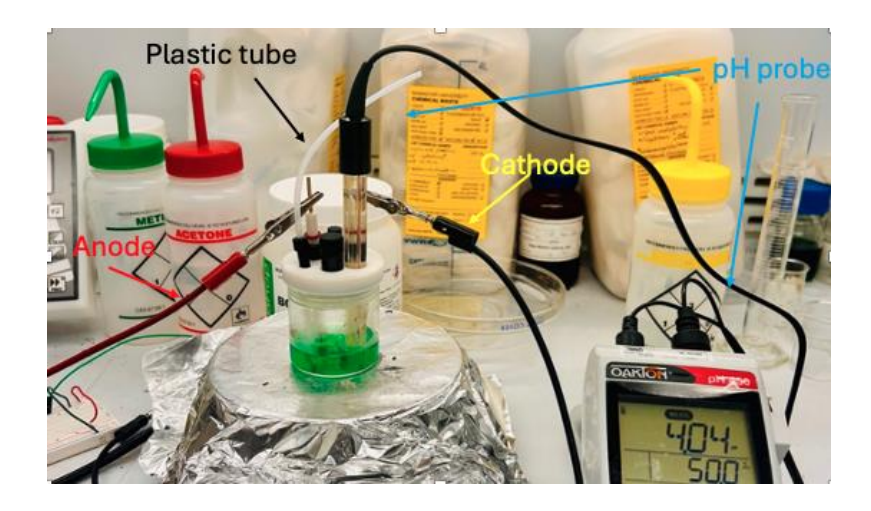


Figure 3.6. The experimental setup using sealed electrolytic cell as deposition method.

However, the setup shown in Figure 3.6 presented several challenges, including bubble formation on the Pt anode and difficulty preventing deposition on the backside of the Si substrate. Various approaches were attempted, such as masking the backside with Kapton tape and S1808 photoresist (0.8 µm thickness). However, both methods introduced new complications by compromising the electrical contact between the Si substrate (cathode) and the Cu sheet of the electrode. Prolonged exposure to the electrolyte weakened the adhesive strength of the Kapton tape. While S1808 photoresist adhered in aqueous environments, the electrical connection between the substrate and the electrode holder was compromised. As shown in Figure 3.4, simply pressing Si and Cu together did not yield reliable electrical contact, reduced coating uniformity, and occasionally caused the Si substrate to crack.

3.3 Iteration 3: Customized Teflon Cell

To address the challenges associated with the sealed electrolytic cell - particularly the issue of unwanted backside coating - a new cell design was developed to localize the plating area exclusively to the top surface of the substrate. Figure 3.7 depicts the cross-

section of the Teflon customized cell with a 2.77 mm diameter hole drilled at the bottom to expose the plating area. A 108 nitrile O-ring (B1000-108) was inserted around the hole, and the substrate was compressed against the O-ring and an Al plate to prevent electrolyte leakage. As shown in Figure 3.7, silver paste and the Al plate were used to establish a reliable electrical pathway from the cathode to the Si substrate, ensuring efficient current conduction.

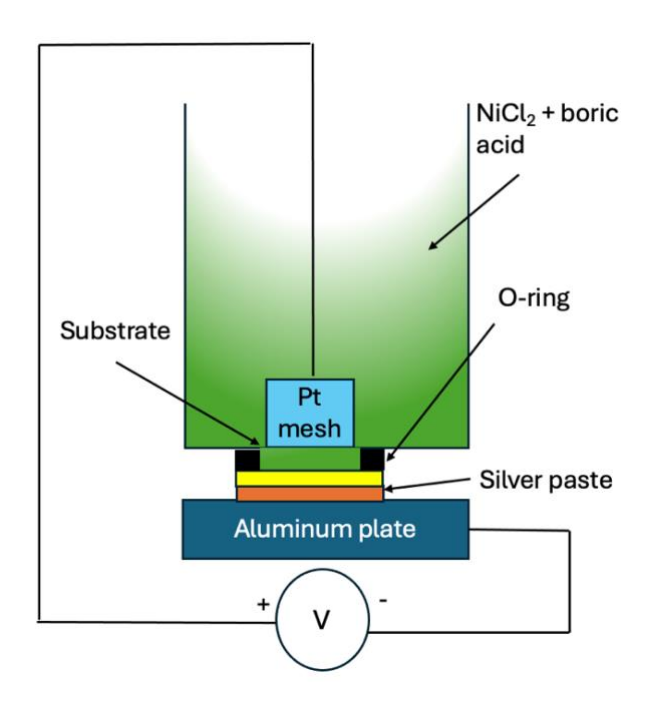


Figure 3.7. The schematic representation of cross-section view of the customized Teflon cell.

Another improvement in this design is the replacement of the Pt sheet with a Stony Lab Pt mesh (NY-PT-MeshElectrode-10x10), which offers the highest surface area (235.6 mm²) among the three design iterations due to its porous, three-dimensional structure. Pt mesh is particularly advantageous in this project where gas-evolving reactions occur, as its structure enhances ion transport and reduces gas bubble accumulation. The gap between the Pt mesh and the substrate was approximately 2.4 - 2.5 mm. This minimized

the distance between Si and Pt mesh electrode, so allowed higher current density, smaller voltage drop, and faster ion transport ^{48,49}.

This new configuration in Figure 3.8 retains the benefits of the sealed electrolytic cell, such as maintaining a fixed distance between the Pt mesh and the substrate and enabling gas release through a small plastic tube. It also resolves the primary limitation of the previous setup - unwanted backside coating. By repositioning the substrate to the bottom of the cell and exposing only the target surface through a drilled hole, the remainder of the substrate is shielded from the plating solution, thereby allowing selective-area electroplating. Moreover, the surface area of the hole (24.1 mm²) is fixed that leads to constant current density, improved reproducibility, and more consistent Ni film coating. To improve electrical contact to the substrate, 400 nm of Al was deposited on the back side of the Si substrate by sputtering using a Torr International planar magnetron sputtering deposition system. To prevent oxidation of the Al layer (Al₂O₃), an additional 200 nm layer of gold (Au) was sputtered onto the Al. The Au layer not only protected the Al from oxidation but also enhanced electrical connectivity with the Al plate, thereby improving current efficiency. Contact deposition was followed by rapid thermal annealing (RTA) at 400 °C for 30 seconds.

Although real-time monitoring of pH and temperature were not implemented with this design, these parameters can still be measured before and after plating. A potential future improvement could involve integrating a custom-built top-mounted stirring motor. However, this is not critical, as the low plating current allows most gas bubbles to escape effectively through the plastic tube (Figure 3.8).

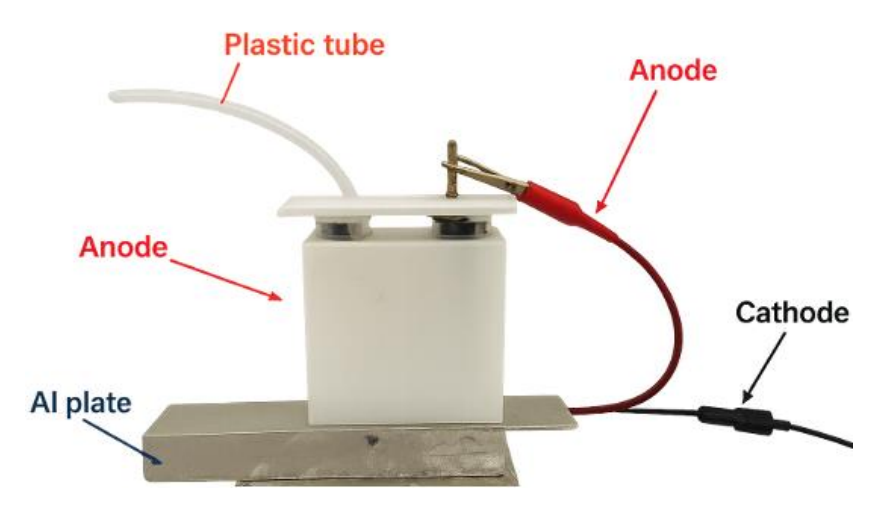


Figure 3.8. The customized Teflon electrochemical cell.

Chapter 4 DC Electrodeposition on Si Substrates

This chapter outlines the iterative development of Ni electroplating on Si substrates. Starting from a basic setup that demonstrated the feasibility of deposition but suffered from non-uniformity and poor adhesion, successive refinements improved coating control and reproducibility. The results show that Ni growth follows the Volmer–Weber mode, with deposition conditions, substrate type, and contact materials strongly influencing film morphology and stability.

4.1 Iteration 1

Although the initial experimental setup (section 3.1) using a glass beaker was relatively primitive, the scanning electron microscopy (SEM) results shown in Figure 4.1 illustrated that Ni was successfully coated on n-type Si (100) substrate. However, the Ni coating was not uniform, and it tended to accumulate near the edge of the Si substrate.

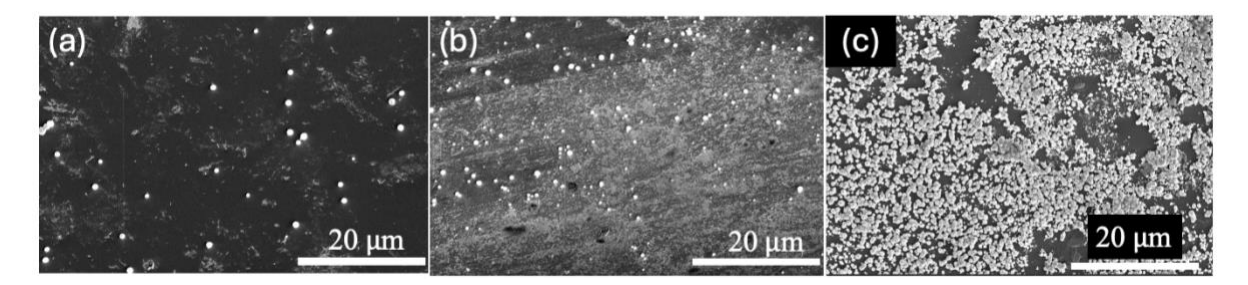


Figure 4.1. Non-uniform Ni deposition on Si in beaker setup, with edge accumulation due to poor current distribution with (a) SEM images of Ni coating on n-type Si substrate at 0.43 A, 3V, 50 °C for 136 s at different positions at the center, (b) near the center, and (c) at the edge (c).

Figure 4.2 shows a cross-sectional SEM image and energy dispersive x-ray (EDX) analysis obtained by cleaving the coated substrate, revealing Ni on the top surface of the

Si substrate. The reason for the presence of Ni on the cleaved surface of the substrate is unclear but may have occurred during the cleaving process.

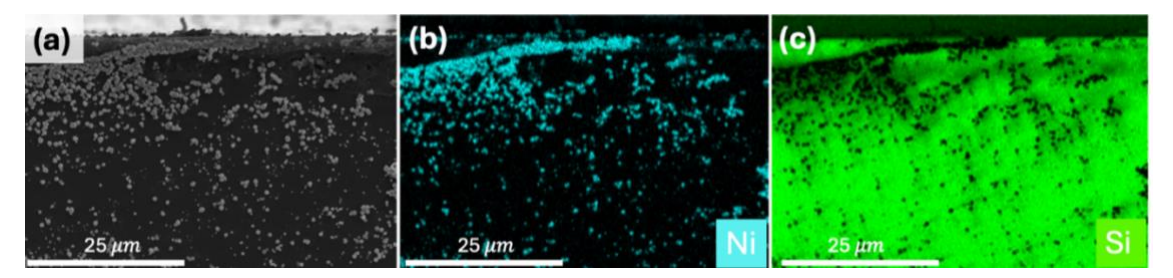


Figure 4.2. Cross-sectional view of the n-type Si substrate at 0.43 A, 3V, 50 °C, for 136 s. (a) SEM image of Ni coating on n-type Si. (b-c) EDX elemental maps showing distributions Ni (blue) and Si (green) respectively.

This deposition method led to unintended Ni deposition on the Cu sheet as shown in Figure 3.1. Because Cu has a higher electrical conductivity than Si, Ni preferentially deposited on the Cu surface rather than on the Si substrate. A significant portion of Ni ions in the solution was consumed in plating the Cu sheet, thereby reducing the efficiency of Ni utilization. Although the Cu sheet was cleaned with isopropanol and acetone before each experiment, there remained a high risk of introducing contaminants into the plating bath, potentially compromising the quality and consistency of the electroplating process.

4.2 Iteration 2

The electrolytic cell method (Section 3.2) was introduced to overcome the limitations of the previous design, such as unintentional Ni deposition on the Cu sheet, inconsistent positioning of the Si substrate, and non-uniform Ni coating. As shown in Figure 3.3, the electrode holder includes a Cu sheet that serves as an electrical contact with the substrate, but it is sealed with PTFE and secured with a PTFE bolt. PTFE is well-known for its thermal resistance, hydrophobic nature, and excellent insulating properties, making it suitable for electroplating processes.

Unlike the setup in Figure 3.1, the Cu sheet was no longer directly exposed in this design, reducing the issue of unintended Ni coating on the Cu. The electrode holder also ensured a fixed vertical position of the Si substrate relative to the Pt mesh counter electrode, as shown in Figure 3.5. This stable positioning improved coating uniformity and enhanced the reproducibility of the experiments.

Using this design, various experiments were conducted to control the thickness of deposited Ni on Si substrates. Current played a critical role in the electrochemical experiments, making it essential to examine its influence on the Ni coating layer. As shown in Figure 4.3, a higher current resulted in a thicker Ni coating - under identical conditions, the Si surface was coated with more Ni at 0.1 A compared to 0.025 A. However, when the current exceeded 0.1 A, the Ni coating began to flake off the surface, a phenomenon visible to the naked eye. This could be attributed to the rapid deposition rate at higher currents, which may lead to poor adhesion and subsequent peeling of the coating from the Si surface.

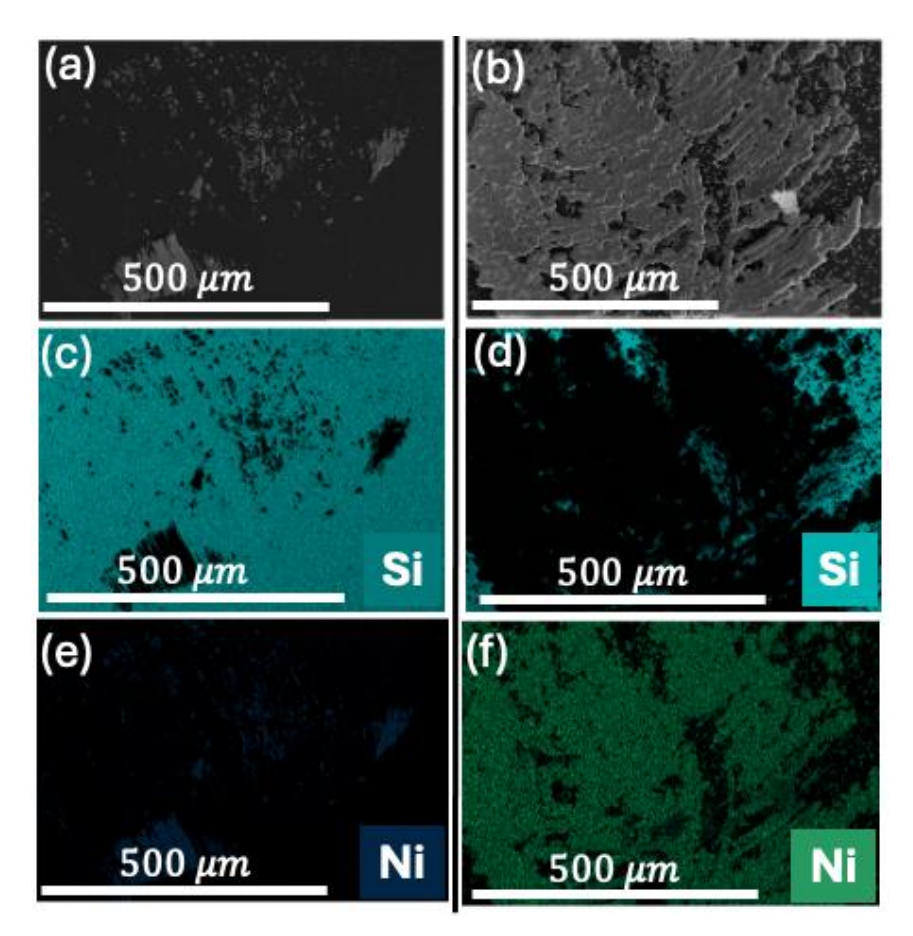


Figure 4.3. Effect of current on Ni thickness: higher current increases deposition but causes poor adhesion and flaking at 3V for 144 s at 58 °C. (a-b) SEM images of the coated n-type Si (100) substrate at 0.025 A and 0.1A respectively. (c-d) EDX elemental maps showing distributions of Si (teal) and Ni (blue) at current 0.025 A. (e-f) EDX elemental maps showing distributions of Si (teal) and Ni (green) at current 0.1 A.

Figure 4.4 depicts an experiment conducted by applying the same conditions (0.1A, 3V, 144 s, and 58 °C) on two n-type Si (100) samples. Figure 4.4 (a) and (b) were only etched with BHF, and Figure 4.4 (c) was rinsed with isopropanol alcohol (IPA) after BHF. An interesting event occurred in the sample that was rinsed with IPA. The coating of Ni increased significantly in the sample that was rinsed with IPA and could even be perceived by the naked eye as shown in Figure 4.5. Studies have shown that HF and alcohol-based treatments can effectively minimize surface residue and offer improved control compared

to conventional HF/H₂O processes, owing to the high vapor pressure of alcohol ⁵⁰. This might explain the higher deposition rate in the sample rinsed with IPA.

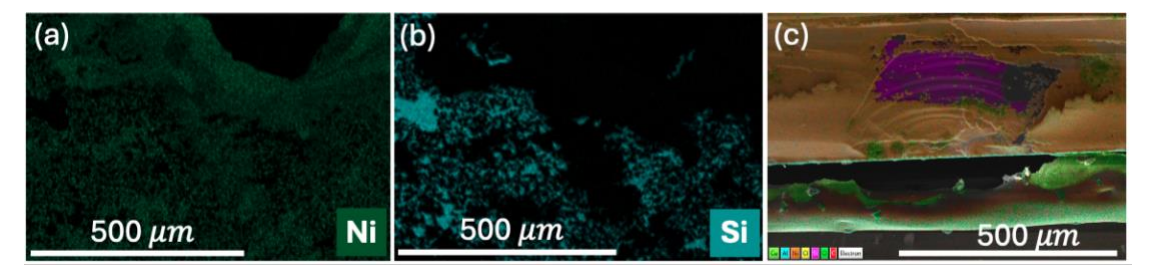


Figure 4.4. IPA rinse enhances Ni adhesion and coating uniformity, but excessive deposition still leads to peeling. Cross-section (tilted 15°) EDX of n-type Si substrate coated with Ni in which (a) and (b) are the results without rinsing with IPA and (c) is the result rinsing with IPA. Both samples were plated at 0.1A and 3V for 144 s at 58 °C.

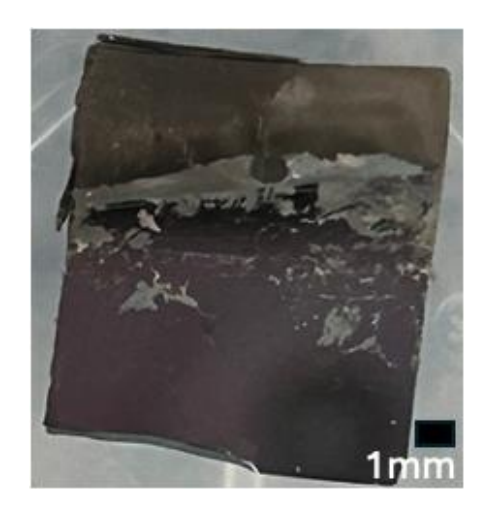


Figure 4.5. Image was taken by phone camera, showing peeling of the Ni film observed by naked eye.

After recognizing the benefits of IPA, Ni deposition experiments were repeated. Figure 4.6 shows that more Ni is deposited when the magnitude of current increases. The surface in Figure 4.6 (c) at the highest current started peeling off and can be observed by the naked eye. Thus, rinsing the surface with IPA can increase current efficiency and allow more controllability over the coating process.

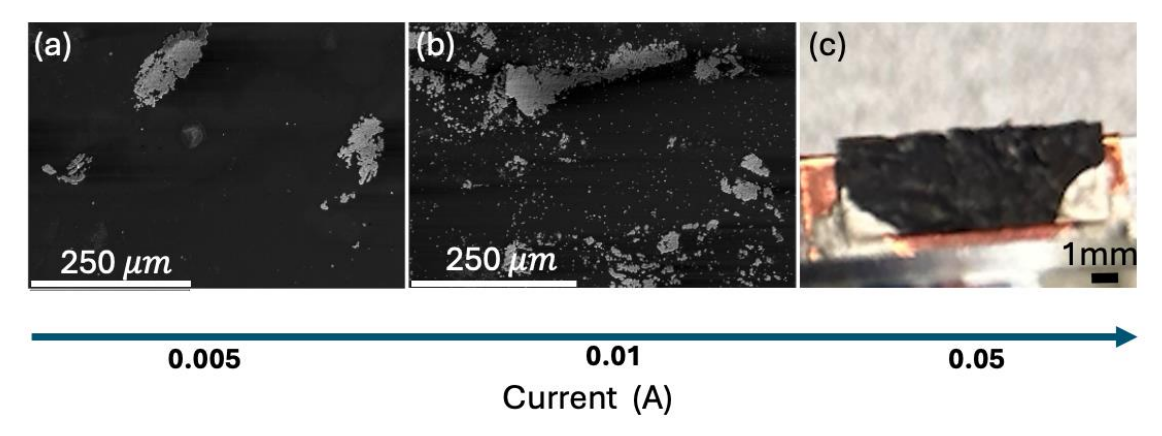


Figure 4.6. Ni growth on Si follows Volmer–Weber mode: particles coalesce into clusters with higher current. SEM images of n-type Si (100) substrate after rinsing with IPA and coated with Ni at (a) 0.005 A, (b) 0.01 A, and (c) photograph of n-type Si sample at 0.05 A.

4.3 Iteration 3

In this design iteration, three deposition experiments were performed with different deposition time on n-type Si (100) substrates. In this experiment, only Al was deposited on the back side of the Si substrate (no Au). Table 4.1 shows the deposition conditions.

Table 4.1. The experimental conditions for n-type Si (100) samples as deposition time increases.

Sample	Current	Voltage	Deposition	рН	рН	Temperature
	(mA)	(V)	time (s)	(before	(after	(°C)
				experiment)	experiment)	
a	0.49	1.93-1.89	60	3.65	3.65	24.1
b	0.49	1.90-1.86	120	3.65	3.53	24.1
c	0.49	1.91-1.85	300	3.65	3.55	24.1

Figure 4.7 and Figure 4.8 showed the plan view SEM and cross-section view SEM images, respectively, of the three samples (a, b, c) from Table 4.1. From these two Figures, it can be concluded that Ni particles tended to agglomerate as the experiment time continued. These results support the theory in section 1.2.3. that the growth mechanism of Ni on Si follows the Volmer-Weber growth mode.

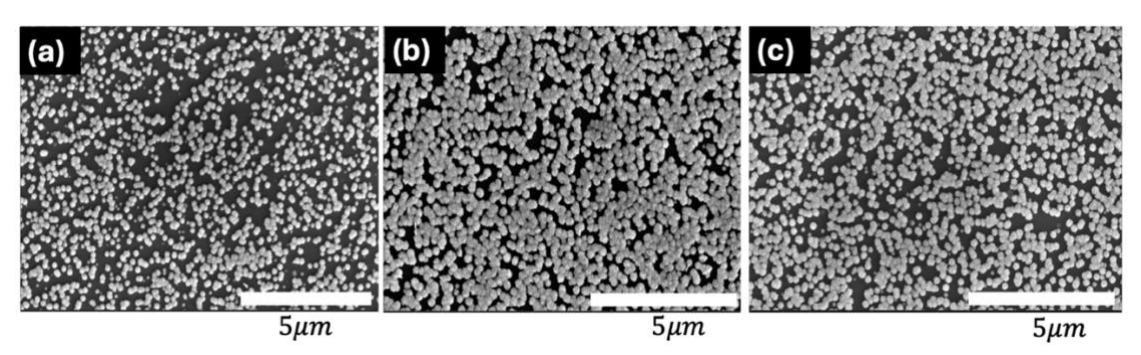


Figure 4.7. Ni growth on Si follows Volmer–Weber mode: particles coalesce into clusters with longer deposition times. SEM images of Ni electroplating on n-type Si (100) substrates back-coated with 400 nm of Al after (a) 60 s, (b) 120 s, and (c) 300 s.

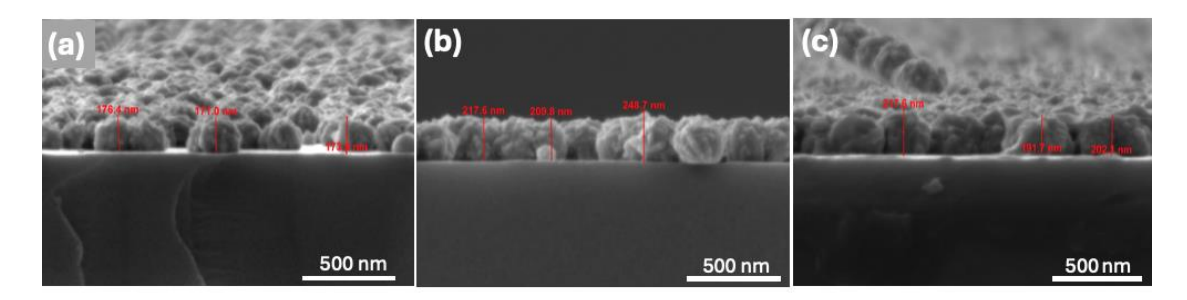


Figure 4.8. The cross-section SEM images of Ni electroplating on n-type Si (100) substrates back-coated with 400 nm of Al after (a) 60 s, (b) 120 s, and (c) 300 s.

The number of particles per unit area in cm², the percentage of Ni coverage area, and the average particle size in µm on n-type Si (100) were shown in Figure 4.9. The trend observed in Figure 4.9 (a) was that the number of Ni particles per cm² reduced as the depositing time increased, while the percentage of Ni coverage (Figure 4.9 (b)) and its average size in µm (Figure 4.9 (c)) increased. This numerical data also affirmed that Ni prefers to accumulate to a bigger cluster. The coverage has a limited range as the Ni film starts flaking off rather than filling in the voids.

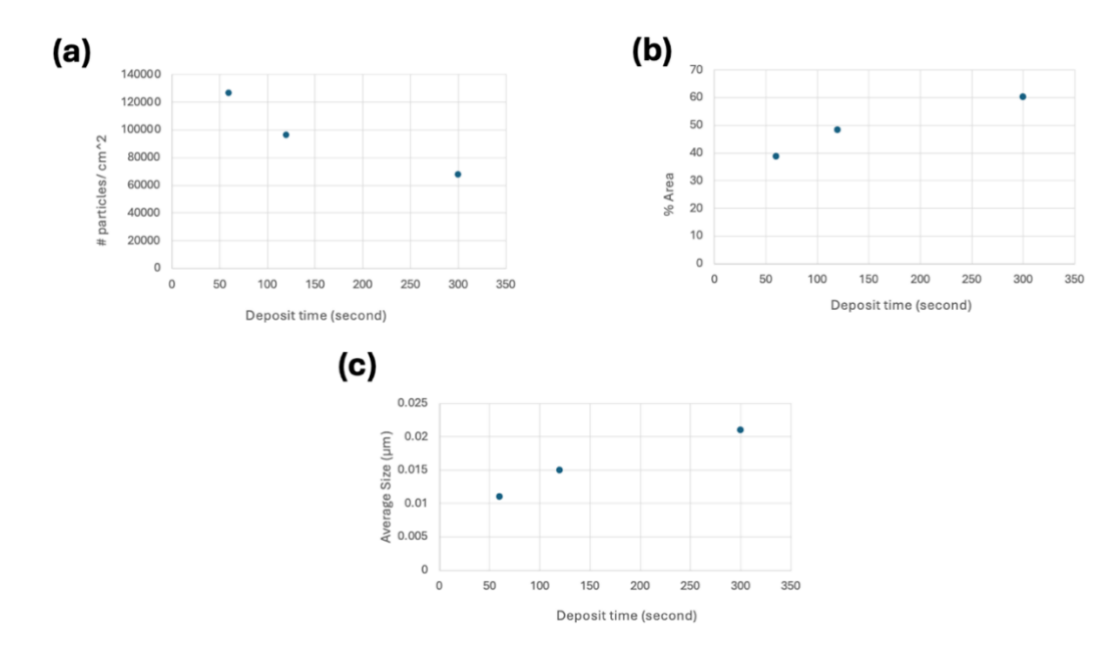


Figure 4.9. The plots of (a) number of Ni particles per unit area in cm², (b) percentage of Ni particle covered the surface of n-type Si substrate (100), and (c) The average size of Ni particles in μ m.

Trials were also conducted on p-type Si (111) substrates using Al/Au back side contacts with three different deposition times, as detailed in Table 4.2. The purpose of this experiment was to examine how deposition time affects the Ni coating layer on p-type Si (111) and to compare the results with those obtained for n-type Si (100). Another difference was the extra layer of Au underneath the Al layer. In addition to protecting Al from being oxidized, Au improved the electrical connection between Al/Si with the cathode terminal to achieve greater control over the coating's uniformity.

Table 4.2. The experimental conditions for p-type Si (111) samples as deposition time increases.

Sample	Current	Voltage	Depositing	рН	рН	Temperature
	(mA)	(V)	time (s)	(before	(after	(°C)
				experiment)	experiment)	
a	0.49	1.96-1.94	30	3.69	3.72	24.7
b	0.49	1.97-1.89	60	3.69	3.66	25.0
С	0.49	1.95-1.87	120	3.69	3.63	24.5

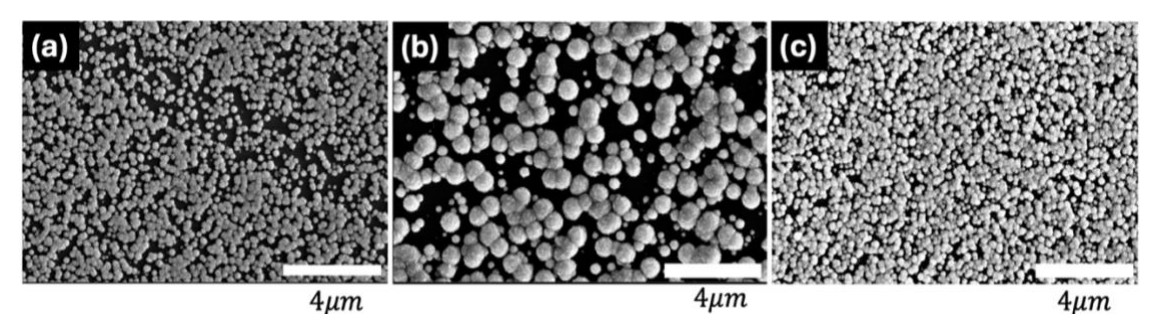


Figure 4.10. Faster Ni growth on p-type Si than n-type; at 120 s coatings peel due to excessive thickness. SEM images of Ni deposition on p-type Si (111) that was backcoated with 400 nm Al then 200 nm of Au at (a) 30 s, (b) 60 s, and (c) 120 s.

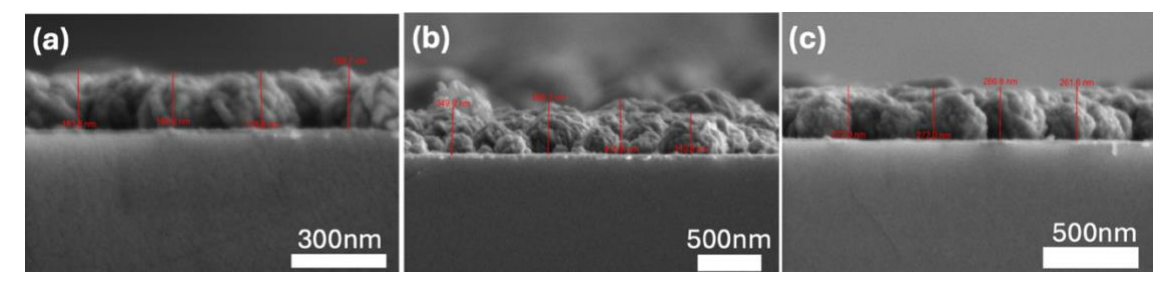


Figure 4.11. Cross-section SEM images of Ni deposition on p-type Si (111) that was back-coated with 400 nm Al then 200 nm of Au at (a) 30 s, (b) 60 s, and (c) 120 s.

The results are shown in Figure 4.10 - 4.11 From Figure 4.10, Ni islands initially grew larger as the deposition time increased. At 120s, Ni began to flake and detach from the ptype Si surface, visible as floating flakes in the solution and the cross-section SEM images from Figure 4.12. In the case of n-type Si, the flaking phenomenon occurred at 300 s. In Figure 4.10 (b) and (c), Ni islands appear to merge and form a thin film. When the film became too thick, it detached from the substrate. The number of particles per unit area in cm², the percentage of Ni coverage area, and the average particle size in µm on p-type Si (111) are shown in Figure 4.13. The decline in thickness at 300 s may be explained by the initiation of a new Ni layer after flaking. That explained why the average size of Ni at 120 s was smaller than 60 s and 30 s. Overall, to obtain more manageable coating results, the current magnitude possibly needed to be reduced if Al/Au continued to be used on p-type (111) Si.

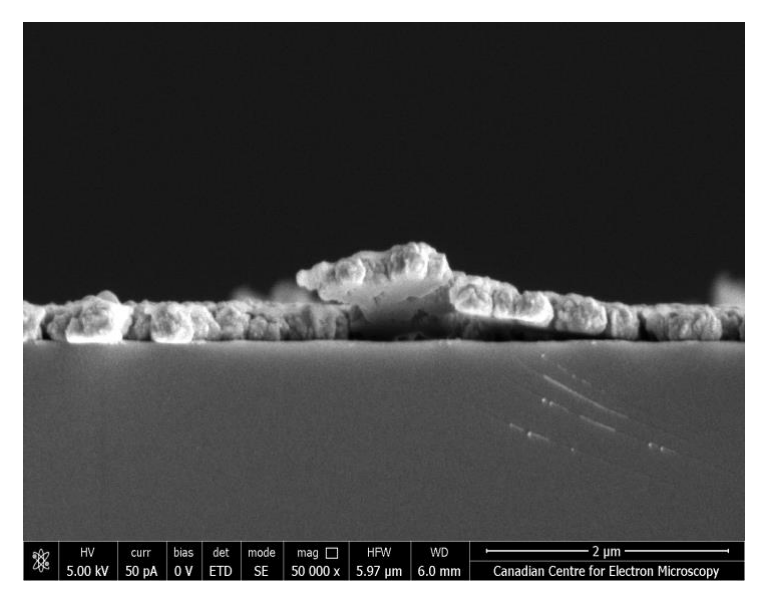


Figure 4.12. The cross-section SEM of sample Ni deposited on p-type Si (111) which was back-coated with 400 nm Al and 200 nm of Au, which demonstrated Ni peeled off Si's surface.

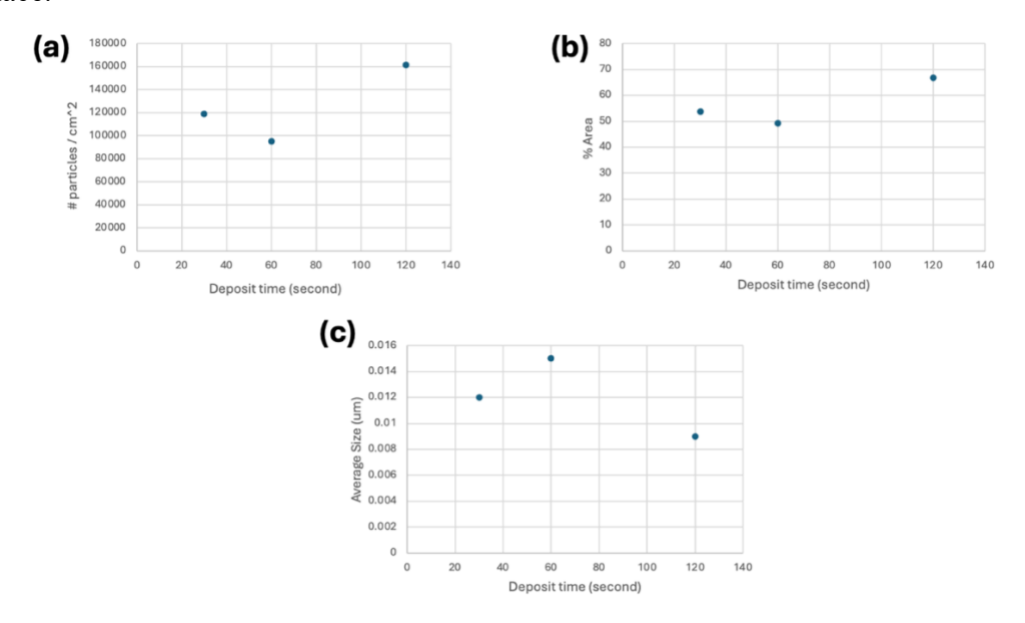


Figure 4.13. (a) Number of Ni particles per unit area in cm², (b) percentage of Ni particle covered the surface of p-type Si substrate (111), and (c) average size of Ni particles in μm.

Chapter 5 DC Electrodeposition on Nanowires

This chapter presents the Ni coating of GaAs and GaP NWs using the DC electrodeposition method. All NW depositions were performed using the design iteration 3 - custom Teflon cell. The study investigates deposition parameters that affect coating uniformity and structural integrity of the NWs. The challenges, such as bundling and bending of NWs and non-uniform coverage of Ni, are presented.

5.1 GaAs NWs

GaAs NWs were grown on GaAs (111) B substrates (As - terminated) following a multistep preparation and growth process. A 4.5 nm-thick gold film was deposited by electron-beam evaporation. The Au-coated substrates were transferred to a gas source molecular beam epitaxy (GS-MBE) system, where they were annealed at 600 °C under an As₂ flux for 5 minutes to form Au-Ga alloy nanoparticles and simultaneously remove the native oxide, assisted by a hydrogen electron cyclotron resonance plasma. NW growth was initiated by opening the Ga shutter at the desired substrate temperatures (500 °C-600 °C), maintaining a constant V/III flux ratio of 1.5. All growths were performed at a nominal two-dimensional rate of one monolayer per second (0.28 nm/s) for a duration of 30 minutes ²².

Figure 5.1 compares the GaAs NW array before (a) and after (b) Ni coating using the DC method at 0.9 mA for 1 minute. The "teepee" structures observed in Figure 5.1 (b) demonstrates the effects of the liquid electrolyte upon drying. This formation in NW arrays has been widely reported due to capillary forces during solvent evaporation. When liquid evaporates from between adjacent high-aspect-ratio NWs, surface tension pulls the wires together, often causing them to collapse and bundle at their tips. This phenomenon

has been observed in various nanomaterials such as carbon nanotubes, ⁵¹ Si NWs ⁵², and Ag NWs ⁵³. Elastocapillary coalescence occurs when fluid, which is trapped between supported plates or pillars, evaporates ⁵⁴. During the evaporation process, capillary forces pull the structures toward each other, leading to aggregation and clustering at the interface ⁵⁴. However, the extent of bundling depends strongly on NW geometry such as their length, pitch, diameter, as well as surface chemistry, and the evaporation dynamics of the solvent.

Figures 5.1 and Figure 5.2 present the tilted view and plan view, respectively, of the SEM and EDX mapping of Ga, As, and Ni. Although the presence of Ni was successfully confirmed in Figure 5.1 (e) and Figure 5.2 (e), the distortion of the NW array after deposition remained a significant challenge. Although the Ni coating seems relatively uniform along the GaAs NWs, their bending toward each other destroys the array.

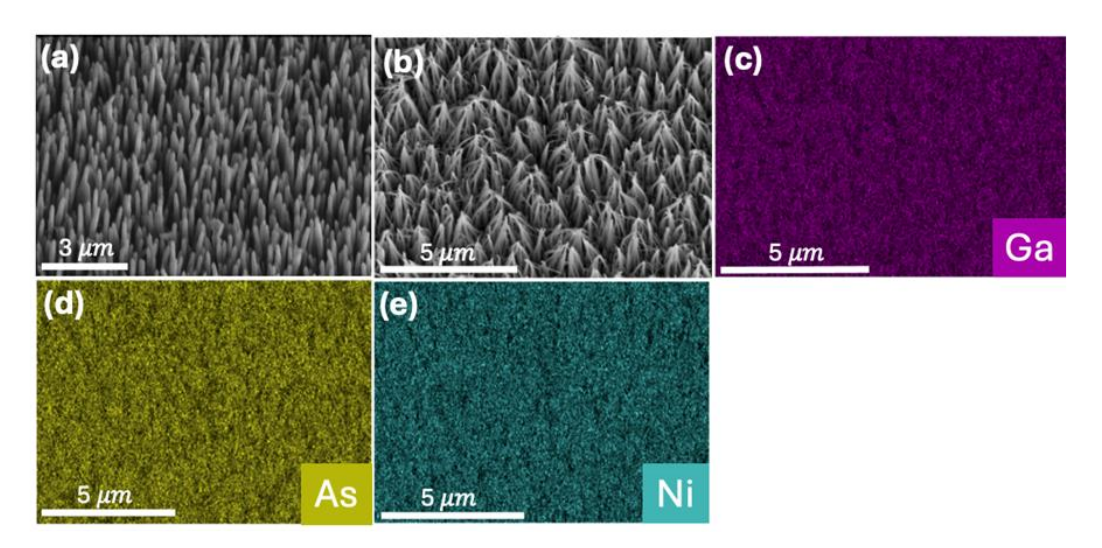


Figure 5.1. 30° tilted SEM and EDX analysis of Ni-coated GaAs NWs synthesized by DC electrodeposition. (a) SEM image of GaAs NWs on GaAs substrate before Ni deposition and (b) after Ni deposition, obtained using DC electrodeposition (0.9 mA, plating time = 1 minute). (c–e) EDX elemental maps showing distributions of Ga (purple), As (yellow), and Ni (blue), respectively.

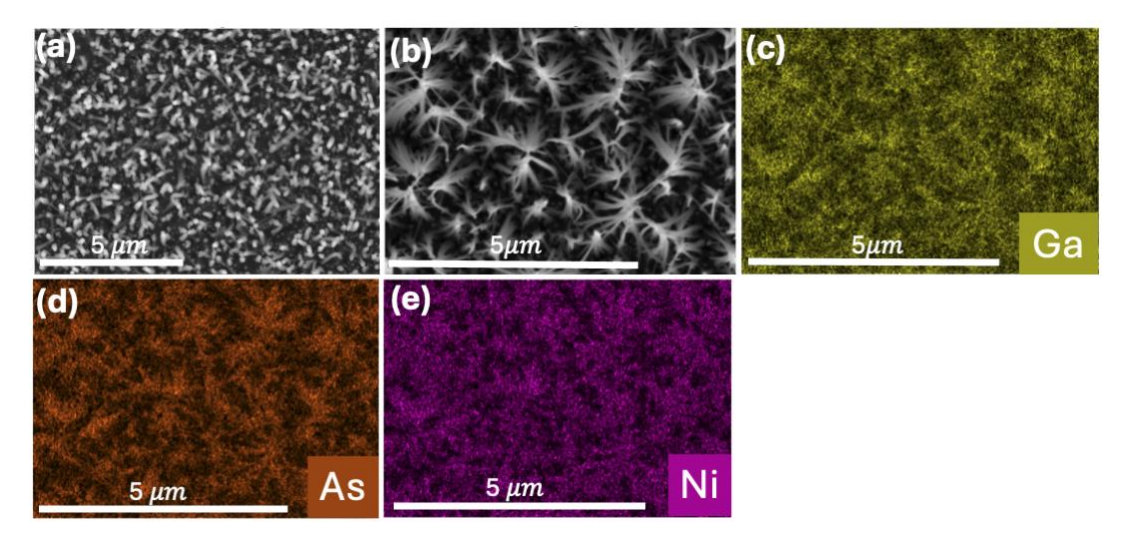


Figure 5.2. Plan view SEM and EDX analysis of Ni-coated GaAs NWs synthesized by DC electrodeposition. (a) SEM image of GaAs NWs on GaAs substrate before Ni deposition and (b) after Ni deposition, obtained using DC electrodeposition (0.9 mA, plating time = 1 minute). (c–e) EDX elemental maps showing distributions of Ga (yellow), As (brown), and Ni (purple), respectively.

5.2 GaP NWs

Be-doped GaP NWs were grown on p-type Si (111) substrates with the Be concentration of 1×10^{19} cm⁻³. The GaP NWs were grown by gas source molecular beam epitaxy using the self-assisted growth method (using Ga droplets) with an array of holes in an oxide mask. The separation between holes defined the NW separation (pitch) of 360, 600, or 1000 nm. Prior to NW growth, Ga droplets were pre-deposited in the holes of the oxide mask for 250 seconds at 650 °C with the deposition rate of 0.125 μ m/h. Be-doped NWs were then grown for 90 min by opening the P₂ flux with V/III ratio = 3. The temperature was maintained at 650 °C, and the deposition was stopped when Ga, P₂, and Be fluxes were all closed ³.

Figure 5.1 (a) shows an SEM image of the resulting NWs for 1000 nm pitch, grown by Thomas ³. Before deposition, the lengths of the GaP NWs with a 1000 nm pitch ranged from 2.6 μm to 3.8 μm, while some lying NWs reached up to 7.7 μm in length. The

diameters varied from 170 nm to 210 nm. The GaP NWs had a p-core structure surrounded by a GaP shell.

The same current magnitude as the GaAs NW sample (0.9 mA) was applied to the GaP NWs with a 1000 nm pitch, but with a longer deposition time of 45 minutes, as shown in the SEM image in Figure 5.2 (b). Figure 5.2 (c–f) presents the EDX spectra of Si, Ni, Ga, and As, respectively. After deposition, the NW length (Figure 5.3) increased to 9.33 μm, while the diameter reached approximately 1 μm. This increase in length and diameter indicates that Ni was successfully coated along the NWs, although only some were coated. Moreover, the coating was not uniform, as Ni clusters appeared along the NWs (Figure 5.3), and some NWs were not coated at all (Figure 5.3 (b)). Despite the partial success of Ni coating on the GaP NWs with 1000 nm pitch, the coating remained non-uniform under 0.9 mA for 45 minutes.

The Ni coating in Figure 5.3 was not continuous, but Kuzmin et al. reported that it is possible to form a continuous Ni layer if the deposition time increases or the electrolyte solution is more concentrated 20 . They reported a thickness of approximately 170 nm of Ni surrounding GaAs NWs with the length approximately 5 μ m (see Figure 5.4) and initial diameter of 64 nm. Hence, the deposition conditions were modified as described below.

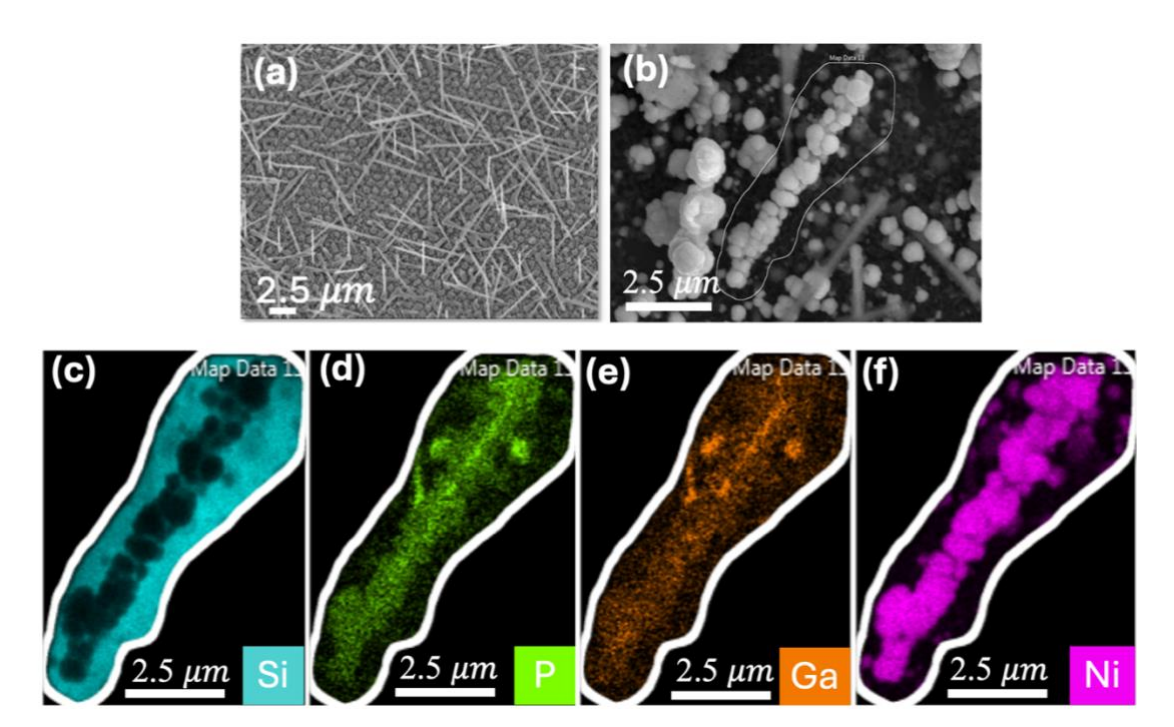


Figure 5.3. SEM and EDX analysis of Ni-coated GaP NWs (1000 nm pitch) by DC electrodeposition. (a) SEM image of GaP NWs before Ni deposition. (b) SEM image of GaP NWs after Ni deposition obtained using DC (0.9 mA, plating time = 45 minutes). (c–f) EDX elemental maps showing distributions of Si (blue), P (green), Ga (orange), and Ni (purple), respectively.

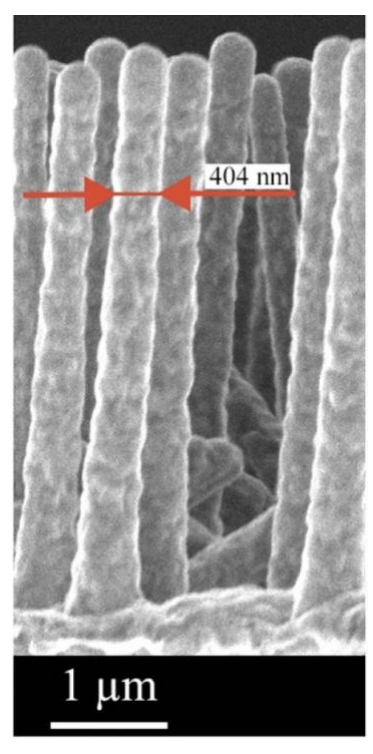


Figure 5.4. SEM image of GaAs NWs after Ni deposition using DC of 3.6 mA for 15 minutes. Reproduced from Ref ²⁰.

Figures 5.5, 5.6, and 5.7 show the results of Ni coating using the DC method on GaP NWs with pitch of 360 nm, 600 nm, and 1000 nm, respectively. All three samples were deposited under identical conditions: 3.6 mA for 15 minutes using the setup of iteration 3. Prior to plating, the samples were etched with BHF for 30 seconds, dried under N₂, and then immersed in a NiCl₂ and boric acid bath.

Figure 5.5 (a) shows the SEM of GaP NWs with 360 nm pitch before the deposition, and Figure 5.5 (b) is the SEM of the sample after electrodeposition. Only Si, Ga, and P signals were detected by EDX, and Ni was not detected. Two main issues were identified: (i) structural deformation of the NWs and (ii) absence of Ni. The bending and clustering of NWs likely resulted from capillary forces upon drying, as described earlier for GaAs NWs.

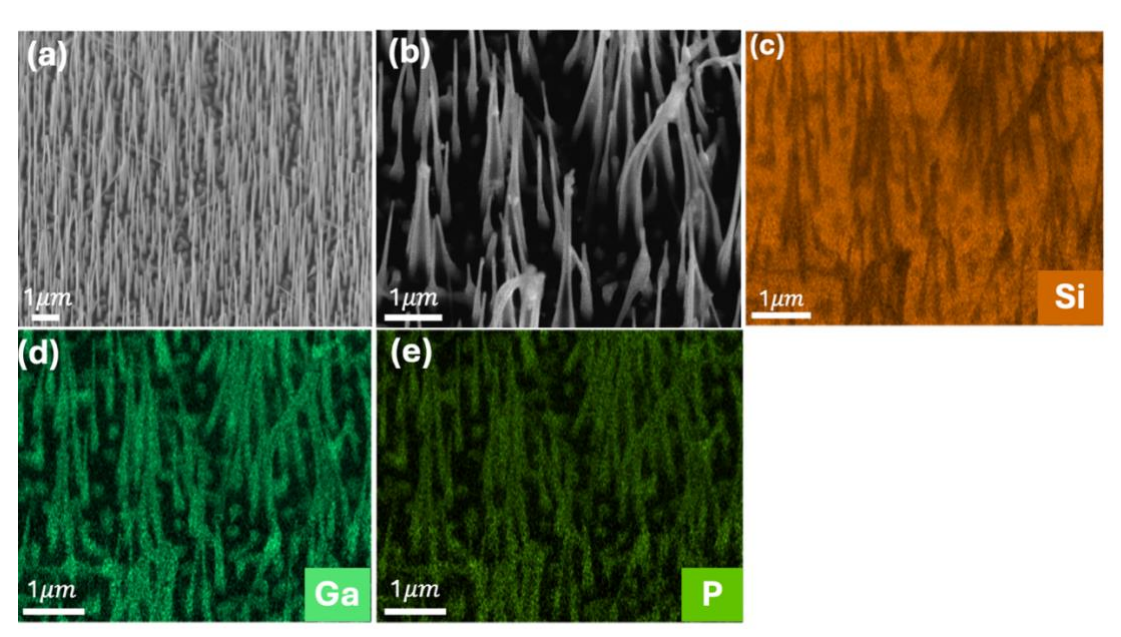


Figure 5.5. (a) SEM image of 360 nm pitch GaP NWs before Ni deposition. (b) SEM image of GaP NWs after Ni deposition at 3.6 mA for 15 minutes. (c–e) EDX elemental maps showing the distributions of Si (orange), Ga (jade green), and P (green), respectively. Ni was not detected.

Figure 5.6 shows the SEM images of GaP NWs with a 600 nm pitch (a) before deposition (30° tilted) and (b) after electrodeposition (57° tilted), together with the EDX maps of Ni (c) and Si (d). Figure 5.6 (c) indicates that Ni coating on GaP NWs with 600 nm pitch was successful under the conditions of 3.6 mA and 15 minutes. However, the Ga and P signals were not detected, and NWs were not observed. This concludes that NWs disappear under these conditions and were perhaps etched. This was later confirmed by focused ion beam on the 1000 nm pitch sample with similar surface morphology.

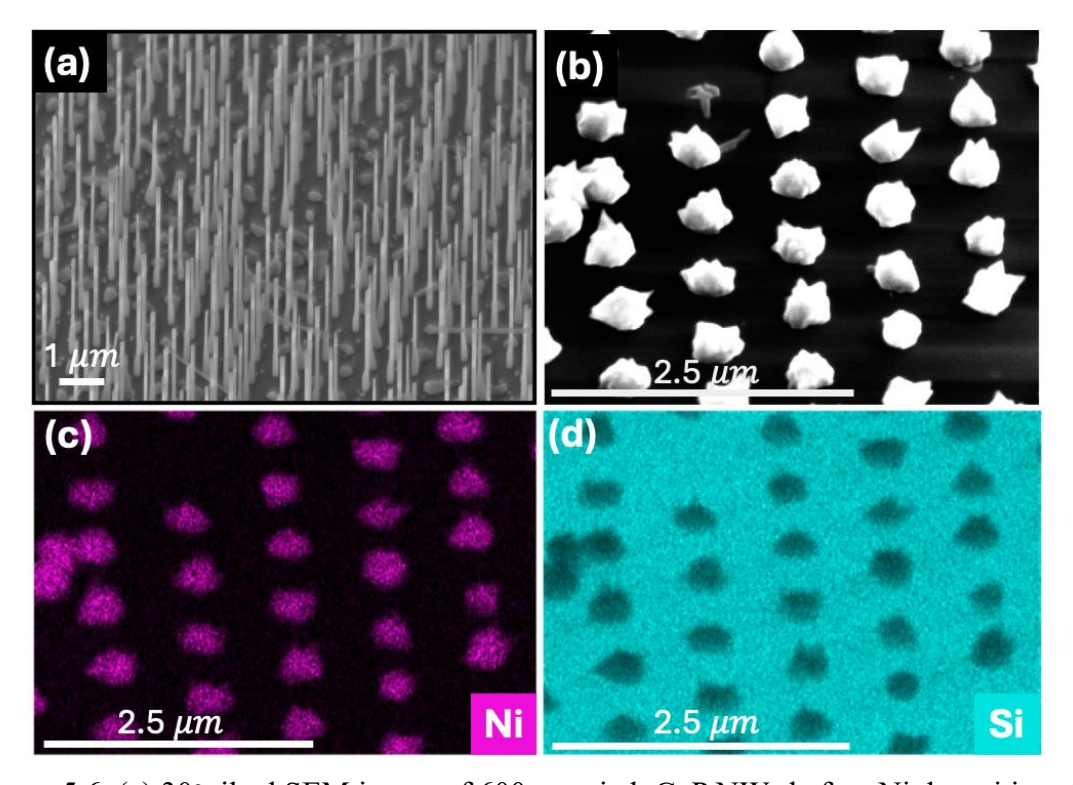


Figure 5.6. (a) 30° tilted SEM image of 600 nm pitch GaP NWs before Ni deposition. (b) 57° tilted SEM image of 600 nm pitch GaP NWs after Ni deposition at 3.6 mA for 15 minutes. (c–d) EDX elemental maps showing distributions of Ni (purple) and Si (blue), respectively.

Figure 5.7 (a) shows the SEM image of the 1000 nm pitch GaP NWs. SEM after electrodeposition (Figure 5.7 (b)) revealed a large Ni cluster coating the NWs and similar morphology as Figure 5.6. A gallium focused ion beam (FIB) was used to provide a cross-

sectional SEM image of the Ni-coated GaP NWs, as shown in Figure 5.8. The darker region above the sample was coated with carbon (C) to shield the surface from the Ga ion beam ⁵⁵. A subsequent layer of tungsten (W) was deposited to protect the carbon coating from sputtering and to facilitate a smoother surface finish ⁵⁵. As illustrated in Figure 5.6 and Figure 5.7, the NWs are no longer discernible; instead, the surface is covered with agglomerated Ni particles and a continuous metallic film.

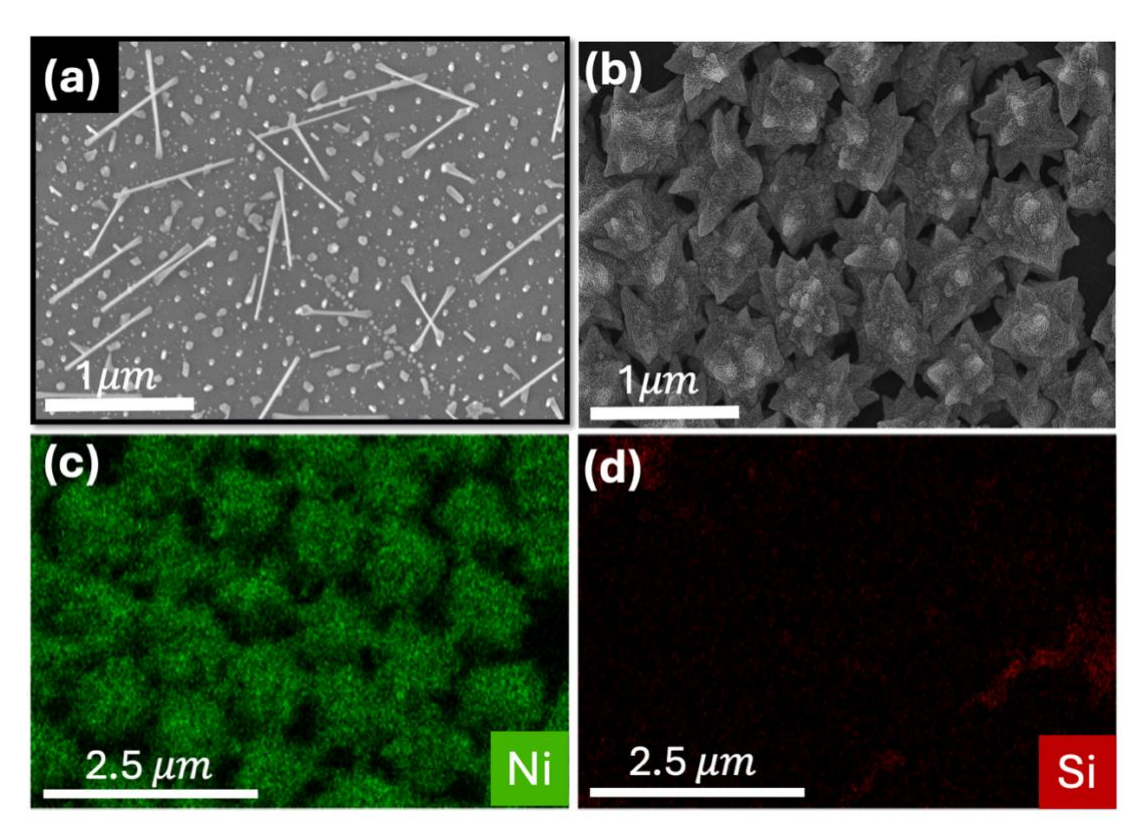


Figure 5.7. SEM images of 1000 nm pitch GaP NWs before Ni deposition. (b) SEM image of GaP NWs after Ni deposition at 3.6 mA for 15 minutes. (c–d) EDX elemental maps showing distributions of Ni (green) and Si (red), respectively.

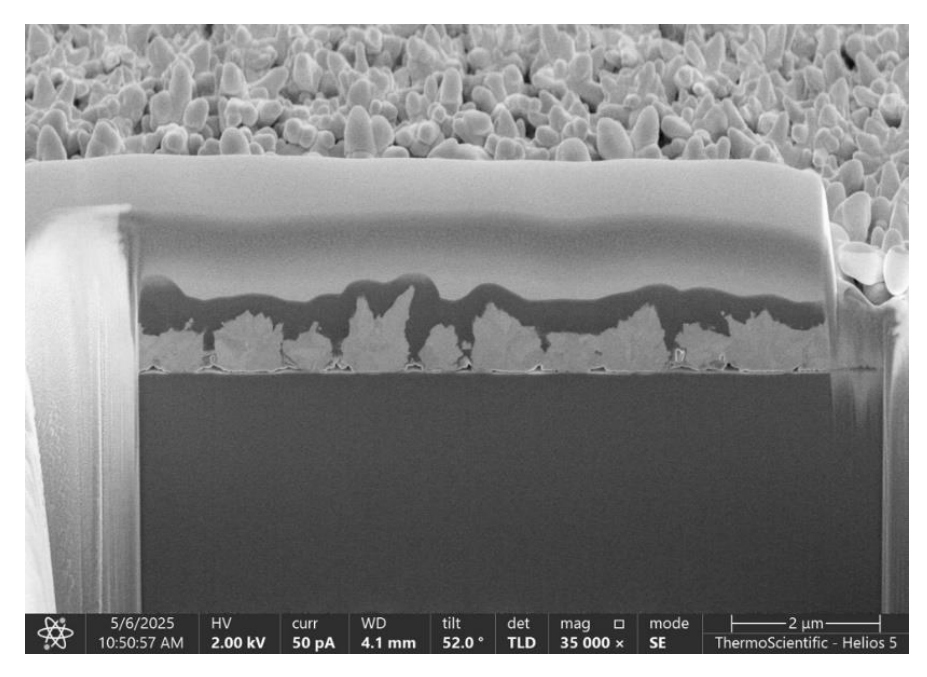


Figure 5.8. SEM image of 1000 nm pitch GaP NWs.

Both the 600 nm and 1000 nm pitch samples exhibited the same behavior under an applied current of 3.6 mA, where the NWs were etched during the electrochemical process. Instead of being plated, Ni²⁺ acted as a catalyst in a metal-assisted chemical etching (MACE)-like mechanism, leading to the etching of GaP.

COMSOL simulations (Figure 5.9) were performed showing that the electric field between NWs is screened at the smaller NW pitch (360 nm), while the electric field strength between the NWs increases as the spacing between NWs (pitch) increases. The current density, J is directly proportional to the electric field, E through material-dependent conductivity σ , according to Ohm's law:

$$J = \sigma E \tag{5.1}$$

Electrodeposition of Ni should theoretically be favored for the larger-pitch NWs, consistent with the simulation results (Figure 5.9). However, the enhanced local electric field also increases charge carrier injection and accelerates the MACE process, thereby

intensifying the etching of the GaP NWs. This behavior is evident in the experimental observations shown in Figures 5.5 - 5.7. These findings suggest that, under the applied conditions, Ni²⁺ ions play a dual role - acting both as a deposition source and as a catalyst that promotes the dissolution of GaP NWs through a MACE-like mechanism.

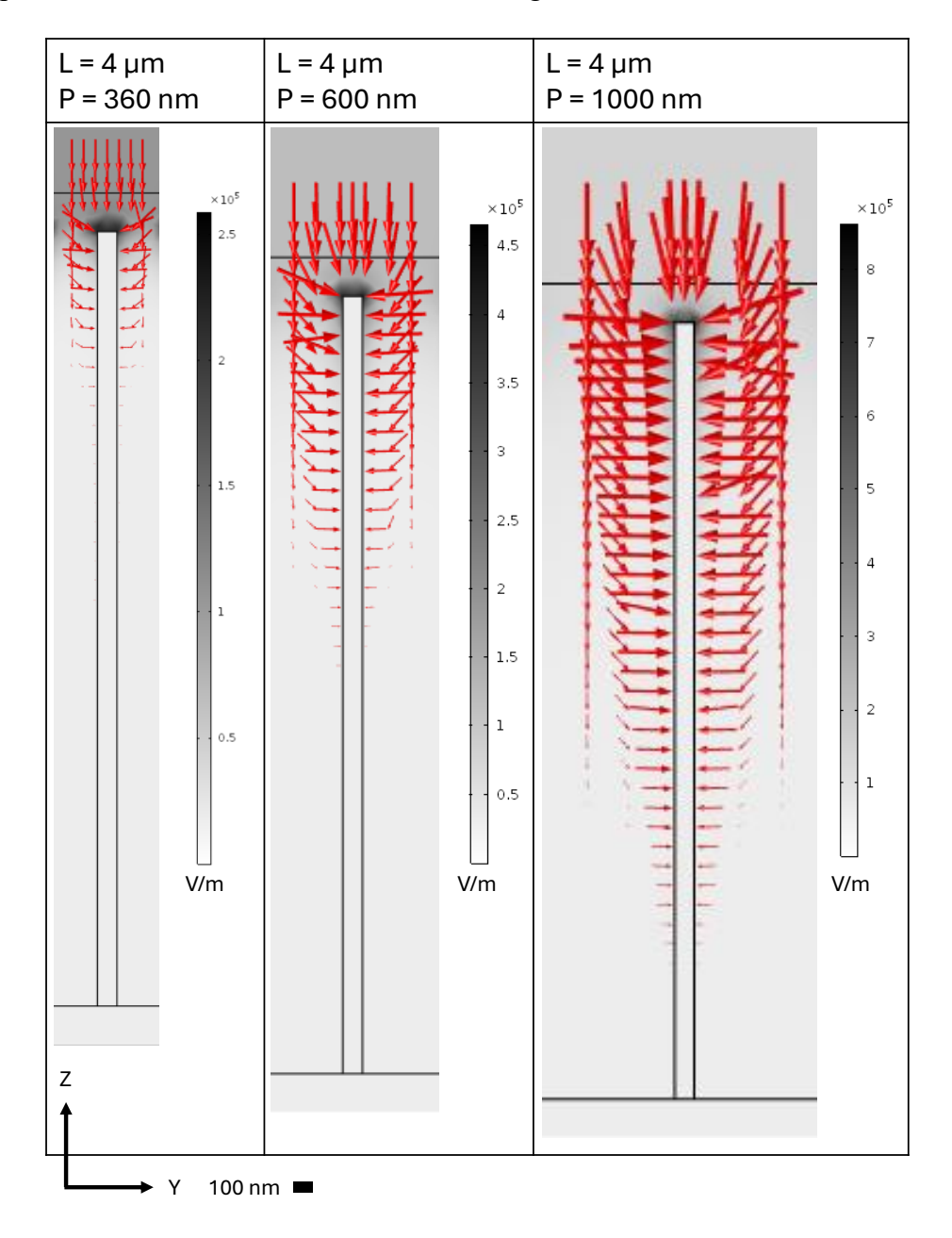


Figure 5.9. Electric field strength and field vectors for 360, 600 and 1000 nm pitch NWs with length $L=4~\mu m$.

This chapter demonstrated Ni electrodeposition on GaAs and GaP NWs using a custom Teflon cell and DC current. For GaAs NWs, short deposition times (0.9 mA, 1 min) achieved Ni coating while preserving array geometry, though bundling and bending occurred due to capillary forces. For GaP NWs, longer deposition or higher current (3.6 mA, 15–45 min) led to non-uniform coatings, Ni clustering, or complete NW dissolution, particularly for wider-pitch arrays. COMSOL simulations confirmed that higher local electric fields in larger pitch NWs resulted in greater Ni deposition but also NW etching. These results highlight the critical influence of NW geometry, current density, and material on deposition outcomes, emphasizing the need for careful optimization to achieve uniform, conformal Ni coatings on high-aspect-ratio NW arrays.

Chapter 6 Pulse Electrodeposition on Nanowires

In this chapter, we discuss the results of electroplating Ni on GaAs and GaP NWs using pulse signals, as well as the dependence of the coating results on the applied voltage and the NW pitch.

6.1 The Mechanism of Pulse Electrodeposition

The mechanism of PED is divided into two types of transport of the Ni ions, namely axial transport (from top to bottom of a NW) and replenishment of Ni between NWs. Axial transport includes drift and diffusion. During the pulse, t_{on} , the voltage causes Ni²⁺ in bulk solution to drift in solution from the top to the bottom of the NW, leading to the deposition. The drift velocity v is expressed as:

$$v = \mu E \tag{6.1}$$

where E is the electric field and μ is the Ni²⁺ mobility. μ can also be expressed through the Einstein relation as:

$$\mu = \frac{Dq}{k_B T} \tag{6.2}$$

where D is the diffusion coefficient (m²s⁻¹), q is the electric charge of the Ni ion (C, Coulombs), k_B is the Boltzmann constant (JK⁻¹), and T is temperature of the bath solution (K, Kelvin). The electric field E is written in terms of voltage V across the NW length L:

$$E = \frac{V}{L} \tag{6.3}$$

The time for Ni²⁺ to drift from the top to the bottom of a NW is:

$$t_{drift} = \frac{L}{v} \tag{6.4}$$

M.A.Sc Thesis - L. Lam; McMaster University – Engineering Physics

Combining these equations, the drift time of Ni ions is:

$$t_{drift} = \frac{L}{\mu E} = \frac{L}{\frac{Dq \ V}{k_B T L}} = \frac{L^2}{D} \frac{k_B T}{q V}$$

$$\tag{6.5}$$

Substituting $q = 1.602 \times 10^{-19}$ C, $k_B = 1.380649 \times 10^{-23}$ J/K, and T = 298 K, gives:

$$t_{drift} = \frac{L^2}{D} \frac{1.380649 \times 10^{-23} \times 298}{1.602 \times 10^{-19} \times V} \approx \frac{L^2}{D} \frac{0.02568}{V}$$
 (6.6)

During t_{off} , diffusion happens so Ni²⁺ ions can diffuse from bulk solution to the bottom of the NW to replenish Ni lost be deposition. Applying the diffusion equation, we have:

$$t_{diffusion} = \frac{L^2}{D} \tag{6.7}$$

Substitute $D = 6.79 \times 10^{-10}$ m²s⁻¹ for Ni^{2+ 56}, and length of GaP NWs L = 3.8 µm, the diffusion time is:

$$t_{diffusion} = \frac{(3.8 \times 10^{-6})^2}{6.79 \times 10^{-10}} \approx 2.127 \times 10^{-2} s = 21.3 \text{ ms}$$

The drift time is rewritten as:

$$t_{drift} = 21.3 \, ms \, \times \frac{0.02568}{V} \tag{6.8}$$

The drift time is inversely proportional to the voltage as shown in Figure 6.3. As voltage increases, the drift velocity increases, so ions travel faster along the NW channel, and the drift time decreases. At low voltage, t_{drift} becomes large, meaning ions take longer to reach the bottom of the NW, possibly leading to incomplete or non-uniform deposition. At high voltage, t_{drift} decreases, meaning ions arrive too quickly, which may cause non-uniform growth, agglomeration, or rough morphology. Thus, the voltage needs to be in a certain range.

The appropriate voltage can be estimated as follows. The plating bath consisted of 5.625 g of NiCl₂.6H₂O and 0.75 g of boric acid in the volume V of 35 mL, so the concentration of Ni²⁺ and boric acid are, respectively:

$$[Ni^{2+}] = [NiCl_2.6H_2O] = \frac{5.625 g}{\frac{(58.69 + 2 \times 35.5 + 12.096 + 6 \times 16)g}{mol} \times 0.035L} = 0.676 \text{ mol/L}$$
(6.9)

$$[H_3BO_3] = \frac{0.75 g}{(3+11+3\times16)g/mol\times0.035L} = 0.351 \text{ mol/L}$$
(6.10)

Recall Equation (2.6) and the reaction quotient, Q, used in a non-equilibrium reaction from Chapter 2. The reaction is:

$$Ni_{(aq)}^{2+} + 2H_2O_{(l)} \rightarrow Ni_{(s)} + O_{2(q)}^{\uparrow} + 4H_{(aq)}^{+}$$

Given $[Ni^{2+}] = 0.676$ M and pH = $4.62 \Rightarrow [H^+] = 10^{-4.62}$ M, and assuming $\rho_{O_2} = 1$ atm, Q is computed as the ratio of the initial activities of all products (a), each raised to the power of their stoichiometric coefficients, to the initial activities of all reactants, each raised to their respective stoichiometric coefficients. Assuming the solid Ni and water are pure, so their activities are both 1, we get:

$$Q = \frac{\left(a_{H^+}\right)^4 \left(a_{O_2}\right) (a_{Ni})}{\left(a_{Ni^2+}\right) \left(a_{H_2} O\right)^2} = \frac{\left(\frac{[H^+]}{1\,M}\right)^4 \left(\frac{\rho_{O_2}}{1\,atm}\right) (1)}{\left(\frac{[Ni^{2+}]}{1\,M}\right) (1)^2} = \frac{\left(\frac{10^{-4.62}M}{1\,M}\right)^4 \times \left(\frac{1atm}{1atm}\right)}{\left(\frac{0.676}{1M}\right)} \approx 4.898 \times 10^{-19} \tag{6.11}$$

or $lnQ \approx -42.16$

Recalling the Nernst equation, Eq. (2.15), from Chapter 2 that $E_{cell} = E_{cell}^0 - \left(\frac{RT}{nF}\right) lnQ$, and E_{cell}^0 was previously determined to be -1.49 V, we get:

$$E_{cell} = E_{cell}^{0} - \left(\frac{8.314 \times 298.15}{4 \times 96487}\right) \times (-42.16) = -1.49 - (-0.271) \approx -1.22 \,V \tag{6.12}$$

Therefore, the minimum cell voltage at experimental conditions is approximately 1.22 V vs SHE. In practice, due to kinetic overpotentials and IR drops, the working cell voltage

needs to be greater than this minimum cell voltage. Consequently, the range of voltage 2.0 V - 3.0 V is appropriate depending on deposition rate and coating morphology.

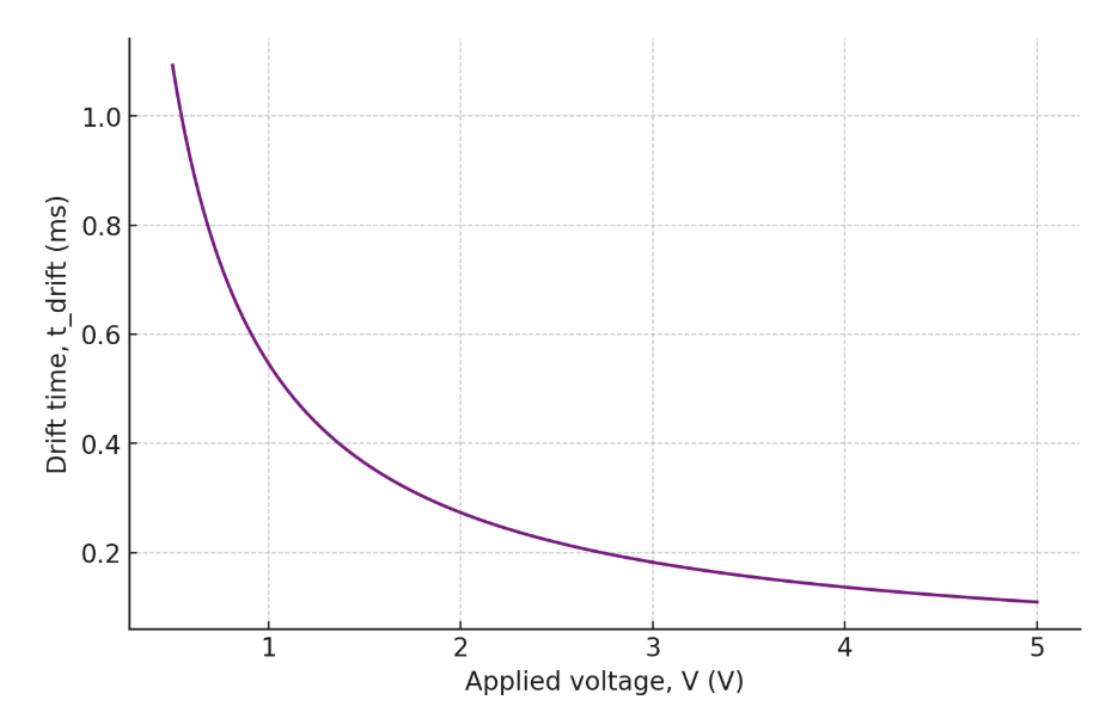


Figure 6.1. Drift time (t_{drift}) of Ni²⁺ ions versus applied voltage for GaP NWs.

Using a voltage of 3 V, we get:

$$t_{drift} = 21.3 \text{ ms } \times \frac{0.02568}{3.0} \approx 0.182 \text{ ms}$$
 (6.13)

We choose t_{on} and t_{off} based on the value of drift time and diffusion time, respectively. Ideally, t_{on} is required to be equal or greater than the drift time, which is 0.182 ms, and t_{off} needs to be at least 21.3 ms.

6.2 GaAs NWs

The output signal from Figure 2.3 was applied to the anode of the electrochemical cell while the cathode was grounded (see Figure 3.8). For GaAs NWs, the chosen t_{on} is 10 ms $\gg t_{drift}$ (0.182 ms) and t_{off} is 1s $\gg t_{diffusion}$ (21.3 ms), respectively. SEM and

EDX results in Figures 6.4, Figure 6.5, and Figure 6.6 chronicle how a Ni coating develops on GaAs NWs over 15 minutes, 30 minutes, and 90 minutes of plating. At 15 minutes (Figure 6.3), SEM reveals a dense array of some vertically aligned NWs (2–5 µm in height) having Ni wrapped at their bases; EDS mapping confirms Ni concentrated at the root of NWs.

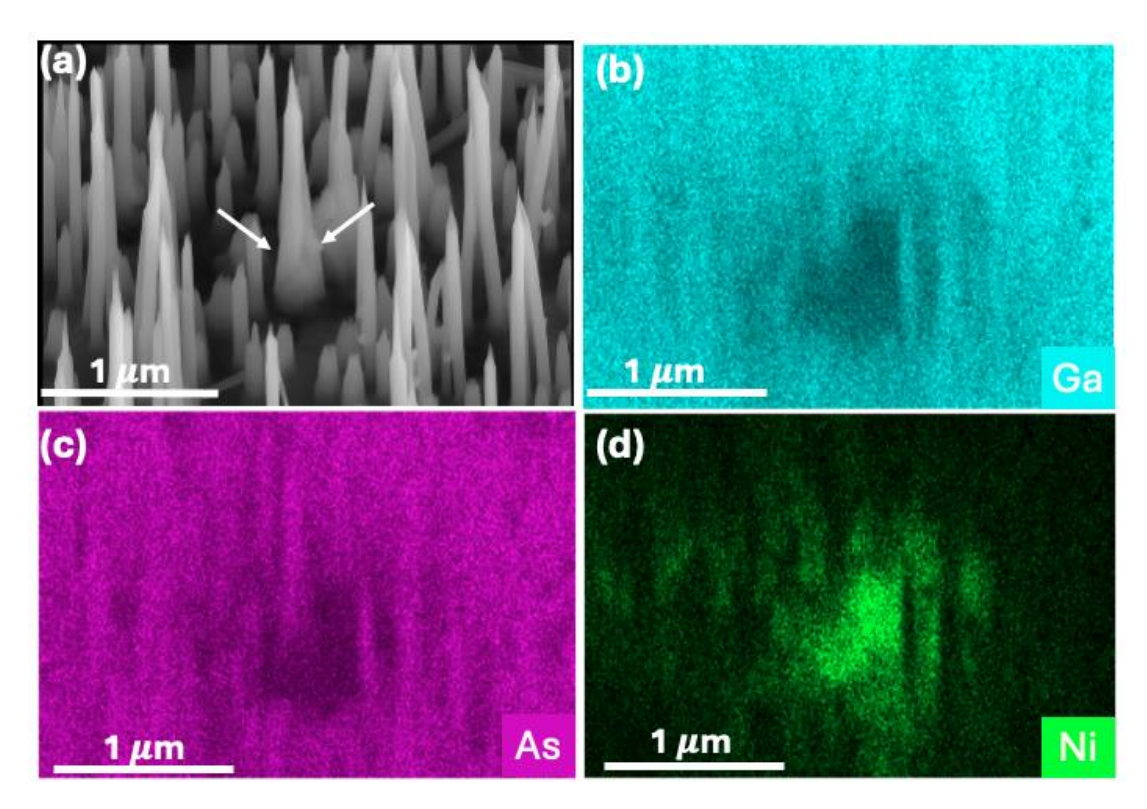


Figure 6.2. (a) SEM image of Ni-coated GaAs NWs obtained using pulse signal parameters ($t_{on} = 10 \text{ ms}$, $t_{off} = 1 \text{ s}$, plating time = 15 min) with the arrows indicating the location of Ni deposition. (b–d) EDX elemental maps showing distributions of Ga (blue), As (purple), and Ni (green), respectively.

By 30 minutes (Figure 6.4), some Ni appears to have coated the NWs. An EDX line-scan across some bundled NWs (Figure 6.5) shows a weak Ni signal. Although the Ni coating appears relatively uniform, the Ni content at the top of the NWs is slightly higher than along the rest of their length. This preferential accumulation at the top likely hinders the transport of Ni²⁺ ions toward the bottom regions of the NWs. Consequently, achieving

precise control over the coating thickness and ensuring uniform deposition along the entire length of the NWs becomes more difficult.

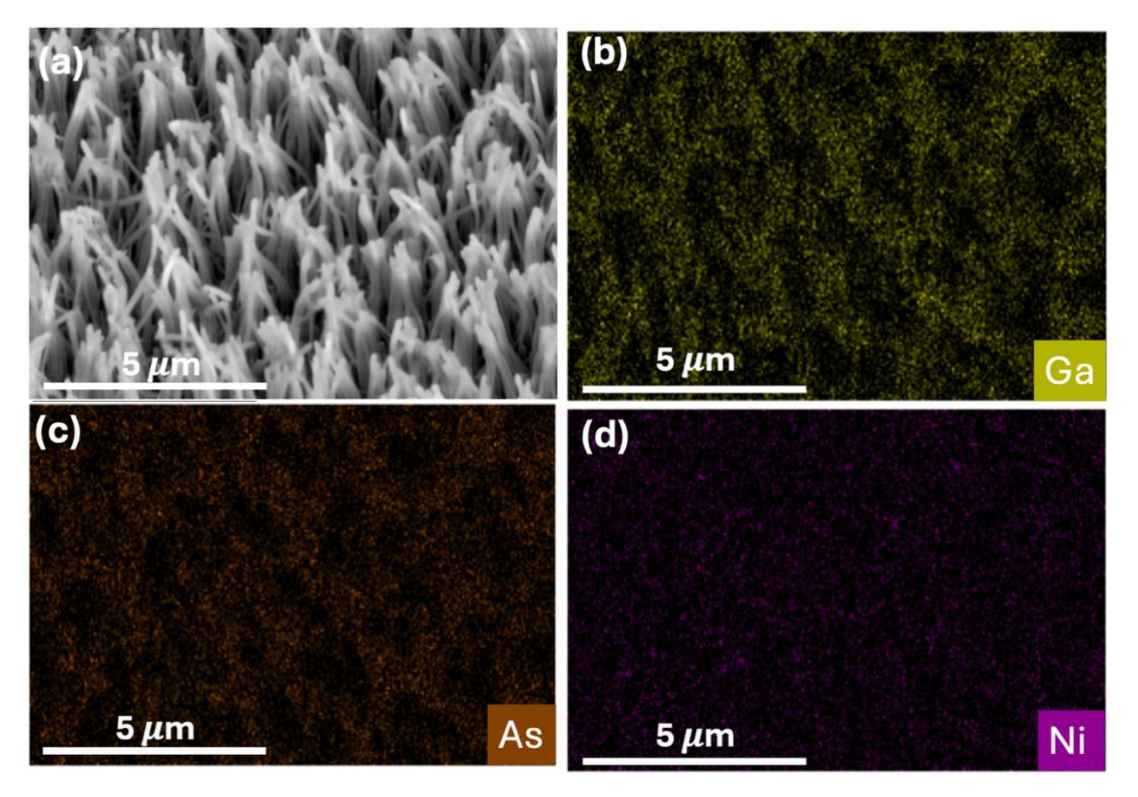


Figure 6.3. (a) SEM image of Ni-coated GaAs NWs obtained using pulse signal parameters ($t_{on} = 10 \text{ ms}$, $t_{off} = 1 \text{ s}$, plating time = 30 min). (b–d) EDX elemental maps showing distributions of Ga (yellow), As (brown), and Ni (purple), respectively.

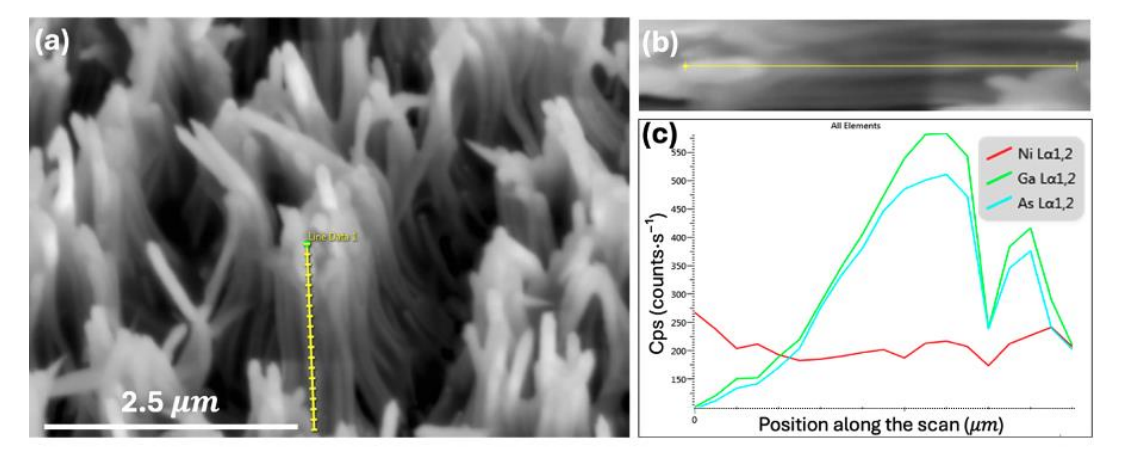


Figure 6.4. GaAs NWs from Figure 6.4. (a) SEM image of GaAs NWs with a height marker of 2 µm. (b) SEM image of a single NW, with a yellow line indicating the region analyzed by EDX. (c) Elemental intensity profiles along the line in (b), showing the distributions of Ni (red), Ga (green), and As (blue).

At 90 minutes (Figure 6.6), Ni is clear on the NWs. EDX now displays an almost uninterrupted Ni coverage, with Ga and As detectable only in isolated cracks. However, it appears that Ni was coated preferentially at the top of the NWs. This could be explained by a "mass diffusion limit" mechanism⁵⁷. When the pulse on-time is extended, Ni²⁺ depletion near the NW surfaces becomes significant. Due to restricted diffusion inside the NW array, Ni²⁺ ions at the bottom of the wire are replenished more slowly compared to the array top, leading to preferential deposition at the tips. This results in a blocking layer that hinders ion transport into the gaps, preventing uniform Ni filling. Shorter on-times combined with sufficiently long off-times are therefore necessary to mitigate mass-diffusion limitations and enable deposition along the entire NW sidewalls.

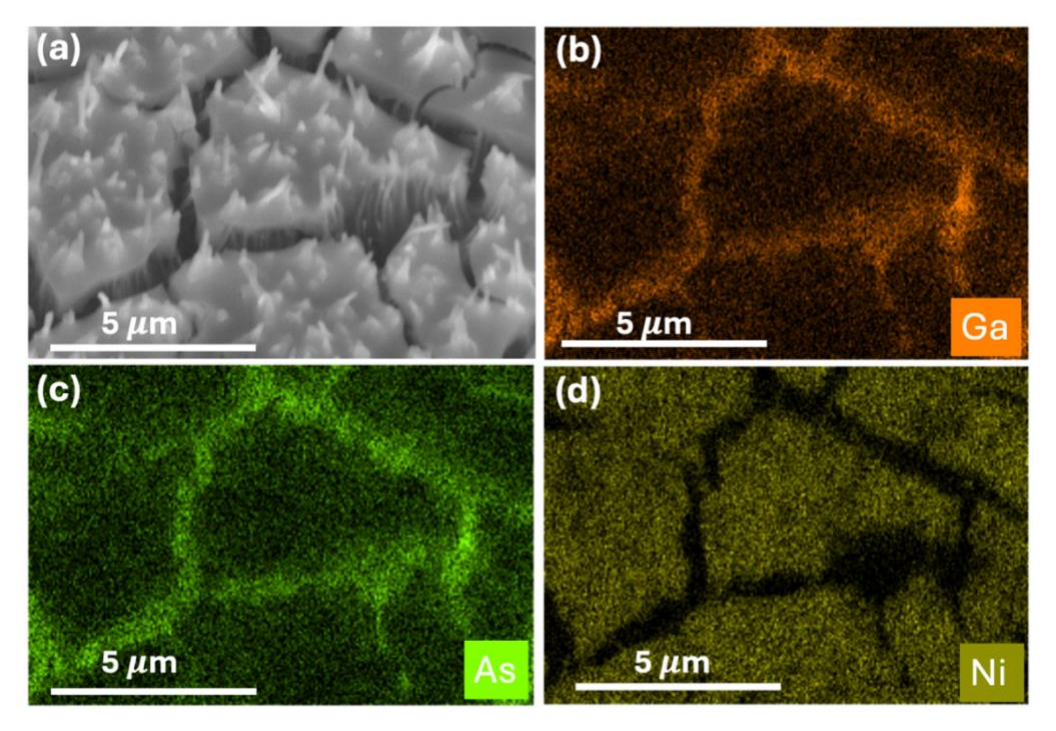


Figure 6.5. (a) SEM image of Ni-coated GaAs NWs obtained using pulse signal parameters ($t_{on} = 10 \text{ ms}$, $t_{off} = 1 \text{ s}$, plating time = 90 min). (b-d) EDX elemental maps showing distributions of Ga (orange), As (green), and Ni (yellow), respectively.

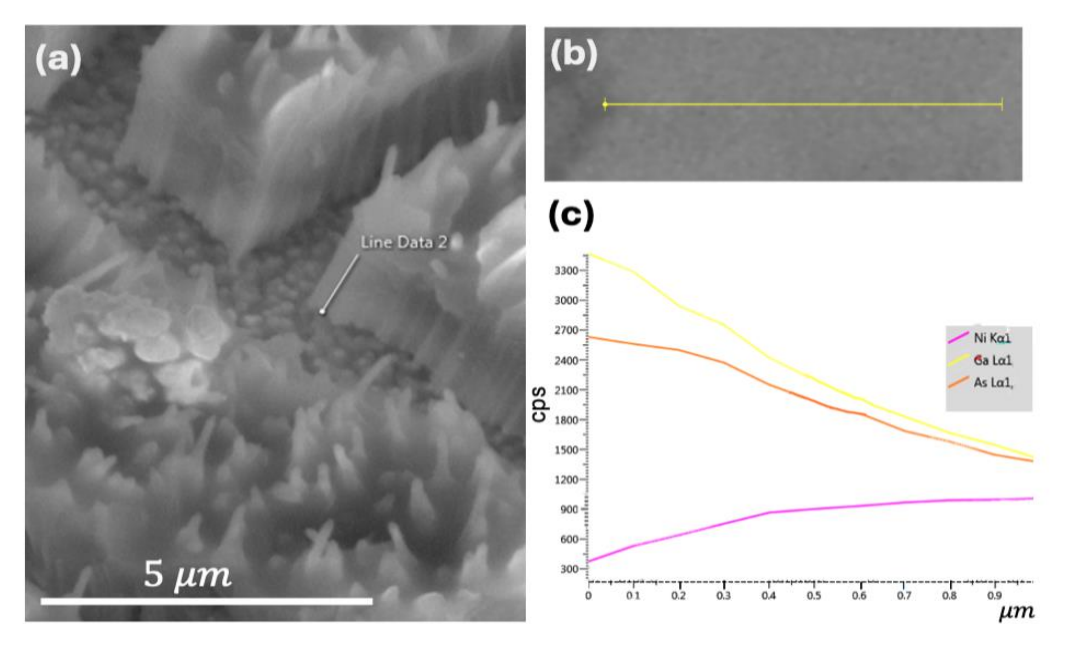


Figure 6.6. Correlative structural and elemental analysis of the surface structure of GaAs NWs from Figure 6.6. (a) SEM image of GaAs NWs with a height marker of 2 μ m. (b) SEM image of a single NW, with a yellow line indicating the region analyzed by EDX. (c) Elemental intensity profiles along the line in (b), showing the distributions of Ni (purple), Ga (yellow), and As (orange).

The observations from Figures 6.4, 6.5, 6.6, and 6.7 mapped a clear transition from early-stage axial nucleation to prolonged lateral growth and film densification as plating time increases. However, the chosen 10 ms on/1 s off are not the best parameters as the coating is not uniform along individual GaAs NWs. The on-time is too long $(t_{on} >> t_{drift})$ and leads to a nonuniform coating, as observed in Figure 6.7.

6.3 GaP NWs

Figures 6.8, 6.10, and 6.13 present the results of GaP NWs with pitches of 360, 600, and 1000 nm, respectively, after pulse plating Ni with $t_{on} = 10$ ms and $t_{off} = 1$ s for 15 minutes at 3 V. Under identical conditions, different pitches produced distinct outcomes. Among the three, uniform Ni coating was observed only for the 1000 nm pitch, whereas no Ni was detected for the 360 nm and 600 nm samples (see Figures 6.9 and 6.11 for

closer inspection). In these two cases, NW bundling was also observed. Combined with the EDX spectra, this indicates that no Ni was deposited between the bundled NWs of the 360 nm and 600 nm samples. The most plausible explanation is that a pitch of 1000 nm provides sufficient spacing to prevent NWs from merging, thereby reducing the likelihood of bundling. This interpretation is supported by SEM analysis: NW arrays with a pitch of 360 nm exhibit more pronounced joining compared to those with a 600 nm pitch (Figures 6.8 and 6.10, respectively).

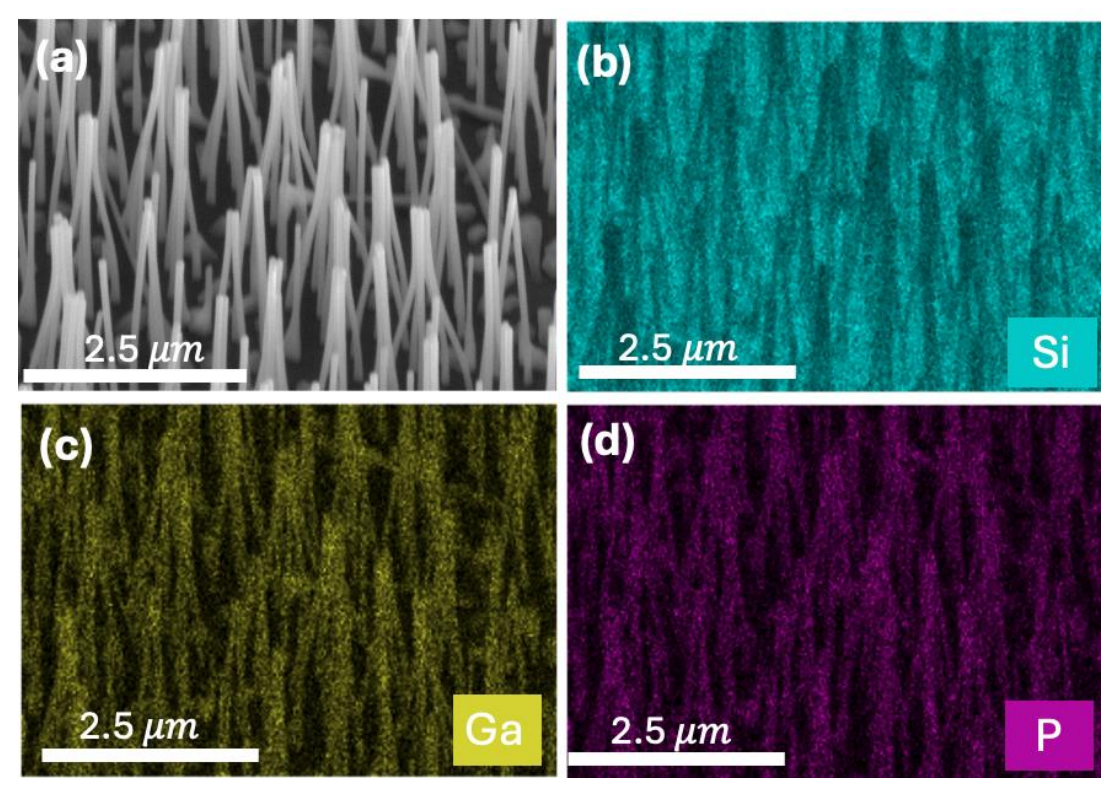


Figure 6.7. (a) SEM image of 360 nm pitch GaP NWs after Ni deposition using $t_{on} = 10$ ms, $t_{off} = 1$ s, V = 3 V, and plating for 15 min. (b-d) EDX elemental maps showing distributions of Si (blue), Ga (yellow), and P (purple), respectively. Ni was not detected.

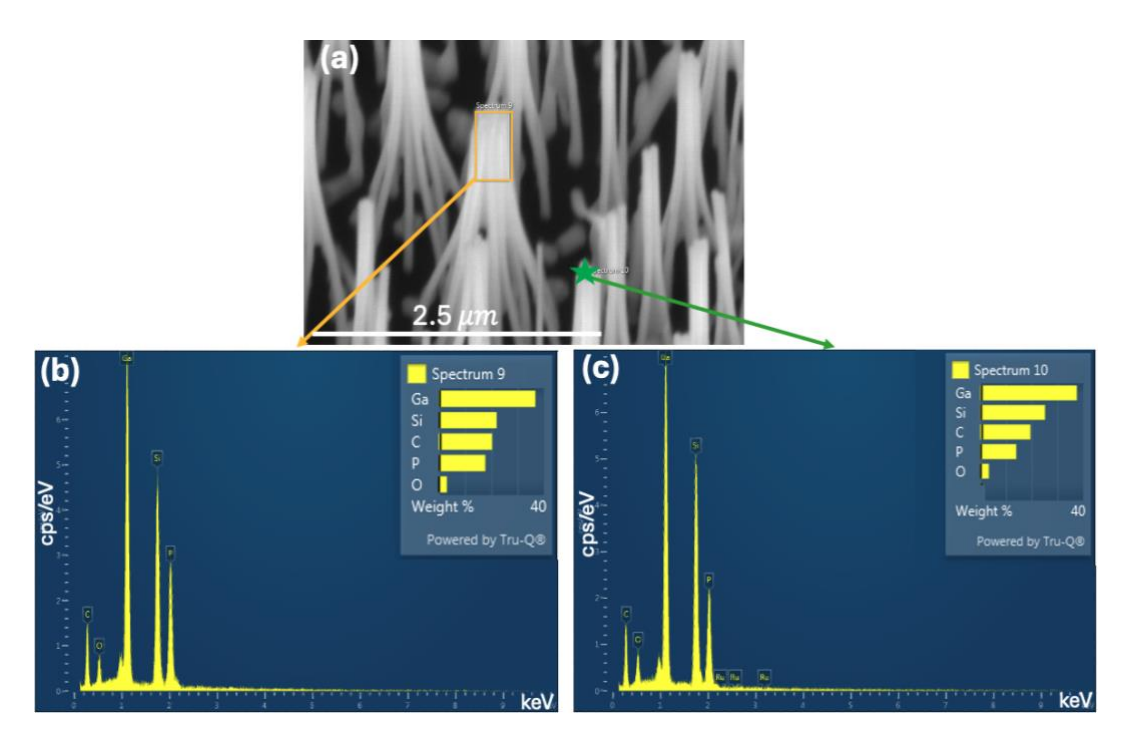


Figure 6.8. (a) SEM image of GaP NWs with a 360 nm pitch after Ni deposition. (b–c) EDX spectra obtained from the selected regions in (a). The orange rectangle and the green star indicate the specific areas analyzed by EDX.

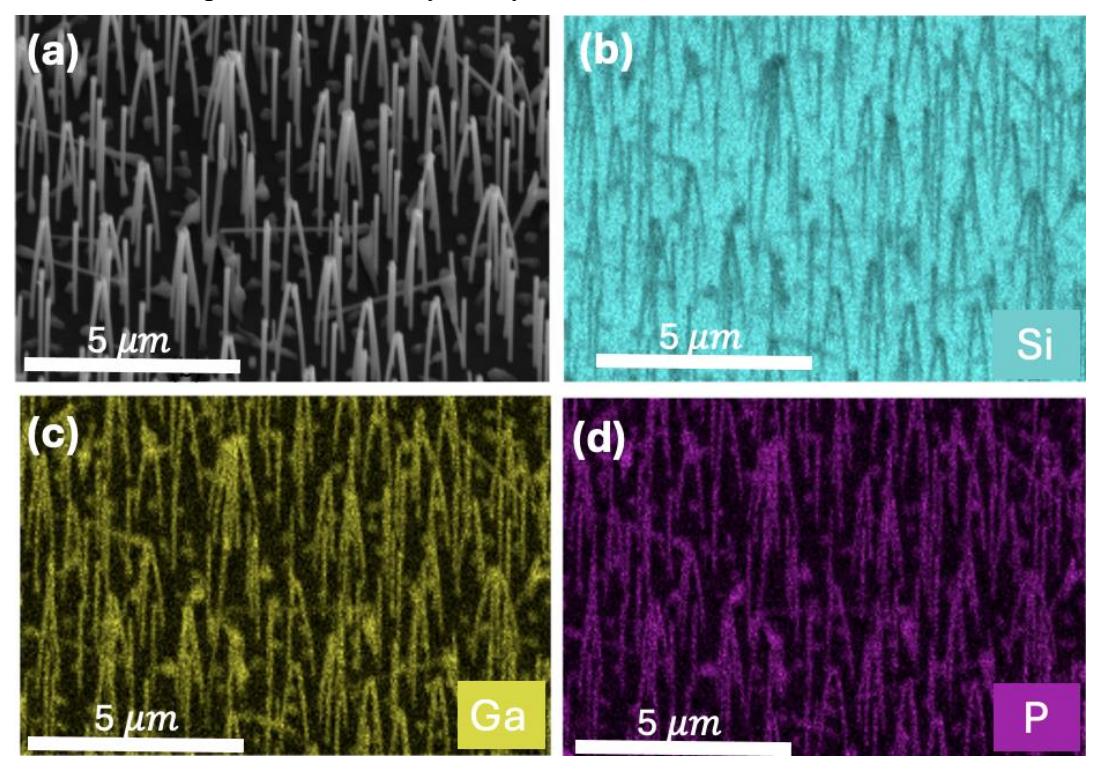


Figure 6.9. (a) SEM image of 600 nm pitch GaP NWs after Ni deposition using $t_{on} = 10$ ms, $t_{off} = 1$ s, V = 3 V, and plating for 15 min. (b–d) EDX elemental maps showing distributions of Si (blue), Ga (yellow), and P (purple), respectively.

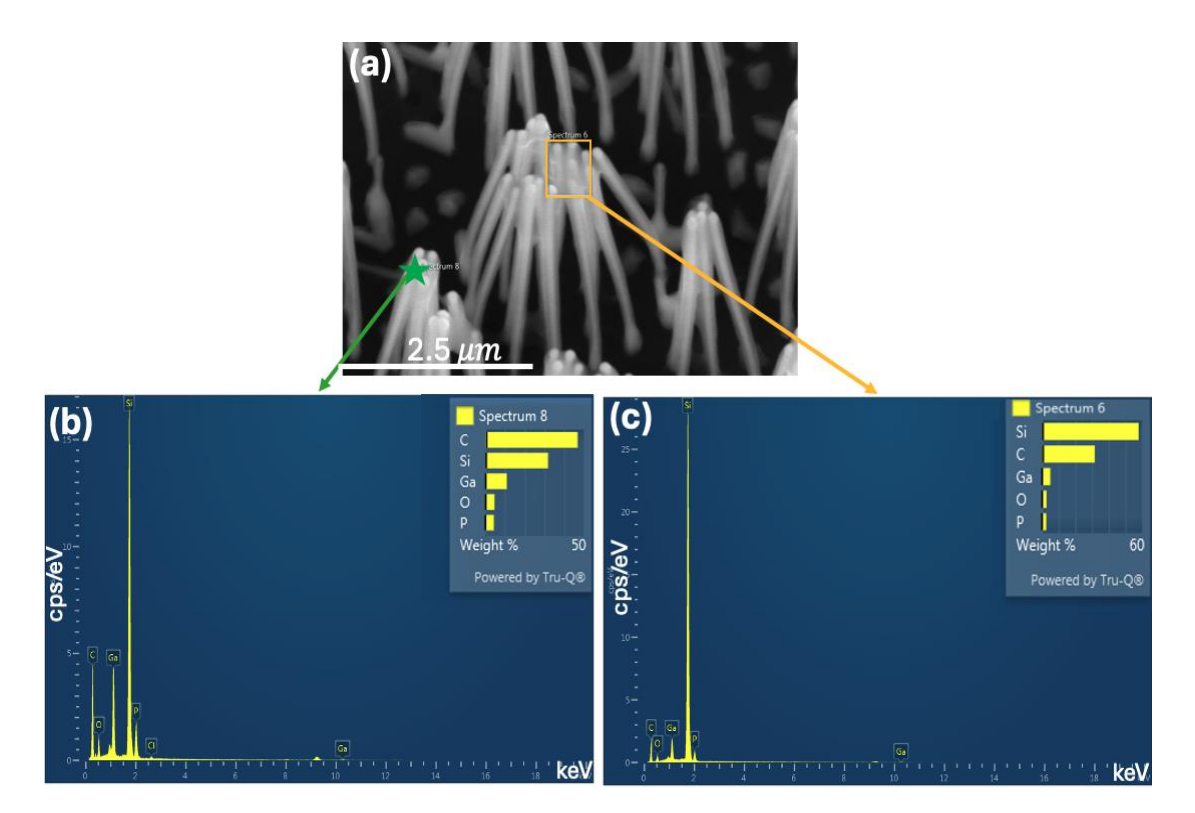


Figure 6.10. (a) SEM image of GaP NWs with a 600 nm pitch after Ni deposition. (b–c) EDX spectra obtained from the selected regions in (a). The orange rectangle and the green star indicate the specific areas analyzed by EDX.

Figure 6.12 (same as Figure 5.9) may explain why there was not any Ni in 360 nm and 600 nm pitch samples and uniform Ni coating along 1000 nm pitch sample (Figure 6.13). The electric field between NWs increase as NWs array are sparser. Greater electric field supports the greater transport of Ni²⁺ ions down to the bottom of each NW during electrodeposition. Moreover, the NWs in 1000 nm pitch are the furthest apart among three samples, so they are less likely to bend and touch than 360 nm and 600 nm NWs samples.

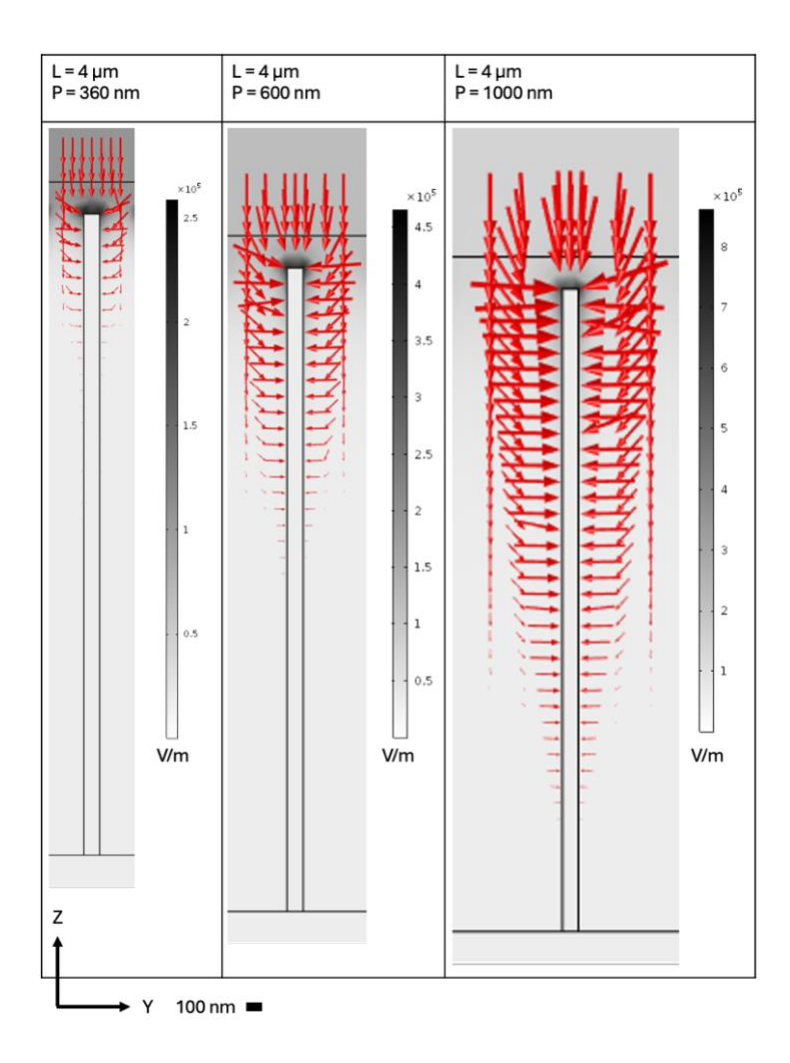


Figure 6.11. The electric field components along the y- and z-axes (E_y and E_z) around NW structure. The legend is presented on a logarithmic scale by a factor of 1×10^{-12} to set the base reference level for the smallest arrow lengths. A range quotient of 10^3 indicates that the longest arrows are about 1000 times longer than the shortest one. The greyscale represents the norm of the Y- and Z- components.

Based on the SEM and EDX results (Figures 6.13 and 6.14), Ni coating along the NWs was successfully achieved on 1000 nm pitch. According to Figure 6.14, the Ni signal in the spectrum was 56.5% by weight, which is the highest among the main elements Ga, P, and Si.

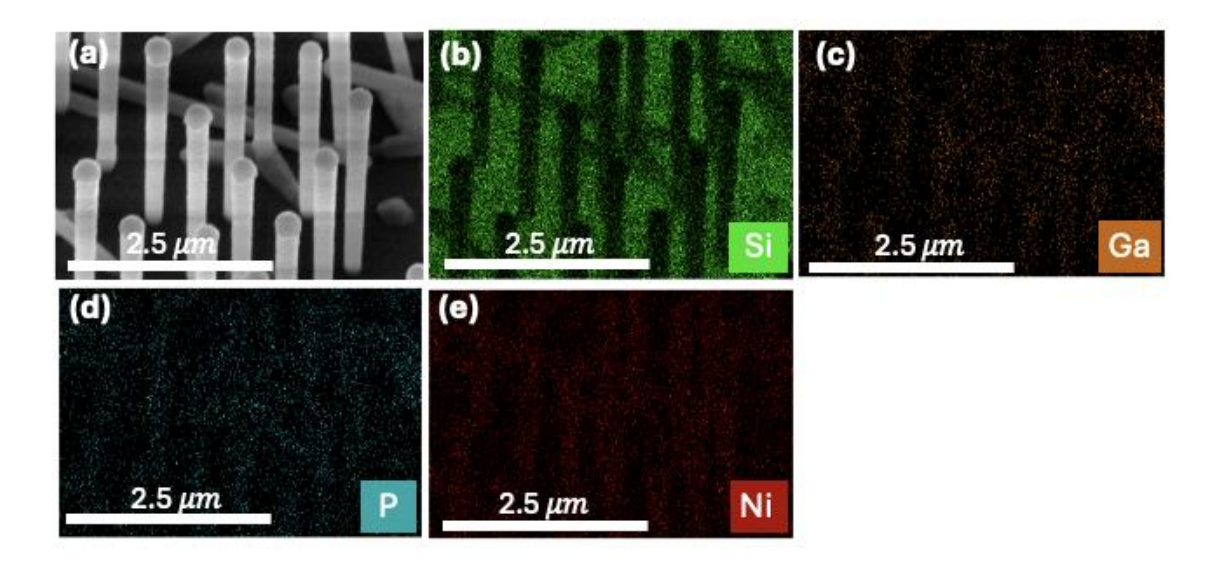


Figure 6.12. Conformal Ni coating achieved on GaP NWs at 1000 nm pitch. (a) SEM image of 1000 nm pitch GaP NWs after Ni deposition using $t_{on} = 10$ ms, $t_{off} = 1$ s, V = 3 V, and plating for 15 min. (b–e) EDX elemental maps showing distributions of Si (green), Ga (orange), P (blue), and Ni (red), respectively.

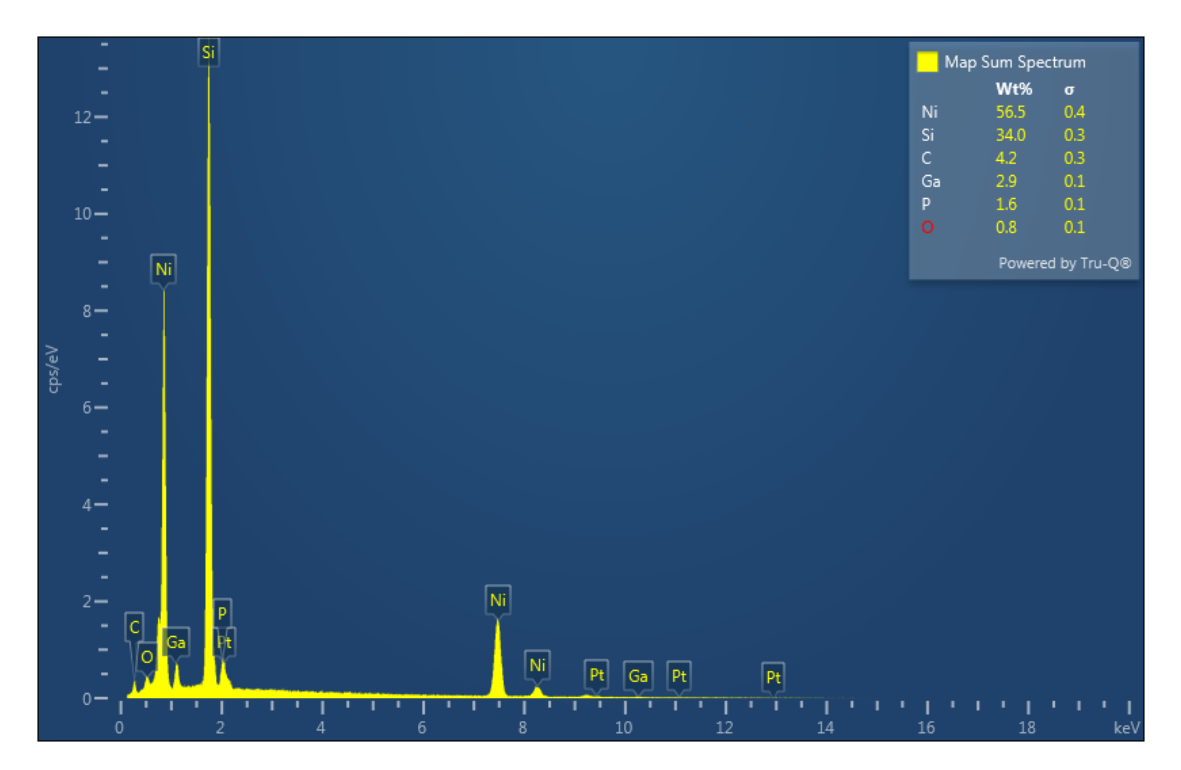


Figure 6.13. EDX map spectrum of 1000 nm pitch GaP NWs on p-type Si substrate.

Following the successful deposition of Ni uniformly without damaging the NW array, the same conditions ($t_{on} = 10 \text{ ms}$, $t_{off} = 1 \text{ s}$, and 3 V) were applied for 30 minutes and 45

minutes, as shown in Figure 6.15 (c) and (d), respectively. The SEM images in Figure 6.15 reveal that the Ni coating became thicker over time as later confirmed by TEM measurements.

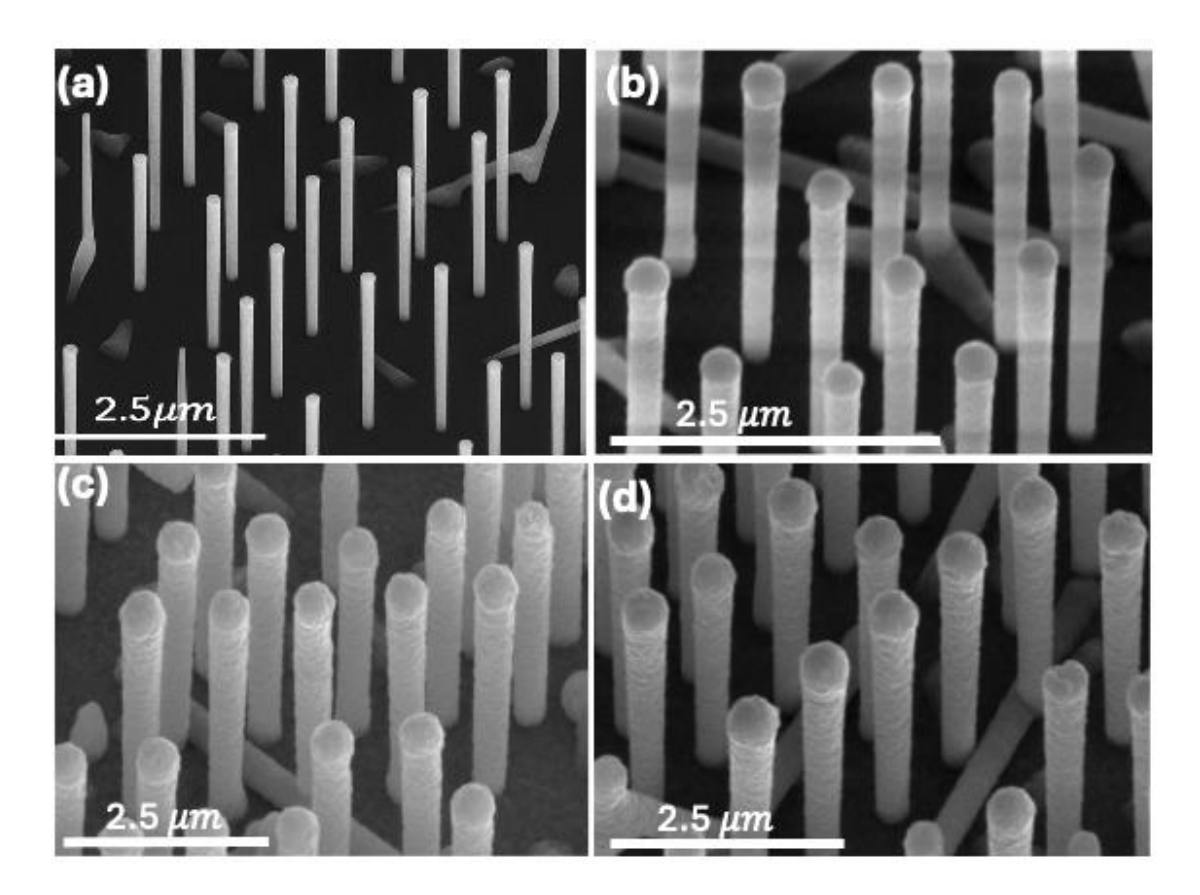


Figure 6.14. The morphological difference of GaP before and after deposition. (a) SEM of GaP NW array before deposition. (b-d) SEM images of GaP NWs (1000 nm pitch), showing conformal coating along sidewalls for 15 min, 30 min, and 45 min of Ni deposition, respectively.

Figure 6.16 shows transmission electron microscopy (TEM) of the GaP NWs sample at 45 min to gain insight into the crystallographic nature of the deposited Ni, electron beam diffraction (EBD) was employed (Figure 6.17). The resulting diffraction pattern shows concentric rings, proving that the crystal structure of Ni is polycrystalline. Detailed analysis of the ring radii and corresponding d-spacings confirm the presence of face-centered cubic (fcc) Ni reflections, with particularly strong agreement at the (200) plane

spacing (\approx 0.124 nm). In addition, a diffraction ring at approximately 0.239 nm is observed, which corresponds closely to the (111) plane. Higher-order reflections further confirm the polycrystalline nature of the Ni shell, with rings corresponding to the (222) and (400) planes.

The observation of a polycrystalline Ni shell is consistent with the electrodeposition mechanism, where nucleation and growth occur simultaneously across multiple sites along the NW surface. The conformal Ni coating thus develops from the coalescence of numerous nano-crystallites, leading to a continuous film with randomly oriented grains. This polycrystalline nature is advantageous for uniform coverage of high-aspect-ratio NWs, as grain boundaries can act as active sites for ion incorporation during growth, thereby promoting conformal deposition along the NW sidewalls.

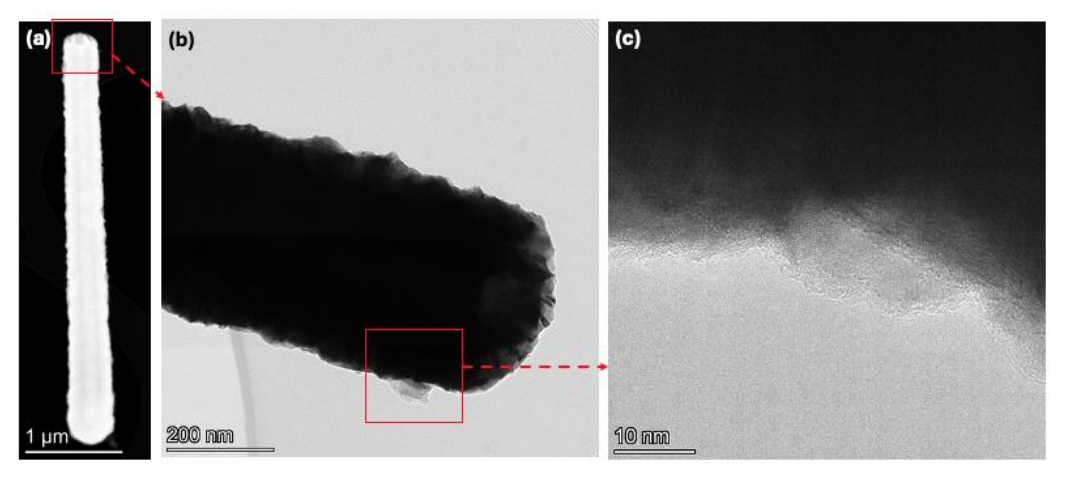


Figure 6.15. (a–c) TEM images of a Ni-coated GaP NW at increasing magnifications, from low (a) to high (c).

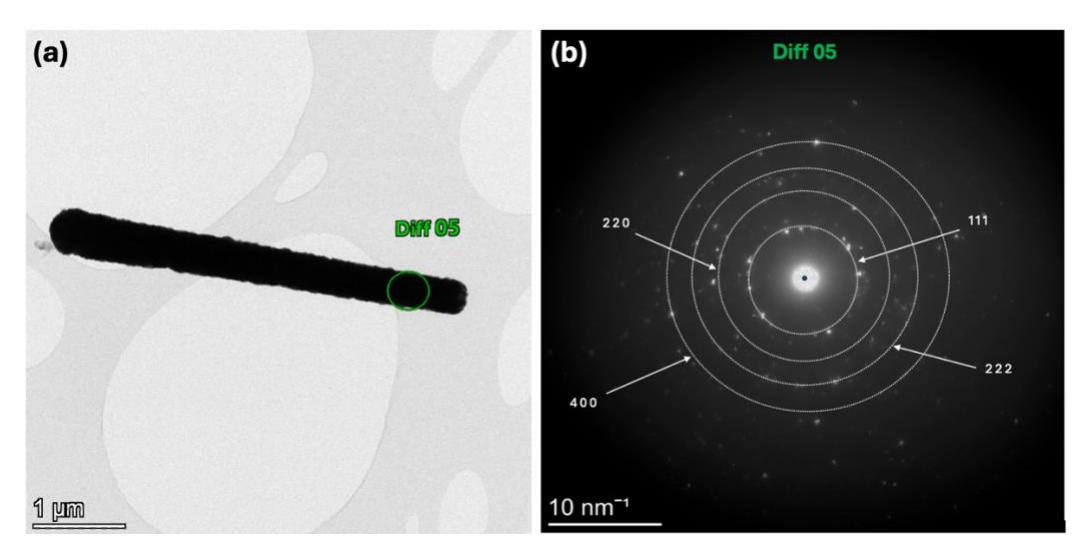


Figure 6.16. (a) TEM image of a Ni-coated GaP NW, showing the polycrystalline nature of the Ni layer. (b) Selected area electron diffraction (SAED) pattern obtained from region Diff 05.

Based on Figure 6.18, 6.19, and 6.20, the thicknesses of Ni at the top, middle, and the bottom of one NW were measured by TEM to be 150 nm, 166 nm, and 179 nm, respectively, after 45 min of deposition. The thickness of the Ni coating was approximated as 133 nm by comparing SEM images before and after deposition. The slight discrepancy between the thickness values obtained from TEM and SEM can be attributed to differences in measurement principles and resolution limits of the two techniques. TEM provides localized, high-resolution cross-sectional information, allowing more precise evaluation of the coating at specific positions along the NW length ⁵⁸. Therefore, the TEM-based measurements (average 165 nm) are considered more reliable for assessing the true Ni shell thickness, while the SEM estimate (133 nm) serves as a supporting approximation.

The overall comparison between SEM and TEM measurements, alongside the observed thickness uniformity, confirms that the adopted deposition parameters enable controllable and homogeneous Ni coating. This outcome highlights the capability of the process to

produce high-quality conformal metallic layers, suitable for applications in nanostructured electrodes, sensors, and energy devices.

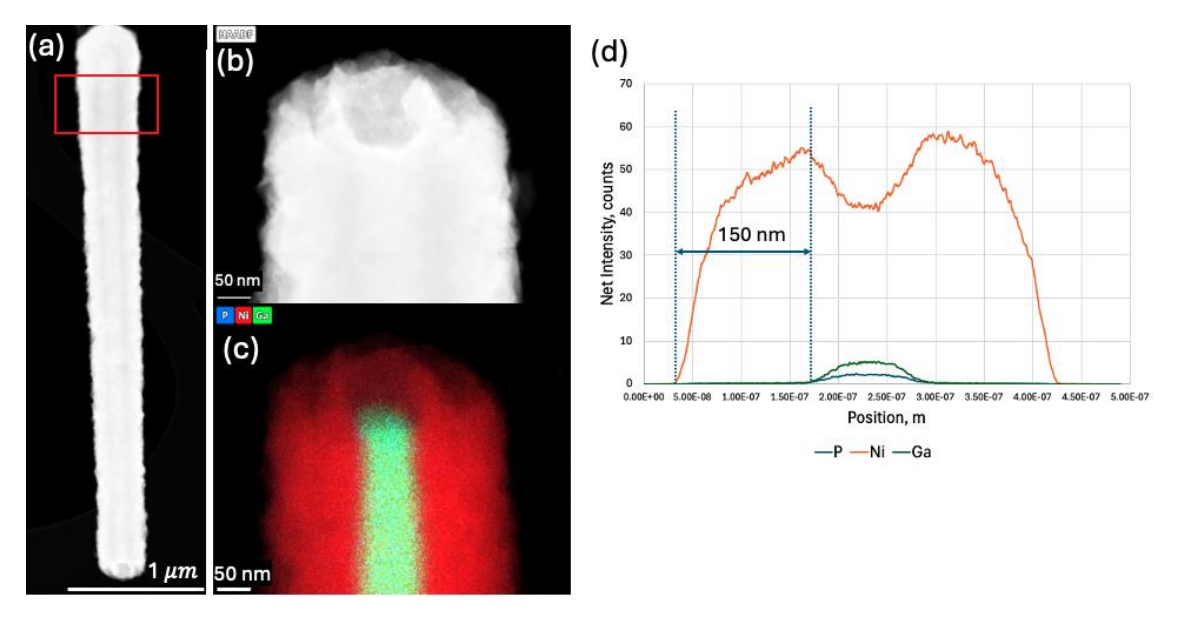


Figure 6.17. (a–b) TEM images of the top region of a GaP NW. (c) EDX elemental map of the same region, where red corresponds to Ni, blue to P, and green to Ga. (d) EDX linescan thickness analysis, showing Ni (orange), Ga (green), and P (blue), with the Ni layer thickness measured to be approximately 150 nm.

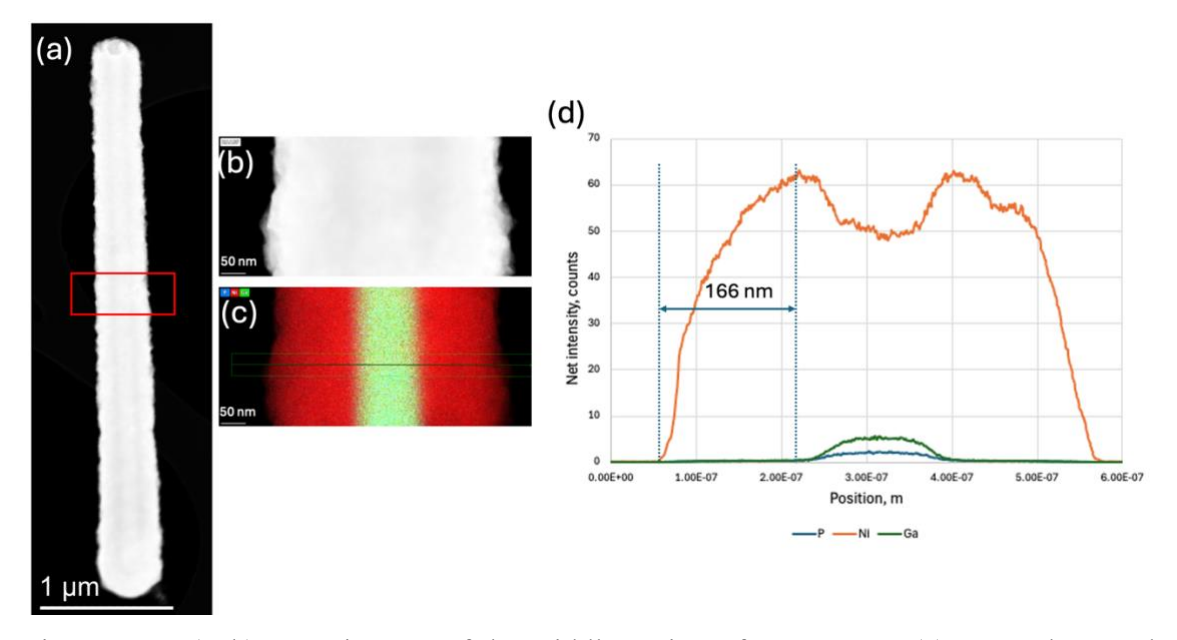


Figure 6.18. (a–b) TEM images of the middle region of a GaP NW. (c) EDX elemental map of the same region, where red corresponds to Ni, blue to P, and green to Ga. (d) EDX line-scan thickness analysis, showing Ni (orange), Ga (green), and P (blue), with the Ni layer thickness measured to be approximately 166 nm.

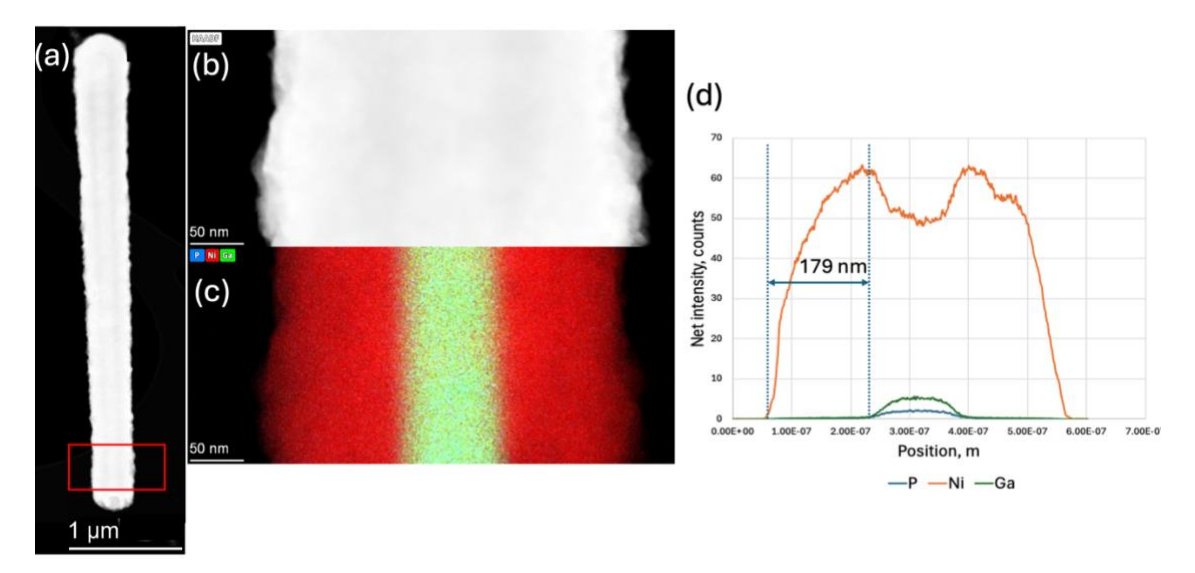


Figure 6.19. (a–b) TEM images of the bottom region of a GaP NW. (c) EDX elemental map of the same region, where red corresponds to Ni, blue to P, and green to Ga. (d) EDX line-scan thickness analysis, showing Ni (orange), Ga (green), and P (blue), with the Ni layer thickness measured to be approximately 179 nm.

Figure 6.21 illustrates the increase in the width of GaP NWs over time. During the first 30 minutes, the diameters increase rapidly and subsequently reaches saturation. The measurements were obtained from SEM images analyzed using ImageJ software. The data presented in Figure 6.21 were further used to determine the Ni coating thickness, as shown in Figure 6.22.

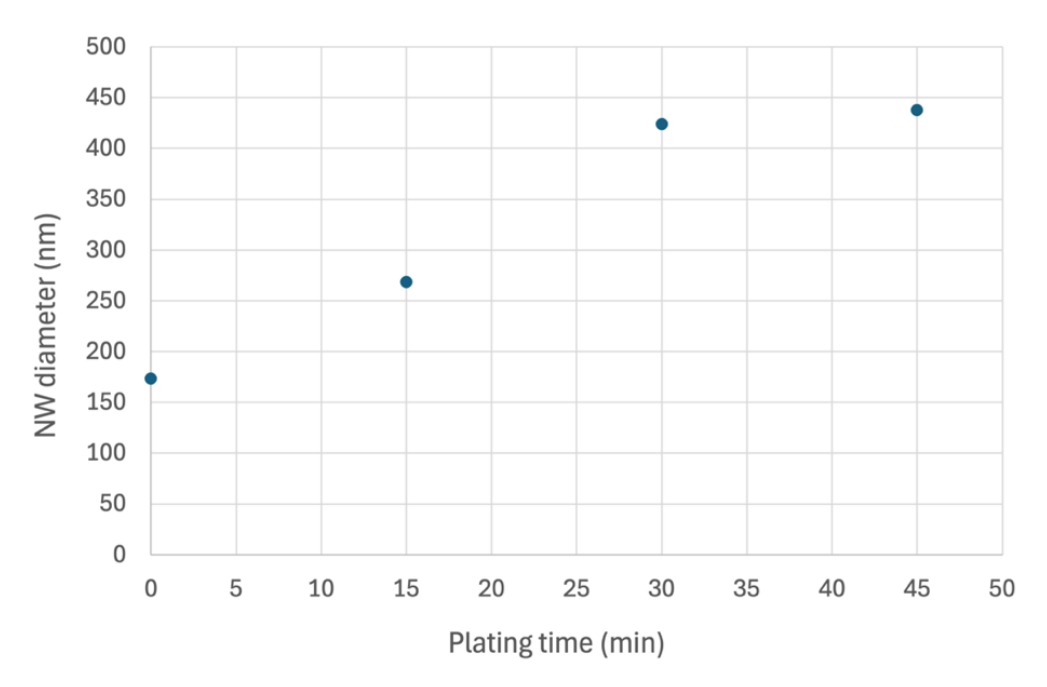


Figure 6.20. SEM measurements showing the increase in a GaP NW diameter with Ni coating as a function of time.

The thickness of the Ni coating was determined by subtracting the initial NW diameter as shown in Figure 6.22. The data reveal that rate of Ni deposition decreased markedly with increasing plating duration. The deposition rate during the first 15 minutes was 0.0528 nm/s, which increased to 0.0863 nm/s in the following 15 minutes (30 minutes total) before declining sharply to 0.00778 nm/s during the final 15 minutes (45 minutes total). Although the rate at 30 minutes was approximately 1.64 times greater than that at 15 minutes, a more than tenfold reduction was observed at 45 minutes compared to the preceding interval. Beyond this point, further extension of plating time would be expected to yield negligible additional Ni deposition. This behavior is attributed to the progressive reduction in spacing between NWs as the coating thickened, thereby restricting Ni²⁺ ion transport. A similar phenomenon was observed in the 360 nm and 600 nm pitch NW

M.A.Sc Thesis - L. Lam; McMaster University – Engineering Physics

arrays, where the higher NW density prevented Ni²⁺ ions from reaching the base of the array, resulting in negligible deposition.

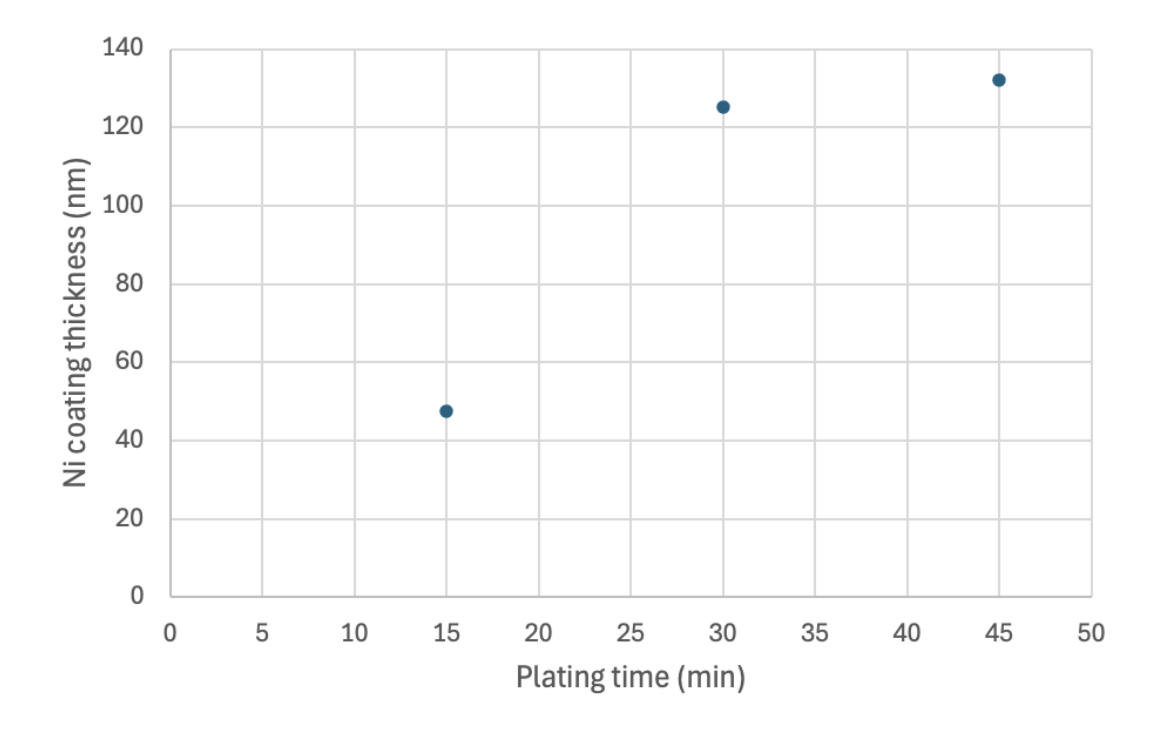


Figure 6.21. Evolution of the Ni coating thickness on GaP NWs with a 1000 nm pitch over time.

Chapter 7 Conclusions

This thesis has investigated Ni electroplating on GaAs and GaP NWs as a strategy for developing BV energy devices. By refining electrochemical cell designs and comparing DC deposition with PED, the work highlights both the challenges and opportunities in achieving uniform metallic coatings on high-aspect-ratio NWs.

The experimental approach evolved through successive improvements: starting with a simple beaker-based setup, progressing to a sealed electrolytic cell, and ultimately employing a custom Teflon cell. These developments demonstrated the critical role of cell geometry and electrode configuration in ensuring consistent deposition. While DC electrodeposition provided important initial insights, it also revealed limitations, such as non-uniform coatings, nanowire bundling, and, in some cases, dissolution of GaP NWs under high current density. In contrast, PED reduced mass-transport limitations and yielded more uniform coatings, particularly in arrays with wider NW spacing. The most successful results were obtained for GaP NWs with a 1000 nm pitch, where Ni shells formed uniformly without damaging the NWs. This highlights the importance of pitch as a key design parameter in controlling deposition and enabling efficient device fabrication. Beyond the experimental findings, this work provides a framework for understanding the interplay between NW geometry, deposition kinetics, and electrochemical transport. Correlating experimental observations with electric field simulations and drift-diffusion considerations clarified why some configurations succeed while others fail, offering guidance for optimizing future integration of ⁶³Ni into NW-based BV devices.

Looking forward, further refinement of pulse parameters, exploration of alternative electrolytes, and suppression of tip overgrowth could extend conformal coating to denser

M.A.Sc Thesis - L. Lam; McMaster University – Engineering Physics

NW arrays. Applying these optimized methods to ⁶³Ni deposition will be a crucial step toward the realization of long-lived nuclear batteries with applications in space exploration, biomedical implants, and remote sensing.

In summary, this thesis demonstrates that careful control of electroplating conditions, coupled with deliberate design of NW architecture, is essential for advancing the next generation of BV devices. These insights establish a foundation for future innovations in nanoscale energy harvesting technologies.

References

- 1. Heinini M. *Molecular Beam Epitaxy: Fundamentals, Historical Background and Future Prospects.* 2012, pp 2–3. DOI:10.1016/B978-0-12-387839-7.00001-4
- 2. Güniat L.; Caroff P.; Fontcuberta i Morral A. Vapor Phase Growth of Semiconductor Nanowires: Key Developments and Open Questions. *Chem. Rev.* 2019, *119*, pp 8958–8971. DOI: 10.1021/acs.chemrev.8b00649
- 3. Thomas A. Design and Fabrication of a Gallium Phosphide Nanowire Betavoltaic Device; Ph.D. Thesis, McMaster University, 2025.
- 4. Dhakal, S.; Minx, J. C.; Toth, F. L.; Abdel-Aziz, A.; Figueroa Meza, M. J.; Hubacek, K.; Jonckheere, I. G. C.; Kim, Y.-G.; Nemet, G. F.; Pachauri, S.; Tan, X. C.; Wiedmann, T. Emissions Trends and Drivers. In Climate Change 2022: Mitigation of Climate Change. Contribution of Working Group III to the Sixth Assessment Report of the Intergovernmental Panel on Climate Change; Shukla, P. R.; Skea, J.; Slade, R.; Al Khourdajie, A.; van Diemen, R.; McCollum, D.; Pathak, M.; Some, S.; Vyas, P.; Fradera, R.; Belkacemi, M.; Hasija, A.; Lisboa, G.; Luz, S.; Malley, J., Eds.; Cambridge University Press: Cambridge, U.K.; New York, NY, 2022; DOI: 10.1017/9781009157926.004.
- 5. Wang J.; Azam W. Natural Resource Scarcity, Fossil Fuel Energy Consumption, and Total Greenhouse Gas Emissions in Top Emitting Countries. *Geoscience Frontiers*. 2024, *15*, 101757. DOI: 10.1016/j.gsf.2023.101757
- 6. Naseem M. B.; Kim H. S.; Lee J.; Kim C. H.; In S. I. Betavoltaic Nuclear Battery: A Review of Recent Progress and Challenges as an Alternative Energy Source. *J. Phys. Chem. C.* 2023, *127*, 7565–7579. DOI: 10.1021/acs.jpcc.3c00684
- 7. Rappaport P. The Electron-Voltaic Effect in P-N Junctions Induced by Beta-Particle Bombardment. *Phys. Rev.* 1954, *93*, pp 246–247. DOI: https://doi.org/10.1103/PhysRev.93.246.2
- 8. McNamee. S. Fabrication of a GaP Nanowire Betavoltaic Device Using Ni-63; master's Thesis, McMaster University, 2018.
- 9. Zhou C.; Zhang J.; Wang X.; Yang Y.; Xu P.; Li P.; ... Wu W. Review—Betavoltaic Cell: The Past, Present, and Future. *ECS J. Solid State Sci. Technol.* 2021, *10*, 027005. DOI: 10.1149/2162-8777/abe423
- 10. Butterfield A. *A Dictionary of Electronics and Electrical Engineering*, 5th ed.; Oxford University Press, 2018. DOI: 10.1093/acref/9780198725725.001.0001
- 11. Pan A.; Zhu X. Optoelectronic Properties of Semiconductor Nanowires. In *Semiconductor Nanowires: Materials, Synthesis, Characterization and Applications*; 2015; pp 327–363. DOI: 10.1016/B978-1-78242-253-2.00012-8
- 12. Olsen L. C.; Cabauy P.; Elkind B. J. Betavoltaic Power Sources. *Phys. Today* 2012, *65*, pp 35–38. DOI: 10.1063/PT.3.1820
- 13. Alam T. R.; Tchouaso M. T.; Prelas M. A. Summary of the Design Principles of Betavoltaics and Space Applications; *Photovoltaics for Space*, 2023, pp 293-345. DOI: 10.1016/B978-0-12-823300-9.00003-0

- 14. Alam T. R.; Pierson M. A.; Prelas M. A. Beta Particle Transport and Its Impact on Betavoltaic Battery Modeling. *Appl Radiat and Isot.* 2017, *130*, pp 80–89. DOI: 10.1016/j.apradiso.2017.09.009
- 15. Wagner D.; Novog D. R.; Lapierre R. R. Simulation and Optimization of Current Generation in Gallium Phosphide Nanowire Betavoltaic Devices. *J. Appl. Phys.* 2019, *125*, 16. DOI: 10.1063/1.5093805
- 16. Kavanagh K. L. Misfit Dislocations in Nanowire Heterostructures. *Semicond. Sci. Technol.* 2010, *25*, 024006. DOI: 10.1088/0268-1242/25/2/024006
- 17. Ulmen B.; Desai P. D.; Moghaddam S.; Miley G. H.; Masel R. I. Development of Diode Junction Nuclear Battery Using 63Ni. *J. Radioanal. Nucl. Chem.* 2009, 282, pp 601–604. DOI: 10.1007/s10967-009-0320-3
- Wang K.; Cao B.; Chen J.; Zhou W. TEM Studies of Nanostructures. In *Modeling, Characterization, and Production of Nanomaterials*; V. K. Tewary, Y. Zhang, Eds.; Woodhead Publishing, 2015; pp 115–144. DOI: 10.1016/B978-1-78242-228-0.00004-1
- 19. Mai L. Q. Semiconductor Nanowire Battery Electrodes. In *Semiconductor Nanowires*; J. Arbiol, Q. Xiong, Eds.; Woodhead Publishing, 2015; pp 441–469. DOI: 10.1016/B978-1-78242-253-2.00016-5
- 20. Kuzmin V.; Mokhov D.; Berezovskaya T.; Monastyrenko A.; Bouravleuv A. Electrochemical Deposition of Ni on Arrays of GaAs Nanowires with n-Type Channels. *Nanotechnology* 2025, *36*, 105601. DOI: 10.1088/1361-6528/ada2f2
- 21. Lozovoy K. A.; Korotaev A. G.; Kokhanenko A. P.; Dirko V. V.; Voitsekhovskii A. V. Kinetics of Epitaxial Formation of Nanostructures by Frank–van der Merwe, Volmer–Weber and Stranski–Krastanow Growth Modes. *Surf. Coat. Technol.* 2020, *384*, 125289. DOI: 10.1016/j.surfcoat.2019.125289
- 22. Plante M. C. *Metal-Assisted Growth of III-V Nanowires by Molecular Beam Epitaxy*; Ph.D. Thesis, McMaster University, 2009.
- 23. Kreysa G.; Ota K.I, Savinell R.F. *Encyclopedia of Applied Electrochemistry*; 2014. DOI: 10.1007/978-1-4419-6996-5
- 24. Ciobanu M.; Wilburn J. P.; Krim M. L.; Cliffel D. E. *Handbook of Electrochemistry*; Springer, 2024.
- 25. Stock J. T. Chapter 1 Electrochemistry in Retrospect: An Overview. *American Chemical Society*, 2011; pp 1–17. DOI: 10.1021/bk-1989-0390.ch001
- 26. Kang H.; Kim J. S.; Choi S. R.; Kim Y. H.; Kim D. H.; Kim J. G.; Lee T.W.; Cho J. H. Electroplated Core–Shell Nanowire Network Electrodes for Highly Efficient Organic Light-Emitting Diodes. *Nano Convergence* 2022, *9*, pp 1–8. DOI: 10.1186/s40580-021-00295-2
- 27. Kloke A.; Von Stetten F.; Zengerle R.; Kerzenmacher S. Strategies for the Fabrication of Porous Platinum Electrodes. *Adv. Mater.* 2011, *23*, 4976–5008. DOI: 10.1002/adma.201102182
- 28. Rose I.; Whittington C. *Nickel Plating Handbook*; Nickel Institute, 2013; pp 263–292.
- 29. Jerkiewicz G. Standard and Reversible Hydrogen Electrodes: Theory, Design, Operation, and Applications. *ACS Catal.* 2020, *10 (15)*, pp 8409–8417. DOI: 10.1021/acscatal.0c02046

- 30. Vives A. A. Piezoelectric Transducers and Applications. 2nd Edition, *Springer* 2008. DOI: 10.1007/978-3-540-77508-9
- 31. Ojo A. A.; Dharmadasa I. M. Electroplating of Semiconductor Materials for Applications in Large Area Electronics: A Review. *Coatings* 2018, *8*, 262. DOI: 10.3390/coatings8080262
- 32. Tambe C. E.; Green T. A.; Roy S. The Multifaceted Role of Boric Acid in Nickel Electrodeposition and Electroforming. *J. Electrochem. Sci. Technol.* 2024, *171*. DOI: 10.1149/1945-7111/ad80d3
- 33. Graham L. M.; Cho S.; Kim S. K.; Noked M.; Lee S. B. Role of Boric Acid in Nickel Nanotube Electrodeposition: A Surface-Directed Growth Mechanism. *Chem. Commun.* 2014, *50*(*5*), pp 527–529. DOI: 10.1039/c3cc47183g
- 34. Kabay N.; Güler E.; Bryjak M. Boron in Seawater and Methods for Its Separation: A Review. *Desalination* 2010, *261*, pp 212–217. DOI: 10.1016/j.desal.2010.05.033
- 35. Devesa S.; Santos G.; Cavaleiro D.; Lopes M.; Ramos A. S.; Carvalho S. A Comprehensive Investigation of Boric Acid-Free Electrodeposition of Ni-P Alloy on Steel. *Colloids Surf.*, A 2025, 705, 135678. DOI: 10.1016/j.colsurfa.2024.135678
- 36. Li S. Chapter 13 Introduction to Electrochemical Reaction Engineering. In *Reaction Engineering*; 2017; pp 599–651. DOI: 10.1016/B978-0-12-410416-7.00013-6
- 37. Schweitzer G. K.; Pesterfield L. L. E-PH Diagrams. In *Aqueous Chemistry of the Elements*; 2010. DOI: 10.1093/oso/9780195393354.003.0003
- 38. Monk D. J.; Soane D. S.; Howe R. T. A Review of the Chemical Reaction Mechanism and Kinetics for Hydrofluoric Acid Etching of Silicon Dioxide for Surface Micromachining Applications. *Thin Solid Films* 1993, *232*, pp 1–12. DOI: 10.1016/0040-6090(93)90752-B
- 39. Kallesøe C.; Mølhave K.; Larsen K. F.; Engstrøm D.; Hansen T. M.; Bøggild P.; Mårtensson T.; Borgström M.; Samuelson L. Integration, Gap Formation, and Sharpening of III-V Heterostructure Nanowires by Selective Etching. *J. Vac. Sci. Technol.*, *B* 2010, *28* (1), pp 21–26. DOI: 10.1116/1.3268135
- 40. Houston M. R.; Maboudian R. Stability of Ammonium Fluoride–Treated Si(100); *J. Appl. Phys.* 78; pp 3801–3808, 1995. DOI: 10.1063/1.359894
- 41. Sacher E.; Yelon A. Comment on Mechanism of HF Etching of Silicon Surfaces: A Theoretical Understanding of Hydrogen Passivation. *Phys. Rev. Lett.* 1991, *66*, 1647. DOI: 10.1103/PhysRevLett.66.1647
- 42. Ghita R. V. Evolution of Surface Oxides on GaAs. *J. Optoelectron. Adv. Mater.* 2015, *17*, No.11-12; pp 1703–1709.
- 43. Safety Data Sheet; Epo-tek ® H2OE PART A, 2023.
- 44. Bennett B. R.; Magno R.; Boos J. B.; Kruppa W.; Ancona M. G. Antimonide-Based Compound Semiconductors for Electronic Devices: A Review. *Solid-State Electron.* 2005, 49 (12), pp 1875–1895. DOI: 10.1016/j.sse.2005.09.008
- 45. Power Supply Korad; SHENZHEN KORAD TECHNOLOGY CO. LTD.
- 46. Keithley. Series 2400 SourceMeter® User's Manual. 2011.
- 47. Mamaghani K. R.; Naghib S. M. The Effect of Stirring Rate on Electrodeposition of Nanocrystalline Nickel Coatings and Their Corrosion

- Behaviors and Mechanical Characteristics. *Int. J. Electrochem. Sci.* 2017, *12*, pp 5023–5035. DOI: 10.20964/2017.06.68
- 48. Jyoti Biswal H.; Vundavilli P. R.; Gupta A. Investigations on the Effect of Electrode Gap Variation over Pulse-Electrodeposition Profile. *IOP Conf. Ser.: Mater. Sci. Eng.* 2019, 653, 012046. DOI: 10.1088/1757-899X/653/1/012046
- 49. Yusron R. M.; Bisono R. M.; Pramudia M. Effect Electrolyte Temperature and Electrode Distance to Electroplating Hard-Chrome on Medium-Carbon Steel. *J. Phys.: Conf. Ser.* 2020, *1569*, 042007. DOI: 10.1088/1742-6596/1569/4/042007
- 50. Han Y.-P. *HF Vapor Etching and Cleaning of Silicon Wafer Surfaces*. PhD Thesis, Massachusetts Institute of Technology, 1999. DOI: 10.1109/IMFEDK.2004.1566427
- 51. Meng L.; Zhu J.; Bian R.; Xu B.; Tang Z.; Zhang Y.; Liu H. Multidimensional Aligned Nanowires Array: Toward Bendable and Stretchable Strain Sensors. *Coatings* 2021, *11*, 975. DOI: 10.3390/coatings11080975
- 52. Tilve-Martínez D.; Lozano-Steinmetz F.; Gómez-Palos I.; Vitatela J. Ordered Silicon Nanowire Bundle Networks from Aqueous Dispersions. *Nanotechnology* 2025, *36* (*32*). DOI: 10.1088/1361-6528/adef60
- 53. An E. Y.; Lee S.; Lee S. G.; Lee E.; Baek J. J.; Shin G.; Choi K.H; Cho J.H; Bae G. Y. Self-Patterned Stretchable Electrode Based on Silver Nanowire Bundle Mesh Developed by Liquid Bridge Evaporation. *Nanomaterials* 2021, *11*, 12865. DOI: 10.3390/nano11112865
- 54. Wei Z.; Schneider T. M.; Kim J.; Kim H. Y.; Aizenberg J.; Mahadevan L. Elastocapillary Coalescence of Plates and Pillars. *Proc. R. Soc. A* 2015, *471*, 20140593. DOI: 10.1098/rspa.2014.0593
- 55. Jenkins D. W. K.; Allen G. C.; Prewett P. D.; Heard P. J. Focused Ion-Beam Assisted Deposition of Tungsten and Carbon. *J. Phys.: Condens. Matter* 1991, *3*, S32. DOI: 10.1088/0953-8984/3/S/032
- 56. Sato H.; Yui M.; Yoshikawa H. Ionic Diffusion Coefficients of Cs+, Pb2+, Sm3+, Ni2+, SeO42-, and TcO4- in Free Water Determined from Conductivity Measurements. *J. Nucl. Sci. Technol.* 1996, *33*, pp 950–955. DOI: 10.1080/18811248.1996.9732037
- 57. Jodłowski P. J.; Jędrzejczyk R. J.; Gancarczyk A.; Łojewska J. New Method of Determination of Intrinsic Kinetic and Mass Transport Parameters from Typical Catalyst Activity Tests: Problem of Mass Transfer Resistance and Diffusional Limitation of Reaction Rate. *Chem. Eng. Sci.* 2017, *162*, pp 322–331. DOI: 10.1016/j.ces.2017.01.024
- 58. Brodusch N.; Brahimi S. V.; Barbosa De Melo E.; Song J.; Yue S.; Piché N.; Gauvin R. Scanning Electron Microscopy versus Transmission Electron Microscopy for Material Characterization: A Comparative Study on High-Strength Steels. *Scanning* 2021, 5511618. DOI: 10.1155/2021/5511618